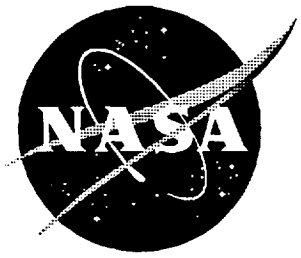

NASA Technical Paper 3515

Study of Potential Aerodynamic Benefits From Spanwise Blowing at Wingtip

Raymond E. Mineck
Langley Research Center • Hampton, Virginia

National Aeronautics and Space Administration
Langley Research Center • Hampton, Virginia 23681-0001

June 1995

Available electronically at the following URL address: http://techreports.larc.nasa.gov/ltrs/ltrs.html

Printed copies available from the following:

NASA Center for AeroSpace Information
800 Elkridge Landing Road
Linthicum Heights, MD 21090-2934
(301) 621-0390

National Technical Information Service (NTIS)
5285 Port Royal Road
Springfield, VA 22161-2171
(703) 487-4650

Contents

Summary

Comprehensive experimental and analytical studies have been conducted to assess the potential aerodynamic benefits from spanwise blowing at the tip of a moderate-aspect-ratio swept wing. Previous studies on low-aspect-ratio wings indicated that spanwise blowing from the wingtip can diffuse the tip vortex and displace it outward. The diffused and displaced vortex will induce a smaller downwash at the wing, and consequently the wing will have increased lift and decreased induced drag at a given angle of attack.

A semispan wing with spanwise blowing from the wingtip has been tested in the Langley 7- by 10-Foot High-Speed Tunnel. Tests with and without blowing were conducted at a Mach number of 0.30 over an angle-of-attack range from −2.0° to 11.0°. Additional testing was conducted at a Mach number of 0.72 without blowing and at Mach numbers from 0.20 to 0.50 with blowing. Different wingtip blowing configurations were tested to investigate the effects of jet-exit chordwise length, chordwise and vertical locations, and exhaust direction. Results indicated that blowing from jets with a short chord had little effect on lift or drag, but blowing from jets with a longer chord increased lift near the tip and reduced drag at low Mach numbers.

A Navier-Stokes solver was modified to simulate the jet blowing at the wingtip. The modified solver predicted the aerodynamic characteristics of the wing without blowing reasonably well at Mach numbers of 0.30 and 0.72, and, except for the wing drag, it predicted the aerodynamic characteristics of the wing with blowing at a Mach number of 0.30. The solver was then used to predict the results with blowing at a Mach number of 0.72. Calculations indicated that lift and drag increased with increasing jet momentum coefficient.

Because the momentum of the jet is typically greater than the reduction in the wing drag and the increase in the wing lift due to spanwise blowing is small, spanwise blowing at the wingtip does not appear to be a practical means of improving the aerodynamic efficiency of moderate-aspect-ratio wings at high subsonic Mach numbers.

Introduction

Aerodynamic efficiency is an important factor in the marketing of subsonic, commercial transport aircraft. Efficiency can be improved by increasing the maximum lift-to-drag ratio at the cruise flight condition. Because induced drag is typically 30 percent or more of the total drag on a subsonic transport in cruising flight (ref. 1), it is frequently the target of drag reduction efforts. Reducing the strength of the wingtip vortices, diffusing them, and displacing them outboard will reduce the downwash on the wing at a given angle of attack, thereby resulting in an increase in lift and a decrease in induced drag. Subscale experiments (ref. 2) have shown that spanwise blowing from the wingtip displaces and diffuses the wingtip vortex. Spanwise wingtip blowing thus has the potential to increase the wing aerodynamic efficiency. This report investigates spanwise blowing from the wingtip as a potential means to increase lift and reduce induced drag.

Wingtip blowing entails exhausting one or more jets of air from the wingtip in a generally spanwise direction, as shown in figure 1. The parameter used to characterize the jet-blowing magnitude is the jet momentum coefficient, (C_μ). For this study, the reference quantities used to define the jet momentum coefficient are the free-stream dynamic pressure and the wing reference area. Thus, the magnitude of the jet momentum can be directly compared with the wing lift and drag when using the appropriate coefficients. Two types of jets have been studied: a single, long-chord jet and several discrete, short-chord jets. Air for the jet can be bled from the propulsion system, removed from the flow at the aircraft surface by a laminar-flow-control system, or ducted from the region of the stagnation line along the wing leading edge. The jet momentum is treated as a gross thrust or force. To account for all the forces properly, the mass flow for the jet is assumed to be decelerated to a stagnant condition. The force to decelerate the jet mass flow is referred to as the "ram drag." If engine bleed air is used, the ram drag of the extra air must be included when evaluating the results. The use of air ducted from the leading edge, as shown in figure 2, would provide a passive system with a portion of the ram drag already included. However, only relatively small mass-flow rates and jet momentum coefficients would be available from such a system.

Early work in wingtip blowing (refs. 2–5) addressed lift augmentation of low-aspect-ratio wings. These tests usually involved large jet momentum coefficients and jet chords that were a large fraction of the wingtip chord like the long-chord jet shown in figure 1. The required jet mass-flow rates and momentum coefficients were quite large. In most cases, the jets exhausted in the plane of the wing and normal to the free-stream direction. The results from these early works showed that spanwise blowing increased the lift-curve slope and sometimes reduced the drag at a given lift. Blowing increased the loading across the span of a low-aspect-ratio wing with the largest increases occurring near the tip (closest to the source). The addition of blowing also increased the maximum lift coefficient. Flow surveys behind the wing with and without blowing indicated that blowing displaced the primary wingtip vortex outward and upward,

diffused the vortex over a larger area, and reduced the maximum vorticity at the center of the vortex. Tests of spanwise blowing with different jet vertical locations and exhaust directions (ref. 2) showed that displacing the jet toward the upper surface or deflecting the jet downward increased the beneficial increment in lift above that found for the jet exhausting spanwise on the centerline of the wingtip.

As previously mentioned, these exploratory investigations (refs. 2–5) primarily studied the effect of spanwise blowing on the lift of low-aspect-ratio wings. Values of jet momentum coefficient ranged from about 0.10 to 1.75. For a hypothetical transport aircraft in cruising flight with a lift-to-drag ratio of about 15 and a cruise lift coefficient of about 0.6, the total engine thrust coefficient is 0.6/15 or 0.04. Jet momentum coefficients used in these exploratory investigations are much larger than the hypothetical installed engine thrust. Such large values are not practical for drag reduction studies.

Tests using several short-chord jets, reported in references 6–8, were made at much lower blowing coefficients, typically between 0.001 and 0.008, by using a rectangular wing with an aspect ratio of 3.4. Benefits from blowing were found to be strongly dependent on the location and direction of the jet exhaust. The results indicated that blowing from several short-chord jets (see fig. 1) can produce trends similar to those obtained with a single continuous jet, although the magnitude of the effects is smaller. Additional information concerning other studies on spanwise blowing at the wingtip is presented in reference 9.

Because previous investigations used large jet momentum coefficients and low-aspect-ratio wings, a systematic study of the effects of jet location and exhaust direction on the benefits of wingtip blowing is needed on a moderate-aspect-ratio wing with practical values of jet momentum coefficient. The purpose of this investigation is to evaluate the potential aerodynamic benefits from spanwise blowing at the tip of a wing planform representative of those found on subsonic transport aircraft. This report presents results from a wind tunnel test of a moderate-aspect-ratio swept wing with spanwise blowing from discrete jets at the wingtip.

Baseline data without wingtip blowing were obtained at Mach numbers of 0.30 and 0.72. The effects of jet chordwise length, chordwise location, vertical location, in-plane deflection, and out-of-plane deflection were investigated at a Mach number of 0.30. This test was conducted in the NASA Langley 7- by 10-Foot High-Speed Tunnel. Wing forces and moments and surface pressures were measured along with the mass-flow rate, pressure, and temperature of the jet. The experimental results were supplemented with Navier-Stokes calculations on simulated blowing from the wingtip at a Mach number of 0.72.

Symbols

All measurements and calculations were made in U. S. customary units.

b	exposed wing semispan, ft
C_B	wing-root bending-moment coefficient, $M_X/q_\infty Sb$
$C_{B_{C_L}}$	slope of wing-root bending-moment curve, dC_B/dC_L
$C_{B,0}$	wing-root bending-moment coefficient at zero lift
C_D	wing drag coefficient, $D/q_\infty S$
$C_{D,\text{tot}}$	total drag coefficient including ram drag penalty, $(D + \dot{m}_j V_\infty)/q_\infty S$
$C_{D,0}$	wing drag coefficient at zero lift
C_L	wing lift coefficient, $L/q_\infty S$
C_{L_α}	wing lift-curve slope, $dC_L/d\alpha$, deg^{-1}
C_m	wing pitching-moment coefficient, $M_Y/q_\infty S\bar{c}$
$C_{m_{C_L}}$	slope of wing pitching-moment curve, dC_m/dC_L
$C_{m,0}$	wing pitching-moment coefficient at zero lift
C_p	local static pressure coefficient, $(p - p_\infty)/q_\infty$
C_p^*	static pressure coefficient at sonic conditions
C_μ	total jet momentum coefficient, $C_{\mu,F} + C_{\mu,R}$
$C_{\mu,F}$	front jet momentum coefficient, $(\dot{m}_j V_j)_F/q_\infty S$
$C_{\mu,R}$	rear jet momentum coefficient, $(\dot{m}_j V_j)_R/q_\infty S$
c	local wing chord, ft
$\bar{c}$	mean aerodynamic chord, 0.616 ft
c_j	chordwise length of jet, in.
c_l	section lift coefficient, $l/q_\infty c$
c_{tip}	wingtip chord, 4.00 in.
D	force in drag direction, lbf
h	body height, ft
L	force in lift direction, lbf
l	section lift per unit span, lbf/ft
M_X	moment about X-axis resolved about wing root, ft-lbf
M_Y	moment about Y-axis resolved about $0.25\bar{c}$, ft-lbf
M_∞	free-stream Mach number
$\dot{m}_j$	jet mass-flow rate, slugs/sec

N_c number of chordwise cells in structured Navier-Stokes grid

N_n number of normal cells in structured Navier-Stokes grid

N_s number of spanwise cells in structured Navier-Stokes grid

N_t number of spanwise cells around each half of wingtip in structured Navier-Stokes grid

p local static pressure, lbf/ft^2

p_∞ free-stream static pressure, lbf/ft^2

q_∞ free-stream dynamic pressure, $\frac{1}{2}\rho_\infty V_\infty^2$, lbf/ft^2

R unit Reynolds number per foot, $\rho_\infty V_\infty / \mu$

S wing (exposed) reference area, 0.978 ft^2

V_j jet-exit velocity, ft/sec

V_x component of local velocity in x-direction, ft/sec

V_∞ free-stream velocity, ft/sec

X,Y,Z axis system with origin at wing moment reference center (see fig. 12)

x chordwise distance, positive when measured aft from wing leading edge, ft

x_j chordwise distance from wingtip leading edge to center of jet exit, in.

y spanwise distance, positive when measured outward on right wing, ft

y^+ normal spacing parameter for grid in boundary layer

z vertical distance, positive measured up from airfoil reference line, ft

z_j vertical distance from airfoil reference line to center of jet exit, in.

α wing angle of attack, positive leading edge up, deg

α_i flow angle induced by presence of body, deg

α_0 wing angle of attack at zero lift, deg

Δ change in parameter due to blowing, Value (with blowing) – Value (without blowing)

δ_j jet dihedral (deflection in YZ-plane), deg (see fig. 7)

η fraction of wing semispan, y/b

ρ_∞ free-stream density, slugs/ft^3

ψ_j jet sweep (deflection in XY-plane), deg (see fig. 7)

Subscripts:

F front

R rear

Abbreviations:

AOA angle of attack

ARL airfoil reference line

HSNLF High-Speed Natural Laminar Flow

HST High-Speed Tunnel

mac mean aerodynamic chord

3-D three dimensional

Wind Tunnel

The experimental portion of this study was performed in the Langley 7- by 10-Foot High-Speed Tunnel (7 × 10 HST). Descriptions of the tunnel and its support equipment can be found in reference 10. A sketch of the internal components of the test section is presented in figure 3. The 7 × 10 HST is a single-return, closed-circuit, fan-driven wind tunnel that operates at atmospheric temperature and pressure. All four test section walls are solid, and wooden fairings on the sidewalls provide a uniform longitudinal Mach number distribution along the centerline of the test section. The test section is 6.58 ft high and 9.57 ft wide with a usable length of 10.83 ft. Four turbulence reduction screens are located just upstream of the 17:1 contraction section to provide good flow quality. A 14 000-hp variable-speed motor drives the fan to provide a continuous Mach number range from near 0 to 0.94 with the test section empty. The nominal test conditions of the tunnel are presented in figure 4. The tunnel has a sting-model support system for full-span model testing and a sidewall turntable on the left wall for semispan model testing. For this investigation, the model was mounted on the sidewall turntable with the sting-model support system stowed along the floor of the test section to minimize interference.

Model

The model used in this investigation was representative of the outer portion of the wing of a subsonic commercial passenger transport. Planforms of several commercial passenger transports were scaled so that each had a wingspan of unity. A comparison of the scaled planforms showed that the leading-edge sweep, the location of the discontinuity in the wing trailing-edge sweep angle, and the taper in the outboard portion of the wing were similar for many types of subsonic passenger transports. The values of the wing parameters selected for this investigation were as follows: a leading-edge sweep of 33°, a change in the wing trailing-edge sweep angle at the 40-percent-semispan location, and a taper ratio of 0.4 outboard of the location of the discontinuity in the wing sweep angle. Only the portion of a transport wing

outboard of the 40-percent-semispan location was modeled because the induced effects from jet blowing at the tip of a moderate-aspect-ratio wing were expected to be very small near the root.

The model was originally designed for testing in a wind tunnel with a test section that was 36 in. wide. To keep wall interference to a reasonable level and to maximize the model size, a semispan configuration was selected with a root chord of 10.0 in., a tip chord of 4.0 in., and a semispan of 20.26 in. Photographs of the model are shown in figure 5 and sketches are shown in figure 6. The NASA HSNLF(1)-0213 airfoil section, designed for a lift coefficient of 0.2 at a Mach number of 0.7, was used for the wing. Measured aerodynamic characteristics of this airfoil are presented in reference 11. The nondimensional coordinates of the airfoil are listed in table 1, and a sketch of the airfoil shape is presented at the bottom of figure 6(c). The wing had no twist, with the result that a straightforward installation of the air passages was possible. The wing was mounted on a body such that it would be outside the test section sidewall boundary layer.

The body, shown in figure 6(a), was formed in three parts: a forward section, a center section, and an aft section. The forward section, which was 8.00 in. long, consisted of a half-body of revolution outboard and 6.78-in-wide panels inboard. The aft section of the body, which was 10.00 in. long, consisted of a half-body of revolution outboard and 6.78-in-wide panels inboard. Coordinates of the forward and aft sections are listed in table 2. The center section of the body, which was 32.50 in. long, consisted of a semicircle with a diameter of 6.25 in. outboard and 6.78-in. flat panels inboard. The opening for the wing was rectangular and slightly larger than the wing root. Foam rubber was bonded to the wing within the body to form a seal to prevent flow into or out of the body opening and to minimize seal tare loads on the balance.

The semispan wing was mounted inverted on a five-component strain gauge balance secured to the model-support turntable by a balance support block within the body, as shown in figures 5(b) and 6(b). The body was not supported by the balance. Two thin-walled hard-wall tubes were connected to the balance support and wing root to serve as the air supply lines. The tubes were bent into coils looping back and forth within the body, as shown in figure 5(b). The coils provided extra length to ease the stiffness between the nonmetric balance support block and metric wing. Experiences with such an arrangement have produced repeatable data.

Previous experiments showed that blowing from the tip jet increases the lift over much of the wing. These wings had small aspect ratios so that for a rectangular wing with an aspect ratio of 2, the effect of blowing was detected for about 1 chord inboard from the wingtip. The effect of tip blowing on the local lift several wingtip chords from the tip should be small. Therefore, chordwise rows of pressure orifices were concentrated over the outer portion of the wing. Five rows of pressure orifices were installed in the model at $\eta = 0.25$, 0.50, 0.70, 0.80, and 0.90. Each orifice had a diameter of 0.010 in. and was drilled normal to the wing surface. A sketch showing the nominal orifice locations is presented in figure 6(c), and measured nondimensional orifice locations are listed in table 3. Each chordwise row consisted of 20 orifices on the upper surface extending from the leading edge back to 90 percent chord and 19 orifices on the lower surface extending from 2 percent chord back to 90 percent chord. The wing was too thin aft of the 90-percent-chord position to install any orifices there. Results from two-dimensional tests of this airfoil section presented in reference 11 indicate that little loading occurs on the rear portion of the airfoil when the flow is attached. By assuming that little or no trailing-edge separation occurs, the absence of orifices aft of the 90-percent-chord location should have little effect on the computation of the section lift coefficient.

The model was designed with removable wingtip sections, shown in figure 6(b), to allow testing of different wingtip blowing parameters. Each wingtip section had a forward plenum and an aft plenum and each plenum was supplied with high-pressure air by a separate air passage in the wing. A 0.020-in. inside-diameter tube was routed through each air passage and ended in a hook or "J" located in the plenum to measure the total pressure. Each plenum supplied high-pressure air to a single jet exit. By using separate plenum chambers, each jet could be operated separately.

Six interchangeable wingtip sections were used to investigate systematically the effects on the aerodynamic characteristics of jet vertical location, chordwise location, in-plane deflection (sweep), out-of-plane deflection (dihedral), and chordwise length. The nomenclature used to define the jet geometry is defined in figure 7 and details of each tip are presented in figure 8. Each tip was assigned an identifying number; thus, the missing numbers denote tips that were designed but not fabricated because of problems in the manufacturing process. The original numbering system is retained in this report to be consistent with that in reference 9. Each small-chord jet was 0.062 in. high and 0.25 in. long ($c_j/c_{tip} = 0.062$). Jets were centered at nominally the 20-, 30-, 50-, 60-, and 70-percent-chord locations. One tip was fabricated with two jets with a longer chord (fig. 8(e)) to approach the continuous jets used in many of the previous exploratory experiments. The attachment hardware and fabrication process of the wingtip imposed constraints on

the length and location of the two long-chord jet exits. The length of the long-chord front jet was selected to cover the two short-chord jet locations designed for the front wingtip plenum chamber. The length of the rear jet was selected to cover the four short-chord jets designed for the rear wingtip plenum chamber. The jet height was 0.062 in. and both jets exhausted in a spanwise direction. The length of the forward jet was 0.620 in. ($c_j/c_{tip} = 0.155$), and the length of the rear jet was 1.50 in. ($c_j/c_{tip} = 0.375$). A summary of the jet parameters for each tip is presented in table 4, and schematic diagram showing the available jet locations for comparisons is presented in figure 9.

Instrumentation

Measurements were required of the wing forces and moments, wing surface static pressures, jet mass-flow rate, pressure, temperature, and wind tunnel test conditions. Wing forces and moments were measured by a five-component strain gauge balance, but wing side force was not measured. All balance strain gauges were temperature compensated, and the balance was calibrated for the first- and second-order balance component interactions.

Wing surface static pressures were measured by an electronically scanned pressure (ESP) measurement system with a transducer dedicated to each orifice. Each transducer measured a differential pressure. Tunnel free-stream static pressure was used as the reference pressure for the static pressure measurements. All wing pressures were measured at virtually the same time that the rest of the data were measured.

Pressure and temperature instrumentation were used with the air supply system to determine the jet momentum and to correct the balance data for the effect of the pressurized air lines. A schematic diagram of the air supply system and associated instrumentation is presented in figure 10. Differential pressure transducers were connected to each air line just upstream of the rigid attachment to the balance support. These air line pressures were used to correct the balance data for the effect of pressure on the air line static load. Differential pressure transducers were connected to the "J" tubes installed in the two wingtip plenum chambers. The plenum total pressure and free-stream static pressure were used to determine the momentum of each jet. The volume flow rate of each tip jet was measured by separate turbine flowmeters, and static pressure and temperature at the inlet of the flowmeters were measured to determine the gas density. Flowmeter inlet static pressure was measured with an individual differential pressure transducer, whereas flowmeter inlet temperature was measured with a thermocouple. Mass-flow rate was determined from the density of the high-pressure air and the volume flow rate of each air line.

Tunnel static and total pressures were measured by quartz bourdon-tube pressure transducers. This same type of transducer was used to measure the reference pressure used for the electronically scanned pressure modules and the differential pressure transducers. These quartz pressure transducers were referenced to a vacuum to provide absolute pressure measurements.

The model angle of attack was measured with an accelerometer mounted on the wing root, as shown in figure 5(b). The sensor provided the actual wing angle of attack so that no corrections were required for model support bending.

Model Calibrations and Corrections

Corrections for Stiffness and Pressure of Air Lines

The presence of the air lines provides load paths for the wing forces and moments in addition to the one through the balance. The effects of stiffness and pressure of air lines must be determined so that they can be removed from the balance data. Air line stiffness can change with pressure, and air line pressure will tend to unwind the coils in the air line, thus changing the air line static load on the balance. In order to determine the tare, the wingtip section was removed and a loading bar was attached to the end of the wing. With the air lines disconnected from the wing root, known loads were applied to the wing and balance. The air lines were then connected to the wing root and the loadings were repeated both with and without pressure in the air lines. The difference in the measured results was the effect of the air line stiffness on the balance calibration.

Air line pressures used in this investigation, which were generally less than 110 psi, were too small to have a measurable effect on the air line stiffness. Each air line was then pressurized separately to determine the effect of pressure on the static loads on the balance by unwinding the air line coils. Details of the calibration procedures for air line stiffness and the results from the calibration may be found in appendix A of reference 9.

Jet Momentum Calibration

The momentum of the tip jets could not be measured in all three directions because there was no side-force component on the balance, and thus an alternate means of determining the jet momentum was used. A rake with five total pressure tubes spaced over the width of the jet exhaust was used to survey across the jet exhaust. Ambient pressure, jet total temperature, and five jet total

pressures were measured and used to compute the density and velocity of the jet exhaust at multiple positions in a plane normal to the jet exhaust. Jet momentum per unit width of jet was determined by integrating across the jet height the product of the density and velocity squared for each of the five total pressure tubes. Jet momentum (thrust) was computed by integrating the variation of the jet momentum per unit width across the width of the jet exhaust. This process was repeated for several different plenum pressures. The integrated jet momentum was calibrated as a function of the difference between the total pressure measured in the jet plenum and the ambient static pressure. Details of the calibration procedures, derivation of the equations used to compute the jet momentum, and the calibration measurements are presented in appendix B of reference 9.

Test Procedures and Data Reduction

Accurate and repeatable drag measurements on the wing with tip blowing were crucial to the success of this investigation. Viscous drag on the wing will change if the boundary-layer transition point changes. The transition location on the wing upper and lower surfaces was fixed by using a strip of carborundum grit. The grit location was determined by using the method of reference 12, and a sketch indicating the size and location of the transition strips is presented in figure 11.

Each tip was tested without blowing at angles of attack from −2.0° to 11.0° at a Mach number of 0.30. This established a baseline for each tip to eliminate the effects of any minor manufacturing differences among the tips. Then, each tip was tested at the same nominal free-stream Mach number and angles of attack with maximum blowing from the front jet alone, the rear jet alone, and from both jets for only tip 8. The maximum jet-exit Mach number, which was limited to 0.90 to eliminate potential noise and fatigue problems associated with a supersonic jet, restricted the maximum jet momentum for the tips with the short-chord jet exits. The maximum pressure and mass-flow rate of the air supply system limited the maximum jet momentum for tip 8 with the long-chord jets (because of the larger jet-exit area). Tip 8 was tested at a constant angle of attack of about 2° while the tip jet momentum was varied from 0 to the maximum value at free-stream Mach numbers of 0.20, 0.30, 0.40, and 0.50. Testing at a Mach number of 0.72 without blowing was limited to an angle-of-attack range from −2.0° to 1.0° by the balance rolling-moment limit. At each test condition, the balance forces and moments, wing surface static pressures, free-stream test conditions, plenum pressure, air line pressure, flowmeter turbine rotational speed, flowmeter temperature, and flowmeter pressure for each jet were recorded.

The wing balance data have been corrected for weight tares, first- and second-order balance component interactions, and air line stiffness and pressure tares. Data were resolved about a moment reference center located along the wing-body juncture at the quarter-chord location of the mean aerodynamic chord, as shown in figure 6(a). All balance data have been converted to coefficient form. Wall interference corrections were computed by using the technique of reference 13 and were found to be negligible.

Jet momentum coefficient as well as the jet contributions to the wing lift, drag, root bending moment, and pitching moment were computed from the jet calibration. These direct thrust effects were subtracted from the measured balance quantities to obtain the wing force and moment results. An equivalent ram drag was computed from the jet mass-flow rate and free-stream velocity. The computed ram drag has been added to the wing drag to obtain the wing total drag. Unless specifically noted otherwise, the drag coefficients presented for the wing do not include the ram drag.

Wing pressure data have been referenced to the free-stream static pressure and nondimensionalized by the free-stream dynamic pressure. Pressures at the two rearmost pressure orifices on the wing upper and lower surfaces were used to extrapolate linearly to the pressure at the wing trailing edge. The wing-surface static pressure coefficients have been integrated in the chordwise and normal directions to obtain the section normal-force and chord-force coefficients. These coefficients were used to obtain the section lift coefficient for each chordwise row of orifices.

Presentation of Results

The wing longitudinal force and moment coefficients are presented in coefficient form in the stability-axis system, and the wing-root bending-moment coefficients are presented in the body-axis system. (See fig. 12.) The reference area for the coefficients was the exposed planform area, the reference length for the wing-root bending-moment coefficient was the distance from the exposed wing root to the tip, and the reference length for the pitching-moment coefficient was the mean aerodynamic chord.

The results from this investigation are presented as follows:

Discussion

Data Accuracy and Repeatability

The accuracy of the wing force and moment data depends on the accuracy of the balance and angle-of-attack measurements. The quoted balance accuracy is 0.5 percent of the full-scale balance load, which equates to 2.0 lbf normal force, 0.15 lbf axial force, 10.0 in-lbf pitching moment, and 5.0 in-lbf rolling moment. A typical accuracy of the angle-of-attack measurement is about 0.02°. For small angles of attack, the drag accuracy depends primarily on the axial-force measurement and the lift accuracy depends primarily on the normal-force measurement. At a Mach number of 0.30 and small angles of attack, the lift-coefficient accuracy is 0.016, the drag-coefficient accuracy is 0.0012, the pitching-moment-coefficient accuracy is 0.011, and the wing-root bending-moment coefficient (rolling-moment) accuracy is 0.002.

The repeatability of the wing force and moment data is affected by problems associated with the two air lines that cross the balance. The design of the air supply system and the test procedures used in these tests attempted to minimize the problems with mechanical connections, nonuniform expansion and contraction with temperature, changes in the static loads with air line pressure, and hysteresis. The repeatability of the wing data was investigated by retesting two of the wingtip sections. The results are presented in figure 13 for tips 2 and 8 at a Mach number of 0.30. These tests were conducted with the air lines attached so that the repeatability of the results would be representative of those obtained with tip blowing. Tip 2 was tested two times, and tip 8 was tested three times. The different sets of measurements for each

tip will be referred to by a run number. Runs 2 and 3 for tip 8 were measured sequentially in the test program without stopping the tunnel flow.

The repeatability of the wing lift data without blowing for tip 2 and the sequentially measured results for tip 8 are in excellent agreement. The sequentially measured results for tip 8 (runs 2 and 3) differ from the results for tip 8 obtained earlier in the test (run 1). The difference in lift coefficient at the same angle of attack is about 0.015, which is just within the lift-coefficient accuracy of 0.016. A linear least-squares curve was fitted to the linear portion of each data set to obtain the angle of zero lift (α_0) and the lift-curve slope (C_{L_α}). (The results are included in table 5.) Except for tip 8 (run 1), the repeatability of the results for a given tip is very good.

For tip 2, the difference in the drag coefficient between the curves at low lift coefficients is about 0.0010, and the difference decreases as the angle of attack increases. The lower drag for run 2 is not consistent with the drag obtained on other tips without blowing, but the difference is still within the expected accuracy. Results for tip 8 that were measured sequentially (runs 2 and 3) are in good agreement, especially at the lower lift coefficients. However, results obtained earlier in the test (run 1) show larger differences in the drag as the lift increases. An examination of the raw millivolt data indicates that the model was probably not precisely at an angle of attack of 0° when the reference readings were recorded for run 1 with tip 8. The difference is probably attributable to an error of about 0.1° in setting the model attitude for recording the reference conditions at which the model is assumed to be at an angle of attack of 0°. However, the differences between the results are still within the quoted balance accuracy.

For the untwisted wing tested in this investigation, the section lift coefficient at each spanwise station will approach zero as the angle is attack is reduced to the angle of zero lift. With no lift across the wing, the wing-root bending moment should also be zero. As the angle of attack increases, the lift at each spanwise station increases linearly with the angle of attack. The wing-root bending moment should also vary linearly with angle of attack and lift because the wing-root bending moment is the integral of the product of the section lift and spanwise location on the wing. The variation should be linear as long as the flow is attached.

The repeatability of the results from tip 2 for wing-root bending moment and of the sequentially measured results from tip 8 is very good. Again, run 1 for tip 8 does not agree very well with the other two runs. The nonzero wing-root bending-moment coefficient at zero lift from run 1 for tip 8 differs slightly from that for the other two runs. This is additional evidence that the reference model attitude for run 1 for tip 8 was incorrect. A linear least-squares curve was fitted to the linear portion of each data set to obtain the slope $\left(C_{B_{C_L}}\right)$ and intercept $(C_{B,0})$ of the wing-root bending-moment curves, and the results are included in table 5. For each tip, the repeatability of the computed slopes of the bending-moment curves is very good.

The moment reference center was located at the quarter-chord of the mean aerodynamic chord, which should be close to the aerodynamic center. Thus, the slopes of the pitching-moment curves are small until separation begins. Although some scatter exists in the results from tip 2 for pitching-moment coefficient at the lower lift coefficients, the curves are in reasonable agreement. The sequentially acquired results from tip 8 are in good agreement, but the results for run 1 are shifted. All results are well within the quoted pitching-moment-coefficient accuracy of 0.011. A linear least-squares fit was applied to the results over the same linear portion of the curve to determine the pitching moment at zero lift, $(C_{m,0})$ and the slope $\left(C_{m_{C_L}}\right)$, and the results are included in table 5. The repeatability of the slopes is very good, although a very small shift in pitching moment occurs between the runs.

The differences that appear in the results are larger for runs that were not measured sequentially. Whenever practical, the effect of tip blowing will be determined by the difference between results with and without tip blowing measured sequentially in order to minimize these differences. From the limits of data accuracy and data repeatability, changes in the force and moment coefficients due to blowing that are less than quoted accuracy should not be considered significant.

The repeatability of the chordwise pressure distributions at each of the five spanwise stations is presented in figure 14 for tip 2 at nominal angles of attack of 4.0° and 8.0°. The accuracy of the transducers in the electronically scanned pressure modules is typically quoted to be 0.15 percent of the transducer full-scale rating. At a Mach number of 0.30 and a dynamic pressure of 125 psf, the accuracy of the pressure coefficient is better than 0.01. As can be seen from the plots, such accuracy is not distinguishable on the scales used. For all five wing stations, the chordwise pressure distributions are in excellent agreement with each other.

The chordwise pressure distributions from figure 14 were integrated to obtain the section lift coefficient at each spanwise station. These integrated results are presented in figure 15 for tip 2 at the same two nominal angles of attack of 4.0° and 8.0°. As expected, the

repeatability of the spanwise variation of the section lift coefficient is excellent.

Wing Aerodynamic Characteristics Without Blowing

The airfoil section (NASA HSNLF(1)-0213) used for the semispan wing was designed to achieve long runs of laminar flow on both surfaces at a section lift coefficient of 0.2 and a Mach number of 0.70. Two-dimensional test results (ref. 11) of the NASA HSNLF(1)-0213 airfoil section at a Mach number of about 0.30 indicate that the airfoil lift curve is linear up to an angle of attack of about 6° where trailing-edge separation begins. Separation moves forward with increasing angle of attack. At stall, leading-edge suction is still present.

Each tip was tested at a Mach number of 0.30 without blowing. Typical results of the wing aerodynamic characteristics without wingtip blowing are presented in figure 16 for tip 8. Selected wing aerodynamic characteristics without blowing for each wingtip configuration are summarized in table 5. The results from all the tips are similar, although small differences in the aerodynamic characteristics exist as was noted in the section describing the data repeatability. The lift curve is linear with angle of attack up to an angle of attack of about 4.0° (a lift coefficient of about 0.55) with an average slope of 0.101 per degree and an average angle of zero lift of about −1.4°. At higher angles of attack, the slope is reduced from that obtained over the linear portion because of increasing trailing-edge separation. Maximum lift coefficient was not determined because the maximum angle of attack tested was below the stall angle.

The average wing drag coefficient at zero lift is about 0.0104. The change in drag is relatively small for lift coefficients up to about 0.40, but it increases rapidly as the lift increases above that level because of the increase in profile drag due to trailing-edge separation and because the induced drag increases with the square of the lift coefficient.

Wing-root bending-moment curves are linear for lift coefficients up to about 0.55 with a ratio of bending moment to lift of 0.42. At higher lift coefficients, the ratio is reduced, with the change in the ratio occuring at about the same lift coefficient at which the change in lift-curve slope occurs. Over the linear portion of the curve, the spanwise center of lift is located at about the 42-percent-semispan location, although at higher lift coefficients, the center of lift moves inboard. The average wing-root bending-moment coefficient at zero lift is virtually zero.

The variation of pitching-moment coefficient with lift coefficient is nearly linear up to lift coefficients of 0.55, with an average slope of about 0.005. The average pitching-moment coefficient at zero lift is −0.013, which is very close to the value (−0.012) obtained in the two-dimensional airfoil tests (reported in ref. 11) at slightly different test conditions. Results from the lift, wing-root bending-moment, and pitching-moment coefficients all indicate that attached flow is maintained up to a lift coefficient of about 0.55 and that the separation begins at the trailing edge.

Chordwise pressure distributions at a Mach number of 0.30 are presented in figure 17 for tip 8 with no blowing at angles of attack from 0° to 10.0° for all five spanwise stations. These results are typical of those for all the tips. At an angle of attack of −0.1°, the measured chordwise pressure distributions generally show a favorable pressure gradient back to at least the 55-percent-chord location on both surfaces of the airfoil. The acceleration over the upper surface of the leading edge has been reduced so that there is no large suction peak followed by an adverse pressure gradient. At this angle of attack, the region aft of the 65-percent-chord location is providing little, if any, lift. Flow on both surfaces decelerates over the rear portion of the airfoil and appears to be attached to at least the aftmost measurement station (the 90-percent-chord location).

At an angle of attack of 2.1°, a more rapid acceleration occurs around the leading edge of the upper surface, which is followed by a region with a small adverse pressure gradient. Again, the rear portion of the airfoil is providing little lift. As the angle of attack increases to 4.0°, a stronger suction peak develops and the boundary layer on the upper surface is subjected to a much larger adverse pressure gradient than at the lower angles of attack. The pressure coefficients on the upper surface at $x/c = 0.90$ begin to diverge from those on the lower surface at an angle of attack of about 4.0°, a result suggesting that a separated region is forming near the trailing edge. This is consistent with the break in the lift and pitching-moment curves at 4.0°.

At an angle of attack of 6.0°, signs of separation appear on the upper surface between the 80- and 90-percent-chord locations because the pressure distribution ahead of the trailing edge is flattened and less positive (more negative). Separation probably begins at a lower angle of attack, but the absence of pressure orifices aft of the 90-percent-chord position prevents its detection. The upper surface pressure distributions indicate that the suction on the midchord region of the upper surface decreases from the inboard to the outboard wing stations. At angles of attack of 8.0° and 10.0°, the leading-edge suction continues to increase and the

location of the start of the separated-flow region moves farther forward. The leading-edge suction peak was maintained to the maximum angle tested.

The spanwise variations of the integrated section lift coefficient associated with these chordwise pressure distributions were computed, and the results are presented in figure 18. As the angle of attack increased, the section lift coefficient increased across the wingspan. At the inboard station, the change in section lift coefficient with angle of attack (section lift-curve slope) was roughly constant. At the outer stations, the change in section lift coefficient with angle of attack became smaller as the angle of attack increased, and during this increase, the lift on the outboard portion of the wing did not increase as much as the lift on the inboard portion. Thus, the center of lift moved inboard as the angle of attack and lift increased.

Effect of Spanwise Blowing on Wing Aerodynamic Characteristics

Each interchangeable wingtip section was tested on the wing at a Mach number of 0.30 both without and with blowing from the forward jet, rear jet, and both jets (tip 8 only). The angle of attack for each of these four conditions was varied from −2.0° to 11.0°. For the tips with the short-chord jet exits (0.25 in. long), the maximum jet momentum coefficient was limited by the assumption that the maximum jet-exit Mach number was 0.90. For the jet exits with a longer chord on tip 8, the maximum jet momentum coefficient was limited by the air supply system. In addition, tip 8 was tested at a constant angle of attack of 2.0° with varying jet momentum coefficient. These additional tests were conducted at Mach numbers of 0.20, 0.30, 0.40, and 0.50 with blowing from the forward jet, rear jet, and both jets. By changing the wingtip, the effect of exhaust location and direction could be investigated. (See fig. 9.) Results from the different tips with and without blowing have been grouped to look at the effect of jet chordwise location, vertical location, in-plane deflection, and out-of-plane deflection. Direct comparisons of results with the jet on and the jet off will be used to determine the effects of blowing.

The effect of blowing at several chordwise locations on the wing lift and drag coefficients is presented in figure 19. The five available chordwise locations are shown above each figure with the location of the operating jet noted by the darkened jet exit. Results show that no significant changes in the wing lift occur with the addition of blowing. The small changes in the drag coefficients with the addition of blowing are all less than the measurement accuracy, and they do not show any consistent trend with jet chordwise location.

The effect of blowing at two jet vertical locations on the wing lift and drag coefficients is presented in figure 20. The available exit locations are shown in the sketches with the operating jet exit darkened. The addition of blowing does not have a measurable effect on the wing lift. The results show a small possible decrease in the drag coefficient with the jet displaced vertically upward for jets located at approximately $0.3c_{tip}$. The decreases, which are smaller than the balance accuracy and data repeatability, should be considered only as a possible trend. This trend is consistent with published results (ref. 2) for wings having a lower aspect ratio, which indicated that displacing the jet upward had a larger induced effect than having the jet on the wingtip centerline.

The effect of redirecting the jet exhaust downward (out of the wing plane) on the wing lift and drag coefficients is presented in figure 21. The components of the jet thrust in the lift and drag directions have been removed from the data. The jet-exit location is shown in the sketches. The exhaust direction in the *XZ*-plane is indicated by the arrow with the jet deflection angle noted. The undeflected jet results ($\delta_j = 0°$) show no measurable effect of blowing. Results with the jet deflected downward ($\delta_j = 20°$) show a very small possible increase in the lift coefficient and a decrease in the drag coefficient. Because both of these changes are much smaller than the balance accuracy and data repeatability, they should be considered only as a possible trend. However, this trend is consistent with published results (ref. 2) which indicate that deflecting the jet downward has a larger induced effect than an undeflected jet on the wingtip centerline.

The effect of redirecting the jet blowing downstream (in the wing plane) on the wing lift and drag coefficients is presented in figure 22. The components of the jet thrust in the lift and drag directions have been removed from the results. The available jet locations and exhaust directions in the *XZ*-plane are presented in the sketches with the operating jet exit darkened. The undeflected jet results ($\psi_j = 0°$) show no measurable effect of blowing. With the jet deflected rearward ($\psi_j = 30°$), blowing leads to a very small increase in lift. Results also show a small decrease in drag coefficient for the front jet location and a small increase for the rear jet location. The magnitudes of the changes are about the same as the balance repeatability and measurement accuracy.

Maximum jet momentum coefficients for the short-chord jets were established by limiting the maximum jet-exit Mach number to 0.90. The effects of blowing on the wing lift and drag could be larger if the jet momentum coefficient was increased. As noted previously, the jet momentum coefficient was dependent on the jet-exit area

and velocity. Because increases in the jet-exit velocity to supersonic values were not desirable, the jet-exit area was increased by increasing the chordwise length of the front and rear jets to define tip 8. The increased jet-exit area increased the maximum momentum available from each jet. Results for the jets with a longer chord are presented in figure 23. The addition of blowing produced definitive results, with reductions in the drag coefficient of about 0.0012 for the front jet and of about 0.0022 for the rear jet. These drag reductions were larger than the accuracy and repeatability of the balance drag measurement. Blowing from the long-chord jets had little effect on the lift measurements.

None of the results from the short-chord jets (0.25 in. long) yielded reductions in drag coefficient that were larger than the balance accuracy and data repeatability. However, results from the long-chord jets (both 0.62 in. long and 1.50 in. long on tip 8) yielded significant drag reductions, thereby warranting additional analysis. The effect of blowing individually and simultaneously from the long-chord jets on the wing aerodynamic characteristics is presented in figure 24. Curve fits were applied to the variation of lift coefficient with angle of attack with and without blowing (fig. 24(a)) to determine the lift-curve slopes. For the linear portion of the curve, the lift-curve slope increased from 0.103 per degree without blowing to 0.108 per degree with blowing from both jets. This increase was about the same as the accuracy of the determination of the slope over this small angle range. At angles of attack above the break in the lift curve, the lift coefficient with blowing was greater than the lift coefficient without blowing. The jet exhaust probably inhibited the local flow from wrapping around the wingtip, thus allowing a higher load to be carried near the tip.

The ratio of the wing-root bending-moment coefficient to the lift coefficient with and without blowing (fig. 24(b)) was computed for the linear portion of the curve to determine the spanwise center of lift. With attached flow, the spanwise center of lift moved outboard from $\eta = 0.42$ without blowing to $\eta = 0.43$ with blowing from both jets. A similar movement in the center of lift with blowing was noted at the higher angles of attack where the curves were nonlinear, a result indicating that blowing increased the loading over the outer portion of the wing.

The increased lift outboard with blowing led to a negative increment in the pitching-moment coefficient (fig. 24(c)) because the tip region was aft of the moment reference center. For the range of lift coefficients associated with attached flow, the slope of the pitching-moment curve changed from 0.005 without blowing to −0.015 with both jets blowing. The drag reduction with blowing (fig. 24(d)) was about 0.0012 for the front jet, 0.0022 for the rear jet, and 0.0025 for both jets operating.

When applied to an aircraft, a source for the high-pressure air for the blowing must be identified. If high-pressure air must be bled from the propulsion system, the ram drag must be added to the wing drag. (The ram drag is equal to the product of the mass-flow rate of the jet and the free-stream velocity.) After adjusting for this ram drag penalty (as shown in fig. 24(e)), the differences with the jets operating are small and mixed. In fact, the differences are of about the same magnitude as the accuracy of the drag measurement. Comparisons of the chordwise pressure distributions and spanwise lift distributions for these cases are not practical because of the small differences in the angle of attack for the blowing-off and blowing-on data points.

The decrease in drag and the possible small increase in lift due to spanwise blowing from the jets with a longer chord were large enough to warrant additional tests at several Mach numbers in which the angle of attack was fixed at 2.1° and the jet plenum pressure was varied to investigate the effect of jet momentum coefficient. As noted previously, the maximum jet momentum was limited by the air supply system for the jets on tip 8. As the Mach number and free-stream dynamic pressure increased, the maximum available jet momentum coefficient decreased, a result leading to very small jet momentum coefficients at Mach numbers of 0.40 and above. Variation of the wing lift and drag coefficients with jet momentum coefficient is presented in figure 25 for several Mach numbers with the front jet, rear jet, and both jets operating. At a Mach number of 0.20, lift increased with increasing jet momentum coefficient for all three jet operating conditions. Drag decreased with increasing jet momentum coefficient for blowing from the rear jet alone and for blowing from both jets operating simultaneously, but it increased slightly for blowing from the forward jet alone. At Mach numbers of 0.30 and 0.40 (figs. 25(b) and 25(c)), the lift coefficient increased and the drag coefficient decreased with increasing jet momentum coefficient for both the front and rear jet operating conditions. The small change in jet momentum coefficient and scatter in the data made it difficult to determine the effect of blowing on the lift or drag coefficients at a Mach number of 0.50 (fig. 25(d)).

Spanwise variation of the section lift coefficients and chordwise pressure distributions provides additional information about the flow field near the wingtip with blowing. The effect of blowing on the spanwise distribution of the section lift coefficient is presented in figure 26 for Mach numbers of 0.20, 0.30, 0.40, and 0.50 at a constant angle of attack of 2.1°. Without blowing, the section lift coefficient increases across the wing to the

70-percent-semispan location, and then it decreases toward the tip. In general, blowing does not have a measurable effect on the lift at spanwise stations out to $\eta = 0.70$. Increasing the jet momentum coefficient increases the section lift coefficient at $\eta = 0.90$ and, to a lesser degree, at $\eta = 0.80$. Increases are largest at the lowest Mach number where the jet momentum coefficient was the largest.

The section lift coefficient at $\eta = 0.90$ was cross-plotted against the jet momentum coefficient for each Mach number. The results, which are presented in figure 27, show that at all four Mach numbers, the section lift coefficient near the tip increases with jet momentum coefficient for all three blowing configurations. At the lower Mach numbers, the increase in section lift coefficient with blowing is larger for the front jet than for the rear jet.

The effect of spanwise blowing on the chordwise pressure distribution is very small. Differences in the chordwise pressure distribution are difficult to discern with the scales typically used for the plots. Therefore, the change in pressure coefficient due to blowing that is, ($\Delta C_p = C_p$ (with blowing) $- C_p$ (without blowing)) will be used rather than the pressure coefficient itself. Data were recorded at a constant angle of attack without blowing followed immediately by data with blowing. The change in the local pressure coefficient with blowing was computed at $\eta = 0.90$, and the results are presented in figure 28. In general, spanwise blowing increases the suction on the upper surface ($-\Delta C_p$) and increases the pressure on the lower surface ($+\Delta C_p$). The magnitude of the change in the pressure coefficient is generally larger for the higher jet momentum coefficient, a result suggesting a small increase in the local angle of attack due to blowing. The effect of blowing is usually larger on the upper surface than on the lower surface. Blowing from the front jet produces a larger change in the leading-edge suction peak than blowing from the rear jet; also, the effect of the front jet on the pressure coefficients is larger than the effect of the rear jet. The front jet increases the suction across most of the chord, and the rear jet tends to have most of its effect on the aft portion of the chord.

As the Mach number and dynamic pressure increased, the maximum available jet momentum coefficient (C_μ) decreased, but the maximum C_μ achievable at a Mach number of 0.72 was too small for practical experiments. A Navier-Stokes solver, modified to simulate spanwise blowing at the wingtip, was used to extend the experimental results to a higher Mach number.

Navier-Stokes Calculations With Simulated Blowing

Previous experimental investigations (refs. 2–4, 6, and 7) indicated that spanwise blowing from the wingtip modifies the flow field near the wingtip and in the wake. Because the effects of viscosity are expected to be important, a Navier-Stokes simulation of the flow field is needed. Thus, an existing Navier-Stokes solver, TLNS3D, which has demonstrated the ability to simulate the flow field about moderate aspect ratio wings realistically at transonic Mach numbers, was selected for use in the study. The computer code, described in references 14 and 15, solves the unsteady Navier-Stokes equations numerically on a grid of control points until steady-state conditions are obtained. A finite volume representation of the equations is written in discrete form in general, curvilinear coordinates. A thin-layer assumption is used to simplify the equations because most of the viscous diffusion is normal to the wing surface. A body-fitted coordinate system was selected with the three coordinate directions in approximately chordwise, normal, and spanwise directions. The solution is advanced to steady state by using a modified, five-stage Runge-Kutta time-stepping scheme developed by Jameson, Schmidt, and Turkel in reference 16. Acceleration techniques, such as local time stepping and multigrid, are employed to improve the numerical convergence. The system of equations is closed with the addition of an eddy viscosity and eddy conductivity for the momentum and energy equations and the algebraic turbulence model of Baldwin and Lomax (ref. 17), a model that works well for attached or mildly separated flows.

A grid-convergence study was performed to determine an acceptable grid for the Navier-Stokes calculations. The Navier-Stokes solver was used to predict the wing aerodynamic characteristics without blowing at Mach numbers of 0.30 and 0.72 to demonstrate that the grid and code are suitable for calculations of the configuration used in this study over the desired Mach number range. The solver was also used to predict the effects of blowing at a Mach number of 0.30 to calibrate the modifications used to simulate the wingtip jet. The calibrated solver was then used to predict the effect of spanwise blowing from the wingtip at a Mach number of 0.72. A summary of the grid-convergence study, the calibration of the solver without blowing at Mach numbers of 0.30 and 0.72, and the calibration of the modifications to simulate blowing are discussed in the appendix.

Calculations at a Mach number of 0.30 with corrections for the effect of the body were in good agreement with results from the current experiment. (See the

appendix.) The computations showed that blowing increases the suction over part of the upper surface and the pressure over the lower surface of the wing near the tip. Blowing was also found to increase the section lift coefficient near the wingtip and the total wing lift. Results from calculations presented in reference 9 indicated that the code also predicts particle paths near the wingtip and near the jet that are similar to those obtained in a water tunnel. Calculations successfully predicted that blowing displaces and diffuses the wingtip vortex. The only trend not predicted correctly by the Navier-Stokes solver with simulated blowing was the wing drag. Because the code predicts the results without blowing at Mach numbers of 0.30 and 0.72 and with blowing at a Mach number of 0.30, it can be used with reasonable confidence to predict the effects (except for drag) of spanwise blowing from the wingtip at a Mach number of 0.72.

The Navier-Stokes solver was used to compute the flow field about the wing with tip 8 at a Mach number of 0.72 at an angle of attack of 1.0°. The jet-exhaust velocity was limited to a Mach number of 0.90. This effectively determined the maximum jet momentum coefficient for a fixed jet-exit area. Initial calculations were performed without and with blowing from the front jet, rear jet, and both jets at the maximum exit velocity. For these initial cases, the jet exhausted in the spanwise direction. Additional computations for both jets operating were performed at the maximum jet-exit velocity with the jets deflected downward 30°.

The effect of blowing from the front jet on the chordwise pressure distributions is presented in figure 29(a) for two spanwise stations: $\eta = 0.90$ and $\eta = 0.98$. Because of the larger free-stream dynamic pressure for the higher Mach number, the jet momentum coefficient is only 0.0012. At $\eta = 0.90$, the effects of blowing are very small, but close to the tip ($\eta = 0.98$), blowing reduces the suction on the upper and lower surfaces at stations ahead of the jet ($x/c < 0.23$). Suction increases on both surfaces across the length of the jet ($0.23 < x/c < 0.38$), and higher suction pressures are maintained aft of the jet on the upper and lower surfaces.

The effect of blowing from the rear jet on the chordwise pressures is presented in figure 29(b) at the same spanwise stations. At $\eta = 0.90$, the effects are small except for the reduced pressure recovery near the trailing edge, but close to the tip at $\eta = 0.98$, blowing induces larger changes in the pressure distribution. The changes due to blowing from the rear jet are similar in character to those found for the front jet. Suction is reduced ahead of the jet ($x/c < 0.51$), but along the length of the jet, the suction increases until the pressure recovery begins. With blowing, the pressure recovery near the trailing edge is less than that found without blowing.

The effect of blowing from both jets on the chordwise pressure distributions is presented in figure 29(c). At $\eta = 0.90$, the change in the pressure distribution with both jets has the same character found for the front and rear jets alone, but with a slightly larger magnitude. Near the tip at $\eta = 0.98$, effects from both jets can be seen. On the forward portion of the chord, blowing from the front jet reduces the suction on the upper and lower surfaces, and the suction level increases across the front jet. On the rear portion of the chord, blowing leads to a larger increase in suction and a smaller pressure recovery than that found for the rear jet alone.

The particle paths on the upper surface with and without blowing are presented in figure 30. The darker shading on the wing surface marks the concave portion of the upper surface where the pressure increases. To determine a particle path, a particle is released at a grid point just above the surface grid. The position of the particle is determined at 2000 time steps by integrating the local velocity at the particle location. Short particle paths are an indication of regions of low velocity. Without blowing, particle paths starting from the leading-edge region on the upper surface, shown in figure 30(a), move inboard as they are convected downstream until the rapid compression is reached where they then move outboard. Particles released along the tip move inboard along the forward portion of the chord, and the flow generally moves outboard along the compression region on the aft portion of the tip. Particle paths with blowing from the front jet are presented in figure 30(b) in which the particles starting from the jet exit are noted by the dashed lines. Because the jet momentum is relatively small compared with the momentum of the flow around the tip, the flow from the jet swirls around the tip instead of penetrating into the free stream. The jet flow blocks the flow around the tip and over the upper surface and thus creates a region of low-energy flow, as indicated by the short or absent particle paths. Blowing has only a small effect on the particle paths starting from the leading edge. With blowing from the rear jet, shown in figure 30(c), the jet flow from the downstream part of the jet penetrates farther into the free stream because of the blockage created by the lengthened upstream part of the jet. The particle paths along the forward portion of the tip are initially displaced inboard and are carried up and over the jet exhaust. Particle paths with blowing from both jets are presented in figure 30(d). These results appear to be similar to a combination of the results found for the individual jet-blowing results. Again, a region of low-energy flow is caused by the jet exhaust blocking the free-stream flow.

The spanwise variations of the section lift coefficient without and with blowing from the front jet, rear jet, and both jets are presented in figure 31. The small momentum from the front jet leads to little change in the spanwise variation of the section lift coefficients. For the rear jet, blowing increases the load over the outboard portion of the wing. Results for both jets are practically the same as results for the rear jet alone.

Changes in the section lift coefficient at $\eta = 0.90$ and in the wing lift and drag coefficients with blowing, presented in figure 32, are small. For the front jet, blowing increased the wing drag coefficient but had little effect on the section lift coefficient or the total wing lift coefficient. For the rear jet, blowing increased the section lift coefficient at $\eta = 0.90$ by about 4 percent (from 0.236 to 0.245) and the wing lift coefficient by less than 1 percent (from 0.256 to 0.258). The drag increased because of the increased suction on the rear-facing surface on the aft portion of the chord. Results for both jets were slightly larger than those for the rear jet alone.

The jet exhausting in the plane of the wing tends to swirl around the wingtip, thereby reducing its effectiveness as a fluid end plate. One possible technique to prevent the jet flow from swirling around the tip is to deflect the jet downward to oppose the local momentum. For these calculations, the jet-exit Mach number is maintained at 0.90 and the jet direction is deflected downward 30°. Chordwise pressure distributions near the tip are presented in figure 33 for the undeflected and deflected jets. Deflecting both the front and rear jets downward 30° increases the suction on the upper surface, increases the pressure on the lower surface, and increases the trailing-edge pressure coefficient relative to the undeflected configuration. Particle paths for the deflected jets, shown in figure 34, indicate that the front jet does not swirl around the tip as much with the deflected jet as it does for the undeflected jet, although the low-energy flow region is still present. Particle paths from the tip are not displaced as far inboard as with the undeflected jet. The spanwise variation of the section lift coefficients, shown in figure 35, shows an increase in the loading near the tip, which was expected from the pressure distributions. Deflecting the jets downward increases the wing lift coefficient from 0.262 to 0.264 and reduces the wing drag coefficient slightly.

At high subsonic Mach numbers, blowing slightly increases the loading near the tip and wing lift and also increases the drag. Blowing leads to a separated region near the tip. For the hypothetical transport aircraft described in the "Introduction," the total engine thrust coefficient is about 0.0400. The maximum C_μ investigated with both jets operating represents about 10 percent of the total engine thrust, but the small increase in the wing lift coefficient of about 1 percent does not justify the 10-percent increase in momentum. Thus, for this type of configuration at a high subsonic Mach number, spanwise blowing from the wingtip is not a practical way of increasing lift or reducing drag.

Concluding Remarks

The experiments at low Mach numbers showed that the addition of blowing had little measurable effect on drag for the jets with the short-chord exits for a jet-exit Mach number of 0.90. The jets with a longer chord showed drag reductions ranging from 0.0012 for the front jet to 0.0022 for the rear jet. Blowing from the jets with a longer chord increased the lift-curve slope and moved the center of lift outboard.

Tests of the jets with a longer chord indicated that for moderate lift coefficients and Mach numbers ranging from 0.20 to 0.40, wing lift increased and drag decreased with blowing. However, after accounting for the ram drag penalty, little, if any, total drag reduction occurred with blowing. Blowing increased the section lift coefficient at the 90-percent-semispan location with a very small change at the 80-percent-semispan location. The increase in the section lift coefficient was greatest for the largest blowing coefficient. Spanwise blowing increased the suction on the upper surface and the positive pressure on the lower surface.

Calculations using the Navier-Stokes solver with modified boundary conditions to simulate blowing from the wingtip were consistent with almost all experimental results at low Mach numbers. Calculations at a Mach number of 0.72 showed that blowing increased the loading near the wingtip and increased the wing lift and drag. Deflecting the jet downward increased the suction on the upper surface and the pressures on the lower surface. Jet deflection reduced the region of the jet swirling around the upper surface, a result yielding an increase in lift with no additional increase in drag over that of the undeflected jet.

Because the momentum of the jet was typically greater than the reduction in the wing drag and because the increase in the wing lift due to spanwise blowing was small, spanwise blowing at the wingtip did not appear to be a practical means of improving the aerodynamic efficiency of moderate-aspect-ratio wings at high subsonic Mach numbers.

NASA Langley Research Center
Hampton, VA 23681-0001
March 8, 1995

Appendix

Verification of Navier-Stokes Solver With Simulated Wingtip Blowing

Details of Navier-Stokes Solver

Results from previous experimental investigations indicated that spanwise blowing from the wingtip modifies the flow field near the wingtip and in the wake. Because the effects of viscosity are expected to be important, a Navier-Stokes simulation of the flow field is needed. An existing Navier-Stokes solver computer code, TLNS3D, which has demonstrated the ability to simulate the flow field about moderate-aspect-ratio wings at transonic Mach numbers, was selected for use in the study. This computer code, described in references 14 and 15, solves the unsteady Navier-Stokes equations numerically on a grid of control points until steady-state conditions are obtained. A finite-volume representation of the equations is written in discrete form in general, curvilinear coordinates. A thin-layer assumption is used to simplify the equations because most of the viscous diffusion is normal to the wing surface. A body-fitted coordinate system was selected with the three coordinate directions in approximately chordwise, normal, and spanwise directions. The solution is advanced to steady state by using a modified, five-stage Runge-Kutta time-stepping scheme developed by Jameson, Schmidt, and Turkel in reference 16. Acceleration techniques, such as local time stepping and multigrid, are employed to improve the numerical convergence.

The system of equations is closed with the addition of an eddy viscosity and an eddy conductivity for the momentum and energy equations and the algebraic turbulence model of Baldwin and Lomax (ref. 17). This turbulence model works well for attached flows but is not recommended for separated flows.

Five flow variables must be specified on all boundaries in the computational domain. All computations are performed at the cell centers. Values for cells at the far-field boundary are based on the Riemann invariants for one-dimensional flow normal to the boundary, as outlined by Thomas and Salas in reference 18. Symmetry is imposed on all variables at the plane of symmetry except for the spanwise component of momentum which is antisymmetric. At the downstream boundary, a zero-order extrapolation is used to determine the values of the variables. On the wing surface, no-slip and no-injection conditions are imposed everywhere except at the jet exit where the three components of momentum are specified. Zero normal pressure and density gradients are assumed on the wing surface.

Grid Generation

The grid topology must be able to capture the rapidly changing features in the flow field near the wing surface, wingtip, and across the trailing wake. For the streamwise direction, a "C"-type grid was selected to resolve the viscous effects near the surface and across the downstream wake. For the spanwise direction, an "O"-type grid was selected to capture the features near the wingtip because a previous study on a similar planform wing (ref. 19) indicated that an "H"-type grid with a similar number of spanwise grid points would not resolve the features of the flow as well as an "O"-type grid. Grid points are clustered near the leading and trailing edges of the wing, near the wing surface, and near the wingtip to resolve better the gradients at those locations. The downstream boundary was chosen to be 5 semispans (10 root chords) downstream of the wing-root leading edge. Outer boundaries for the computational space were located five semispans upstream of the wing-root leading edge and five semispans from the plane of symmetry. The grid modeled only the exposed part of the wing from the current experiment, and the body was not included in the grid.

Grid-Convergence Study

The number of cells in each coordinate direction should be sufficiently large such that increasing the number of cells in any of the three grid coordinate directions does not have a significant effect on the wing lift, drag, or pressure distributions. A systematic study of the effect of varying the number of cells in each direction has been conducted to determine the number of cells to be used for the final Navier-Stokes calculations with spanwise blowing. The grid-convergence study was made without any simulated blowing from the wingtip, with details provided in reference 9. As the number of cells in a given direction was increased, the spacing of the cells was decreased proportionately. Far-field and downstream boundaries remained the same for all grids. The Navier-Stokes solver was run on each grid at a Mach number of 0.311 and an angle of attack of 3.03° until the residual error was reduced by at least four orders of magnitude. Convergence histories for the residual error in the continuity equation, the lift coefficient, and the drag coefficient for one of the grids used in the study are presented in figure A1. The results show that the lift and drag coefficients have converged to a steady value when the residual error has been reduced four orders of magnitude. For the grid-convergence study, the number of chordwise cells (N_c) was varied from 96 to 256, the number of spanwise cells (N_s) was varied from 32 to 48, and the number of normal cells (N_n) was varied from 32 to 64, as shown by the results in figure A2. The size of the final grid was determined to be the minimum number of cells that yielded differences in lift coefficient less

than 0.001 and differences in drag coefficient less than 0.0003 if the number of cells was increased.

The final grid had 192 chordwise cells, 40 spanwise cells, and 64 normal cells. Sketches of the final wing-surface grid and of the final volume grid are presented in figures A3 and A4, respectively. Note that some grid lines have been omitted for clarity. Eight spanwise cells were used to define the upper and lower halves of the rounded-tip cap. The chordwise spacing of the grid points was 0.002 of the local chord (c) at the leading edge and $0.006c$ at the trailing edge. The spanwise spacing of the grid points was 0.059η at the root and 0.003η at the inboard edge of the rounded tip. The normal spacing of the grid points increased from about $0.25 \times 10^{-6}c$ at the leading edge to $0.50 \times 10^{-6}c$ at the trailing edge. This spacing produced values of the normal spacing parameter y^+ that ranged from about 0.7 to 1.7 at the root and from about 0.3 to 1.0 at the tip.

Calibration of Navier-Stokes Solver

The Navier-Stokes code solves the equations on a single-block structured grid. The experimental setup utilizes a wing-body combination, and the presence of the body modifies the local flow field about the wing. The wing balance measures the forces and moments on the wing that include induced effects from the body. A comparison of experimental data from the wing-body combination with results from the Navier-Stokes solution for the wing alone would not be valid. To do so, the effects of the body on the wing flow field must be included in the calculations.

In effect, the body blocks the approaching flow and this leads to a local increase in the velocity in the plane of the wing. The body also acts as a low-aspect-ratio lifting surface that induces an upwash in the plane of the wing. Both effects are largest near the body and decrease rapidly with increasing distance from the body. The effects of the body on the local flow field were computed by using the panel method code, VSAERO, described in reference 19. The body alone with a fixed wake was represented by using 880 panels. The program provided three components of velocity at user-defined points in the flow field. Induced vertical and streamwise components of velocity along the quarter-chord line of the wing were used to predict the change in streamwise velocity (and Mach number) and angle of attack induced by the body at free-stream Mach numbers of 0.30, 0.50, and 0.70 and angles of attack of 0°, 1.0°, 2.0°, and 4.0°. A variation of the induced angle of attack (α_i) is strongly dependent on the body angle of attack and is only weakly dependent on the free-stream Mach number. The results at a Mach number of 0.30 are presented in figure A5(a). The results at the other two Mach numbers are similar. The correction factor for the normalized streamwise velocity (V_x/V_∞) (and Mach number), which was largest near the root and decreased toward the wingtip, was strongly dependent on the free-stream Mach number and only weakly dependent on the body angle of attack. The results at an angle of attack of 0° are presented in figure A5(b). The results at the other angles of attack are similar.

Induced upwash from the body (α_i) is equivalent to a twist across the wing. The upwash angle distribution was used to define the wing twist at five equally spaced stations across the wing: $\eta = 0$, 0.25, 0.50, 0.75, and 1.00. The root twist angle increased from 0° to 2.99° as the body angle of attack increased from 0° to 4.0°. (See ref. 9 for additional details.) This wing twist was incorporated into the wing-surface grid definition. A separate wing-surface grid was defined and used to create a different volume grid for each of the nominal angles of attack used in the numerical study (0°, 1.0°, 2.0°, and 4.0°).

Induced streamwise flow from the body was equivalent to a spanwise change in the free-stream Mach number. To simplify the calculations, an average change in the free-stream Mach number was used as an approximation. Because most of the change occurred near the wing root and the change was fairly constant on the outer portion of the wing, the use of an average approximation was reasonable. The free-stream Mach number for the Navier-Stokes calculations was increased by the change in the local Mach number at the 42-percent-semispan position because the spanwise center of lift was located there. The increase in the Mach number was 2.3 percent at a Mach number of 0.30 and was 3.1 percent at a Mach number of 0.72. The Navier-Stokes calculations were therefore performed on the grid having the appropriate wing twist for the desired angle of attack at the adjusted free-stream Mach number. Calculated pressure coefficients were corrected for the changes in free-stream static pressure and dynamic pressure due to the change in free-stream Mach number. Section lift and drag coefficients were rotated back into the untwisted wing axis system and corrected for the change in the free-stream dynamic pressure. Corrected section properties were integrated across the span to obtain the corrected wing lift and drag coefficients.

Comparisons of the experimental chordwise pressure distributions with those from the Navier-Stokes solver code with and without the corrections for the presence of the body are shown in figure A6 at a Mach number of 0.305 and an angle of attack of 4.03°. Without the correction, the calculated results do not agree with the experimental results, especially on the upper surface. With the correction, the agreement becomes much better,

especially the suction peak at the wing leading edge and the upper surface pressures. Correcting the calculated results at a Mach number of 0.719 brought about similar improvements in the agreement of the chordwise pressure distributions from the experiment. All calculated results, unless explicitly noted otherwise, include the corrections for the presence of the body.

Computed results having the corrections for the body are compared with experimental results at Mach numbers of 0.306 and 0.719 to determine the ability of the code to predict the aerodynamic characteristics without blowing. Comparisons of computed and experimental results for several spanwise stations at a Mach number of 0.306 and an angle of attack of 2.07° are presented in figure A7. In general, the agreement is very good, although some scatter occurs in the experimental results. The code generally underpredicts the upper surface suction at all spanwise stations and the peak leading-edge suction at the outboard stations. Even though the code adequately predicts the magnitude and location of the compression on the aft portion of the upper surface, it tends to overpredict the compression on the lower surface, the difference being largest at the inboard stations.

The effect of angle of attack on the comparison of experimental and computed chordwise pressure distributions at the 50-percent-spanwise location is presented in figure A8. Again, the computed results are in very good agreement with the experimental results. The leading-edge suction peak and the pressures on both surfaces back to the compression agree very well, and the agreement improves with increasing angle of attack. The experimental scatter is reduced at the higher angles of attack because the ratio of electrical signal to noise of the pressure transducer increases as the pressure level increases with angle of attack. The overshoot in the rapid-compression region on the lower surface appears for all three angles of attack. The computed results show virtually no trailing-edge separation at angles of attack up to 4.0°, which is consistent with experimental results.

Spanwise lift distributions for these three angles of attack ($\alpha \approx 0°$, 2.0°, and 4.0°) were computed from the chordwise pressure distributions, and the results are presented in figure A9. Agreement is good at the two lower angles of attack, but at the larger angle of attack, the agreement is only fair. A comparison of the computed and experimental lift and drag coefficients without blowing is presented in figure A10. In general, the lift-curve slopes are in very good agreement, but the computed lift is slightly less than the experimental value at a given angle of attack. The difference between the values of the computed and experimental lift coefficient ranges from 0.006 to 0.016. The experimental accuracy of the lift-coefficient measurement is 0.016. The uncertainty in the calculated lift-coefficient from the grid-convergence study is less than 0.001. Even though the computed drag is greater than the experimental drag, it follows the trend of the experiment well, with the difference between the computed and experimental drag coefficients ranging from 0.0004 to 0.0008. The experimental accuracy of the drag coefficient is about 0.0012, and the uncertainty in the calculated drag coefficient from the grid-convergence study is less than 0.0003. The differences in the lift and drag are less than the experimental accuracy. Thus, at a Mach number of 0.306, the Navier-Stokes solver with the corrections for the presence of the body adequately predicts the pressure distributions everywhere except on a small portion of the lower surface, and the solver reasonably predicts the total wing lift and drag.

Computed results with corrections for the presence of the body were also compared with experimental results at a Mach number of 0.721 at which supercritical flow occurs over the wing. Chordwise pressure distributions without blowing at $\alpha = 0.95°$ (the highest angle of attack tested) are compared at several spanwise stations in figure A11. At the inboard station, ($\eta = 0.25$), the code tends to overpredict the suction on the central portion of the airfoil (fig. A11(a)). Because the difference is not apparent at the other spanwise stations, a likely cause of the overprediction is interference from the body that is not included in the simple global Mach number correction. Because the tip region is most important in this study, this minor difference at the inboard station is acceptable. At all spanwise stations, the code predicts the upper surface compression region very well, and the lower surface is in very good agreement with only a slight overshoot at the end of the rapid compression. Because the code will be used to predict the changes due to blowing, small differences that do exist should have minimal impact on the incremental values.

The effect of angle of attack on the comparison of the chordwise pressure distributions at $M_\infty = 0.721$ is presented in figure A12 for the 50-percent-spanwise location. At the lower angle of attack, (–0.09°) only a small region of supersonic flow occurs on the upper surface. However, at an angle of attack of 0.95°, supersonic flow extends from about 10 to 60 percent chord. Computed results with the correction for the body are in very good agreement with the experimental results, although the computations slightly overpredict the suction on the upper surface. The code with the correction adequately predicts the location of the compression region on both surfaces and the magnitude of the pressure rise. The results on the lower surface are in excellent agreement. Also, the code with the correction adequately predicts the results for conditions that result in regions with supercritical flow.

Computed and experimental spanwise lift distributions for angles of attack of –0.09° and 0.95° are compared in figure A13. As noted previously, the code overpredicts the suction on the upper surface at $\eta = 0.25$, which leads to an overprediction of the section lift coefficient at that location. The agreement from $\eta = 0.70$ to $\eta = 0.90$ is very good. Because blowing from the wingtip is not expected to have a measurable effect on the inboard portion of the wing, the differences between the calculations and the experiment are acceptable for this study.

A comparison of the wing lift and drag coefficients without blowing is presented in figure A14, and the calculations match the experimental results reasonably well. The quoted balance accuracy at a nominal Mach number of 0.721 is 0.004 for the lift coefficient and 0.0003 for the drag coefficient. The computed lift differs from the measured lift by 0.005, and the computed drag differs from the measured drag by about 0.0005.

From these results without wingtip blowing, the Navier-Stokes solver with corrections for the induced effect of the body satisfactorily predicts the wing lift and drag, the spanwise lift distributions, and the chordwise pressure distributions. The solver can be used to predict the aerodynamic characteristics at Mach numbers up to 0.72 at an angle of attack of about 1°.

Verification of Boundary Conditions Used To Simulate Blowing From Wingtip

Modifications to the Navier-Stokes solver to simulate spanwise blowing from the wingtip are verified by comparing calculated results with simulated blowing with experimental results at the same value of C_μ. Because the Navier-Stokes solver uses a finite-volume formulation of the equations, calculations are performed at the center of a cell defined by eight of the structured grid points. Boundary conditions on the wing surface are implemented by defining a "ghost cell" inside the wing surface that mirrors the cell with one face on the wing surface. The boundary condition at the surface for each computational variable is determined from the values of that parameter in the surface cell and in the ghost cell.

The most significant modification to the code involved changes in the boundary conditions used to simulate the jet flow. The jet is characterized by the three components of momentum, density, and pressure. The jet-exit static pressure is equal to the local static pressure for a fully expanded jet. To model the jet characteristics, the three components of momentum were specified at the jet exit (wing surface). The density and pressure of the jet were specified at the center of the ghost cell.

The boundary conditions for selected cells were modified to simulate spanwise blowing from the jets of tip 8. Boundaries of cells with blowing did not match the experimental jet boundaries exactly because of the technique used to define the surface grid. The rounded wingtip was formed by spacing grid points at equal angular increments. Such spacing led to cells with changing heights so that the cell boundaries were not aligned with lines of constant height. Cells with boundary conditions modified for blowing were selected by overlaying the outlines of the front and rear jet exits on the sketch of the rounded tip, as shown in figure A15. The cells with more than half the face area within the jet exit, which are identified by the shading, had the boundary conditions modified for jet blowing.

The grid in the vicinity of the wingtip must be fine enough to capture the rapidly changing flow field near the path of the jet exhaust. By using the final grid from the grid-convergence study as a baseline, the number of cells around each half of the wingtip cap (N_t) was increased to determine its effect on the wing aerodynamic characteristics. The results without and with blowing from the front jet are presented in figure A16. Without blowing, increasing the number of cells around the wingtip above the baseline value ($N_t = 8$) had a negligible effect on the wing lift and drag coefficients. With blowing from the front jet, increasing the number of cells from 12 to 16 around each half of the wingtip increased the wing lift coefficient by 0.001 and had a negligible effect on the wing drag coefficient. The tolerance level used to select the final grid for the wing grid-convergence study was a change in the wing lift coefficient less than 0.001 and a change in the wing drag coefficient less than 0.0003. The results from the grid with 16 cells around each half of the wingtip satisfied these criteria. The grid used to study the effects of blowing had 16 cells around each half of the wingtip, for a total of 48 spanwise cells.

Four cells were typically used over the height of the jet exit (see fig. A15), which allowed three levels of multigrid to be used in the calculations. The jet area for the computations was larger than the jet area used for the experiments. The ratio of the front jet-exit area to the wing area was 2.8×10^{-4} for the experiment and 3.8×10^{-4} for the computations. For the rear jet, the ratios were 6.7×10^{-4} for the experiment and 8.9×10^{-4} for the computations. Modifications to the boundary conditions to simulate blowing were verified by comparing experimental results with calculated results at the same value of C_μ. The comparisons included the change in the chordwise pressure distribution, the section lift coefficient, and the wing lift and drag coefficients.

The Navier-Stokes solver was used to compute the flow field without tip blowing ($C_\mu = 0$) and with blowing from one jet ($C_\mu = 0.0066$) at a Mach number of 0.307 and an angle of attack of 2.07°. The change in the chordwise pressure distributions ($\Delta C_p = C_p$ (with blowing) – C_p (without blowing)) at $\eta = 0.90$ with blowing from the front and from the rear jet is presented in figure A17. Blowing has only a small effect on the pressure coefficients. For the front jet, the calculated and experimental results show similar trends with an increase in suction ($-\Delta C_p$) on the upper surface and an increase in pressure ($+\Delta C_p$) on the lower surface. However, the calculations overpredict the suction on the upper surface, and they also predict an increased leading-edge suction peak that was not seen in the experimental results. The orifice spacing near the leading edge may have been too large to resolve this effect. The comparisons are similar for the rear jet. Both the calculated and experimental results show an increase in suction on the upper surface, especially along the rear half of the chord. Both results show an increase in pressure on the lower surface. The calculations again overpredict the change in the pressure distribution and predict a small increase in the leading-edge suction peak. The calculated region with the largest increase in suction on the upper surface is closer to the trailing edge for the rear jet. These small differences over the front and rear portions of the chord lead to errors in the prediction of the pressure component of the drag.

Changes in the chordwise pressure distributions will be reflected in the spanwise lift distributions. Blowing has been shown to increase the loading near the wingtip (e.g., see refs. 2–4), but the effect becomes smaller as the distance from the tip increases. A comparison of the calculated and experimental spanwise variations of the section lift coefficient with and without blowing is presented in figure A18. For either jet location, both the calculated and experimental results show an increase in the lift near the wingtip that decreases with increasing distance from the wingtip. The calculations indicated that the measurable influence of the jet blowing extends farther inboard than was found in the experiment. However, the measured and calculated results are still in reasonable agreement. The changes in the chordwise pressure distributions and in the spanwise variation of the section lift coefficient indicate that the calculations are in agreement with the experiments at the one value of C_μ presented. Comparisons of calculated and experimental results over a range of C_μ are needed to gain the necessary confidence in the modified Navier-Stokes solver to predict the effect of blowing at conditions outside the experimental test envelope.

A comparison of the change in the computed and experimental section lift coefficients at the 90-percent-semispan location with jet momentum coefficient is presented in figure A19. The section lift coefficient at that spanwise station increases with increasing jet momentum coefficient. For either jet, computations show the proper trend but the predicted increase in the section lift coefficient is too large. In general, the calculated results are better for the front jet than for the rear jet. Small differences noted in the change in the chordwise pressure distributions lead to these moderate differences in the section lift coefficients. Additional experimental data are needed closer to the wingtip to determine better how well the code predicts the effects of blowing on the surface pressure distribution.

Computed changes in the wing lift and drag coefficients are compared with the experimental results in figure A20. For the front jet, the calculations show the increase in the wing lift coefficient with increasing jet momentum coefficient. The experimental results indicated a small decrease in the wing drag coefficient with increasing jet momentum coefficient, but the calculations showed a very small increase. For the rear jet, changes in the computed and experimental lift coefficients are in good agreement. However, the computed drag increases with increasing jet momentum coefficient, which is opposite the effect found in the experiment. Although the drag trend for either jet location is the opposite of that found in the experiments, the differences are small, on the order of the accuracy of the drag computations. The increase in computed drag is due to the increase in suction on the aft part of the airfoil. Drag calculations are divided into viscous and pressure components. Although not shown, calculations indicate that the viscous drag is the same with or without blowing. Pressure drag increases with blowing, and because the surface has an aft-facing component, increased suction leads to increased drag.

Surface pressure coefficients, spanwise lift distributions, and the wing lift and drag coefficients predicted by the Navier-Stokes solver with corrections for the presence of the body are in good agreement with the experimental results at Mach numbers of 0.30 and 0.72 with no wingtip blowing. Also, the changes with blowing for the chordwise pressure distribution, section lift coefficient near the tip, and wing lift coefficient were predicted reasonably well by the modified Navier-Stokes solver with the body corrections. The modified solver can be used with reasonable confidence at a Mach number of 0.72 to predict the effects of blowing on the surface pressure distribution and wing lift. However, the calculation of the change in wing drag coefficient with blowing is questionable.

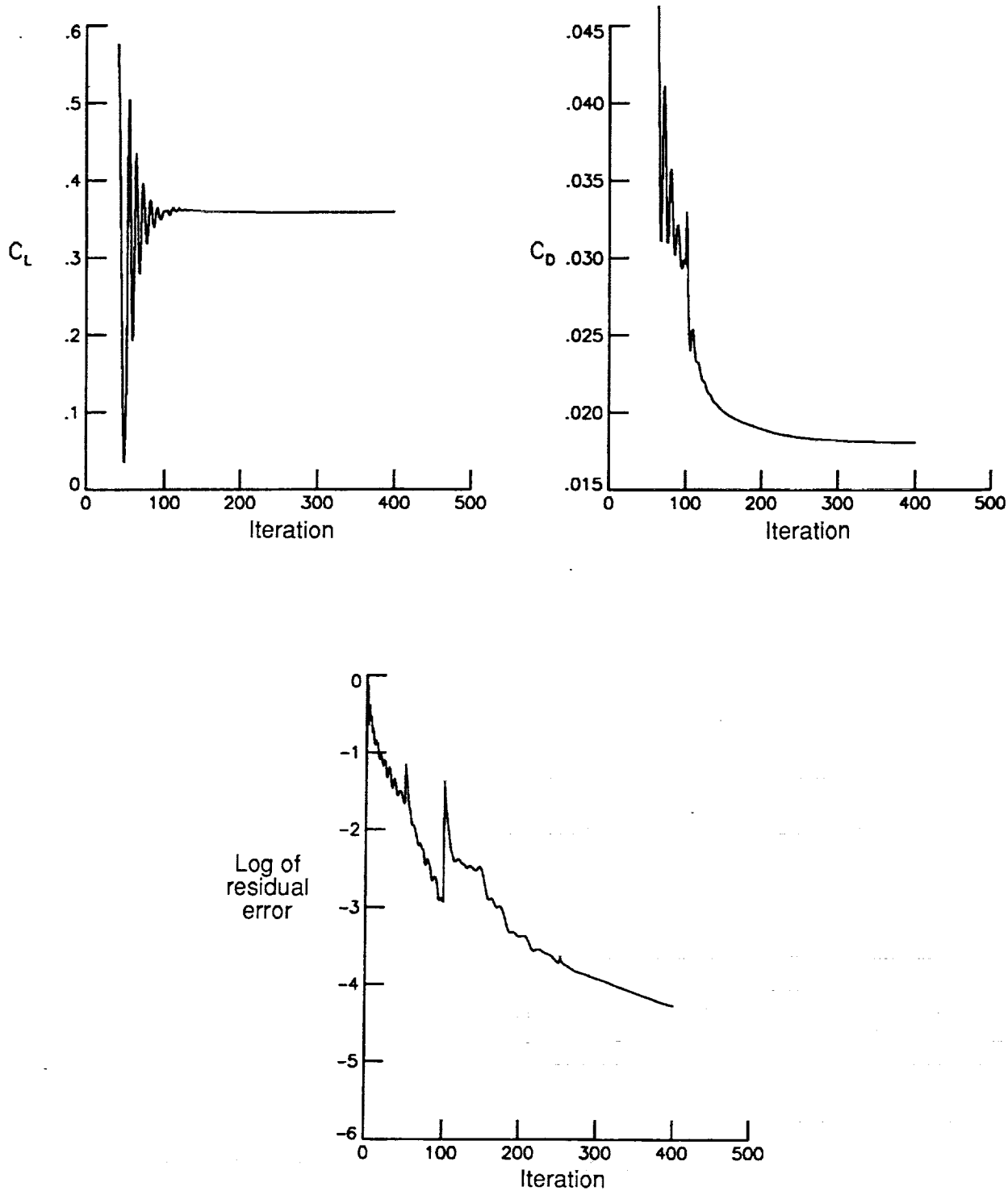

Figure A1. Convergence histories for residual error, lift coefficient, and drag coefficient for a typical grid ($N_c = 192$, $N_n = 64$, $N_s = 40$) at $M_\infty = 0.311$ and $\alpha = 3.03°$.

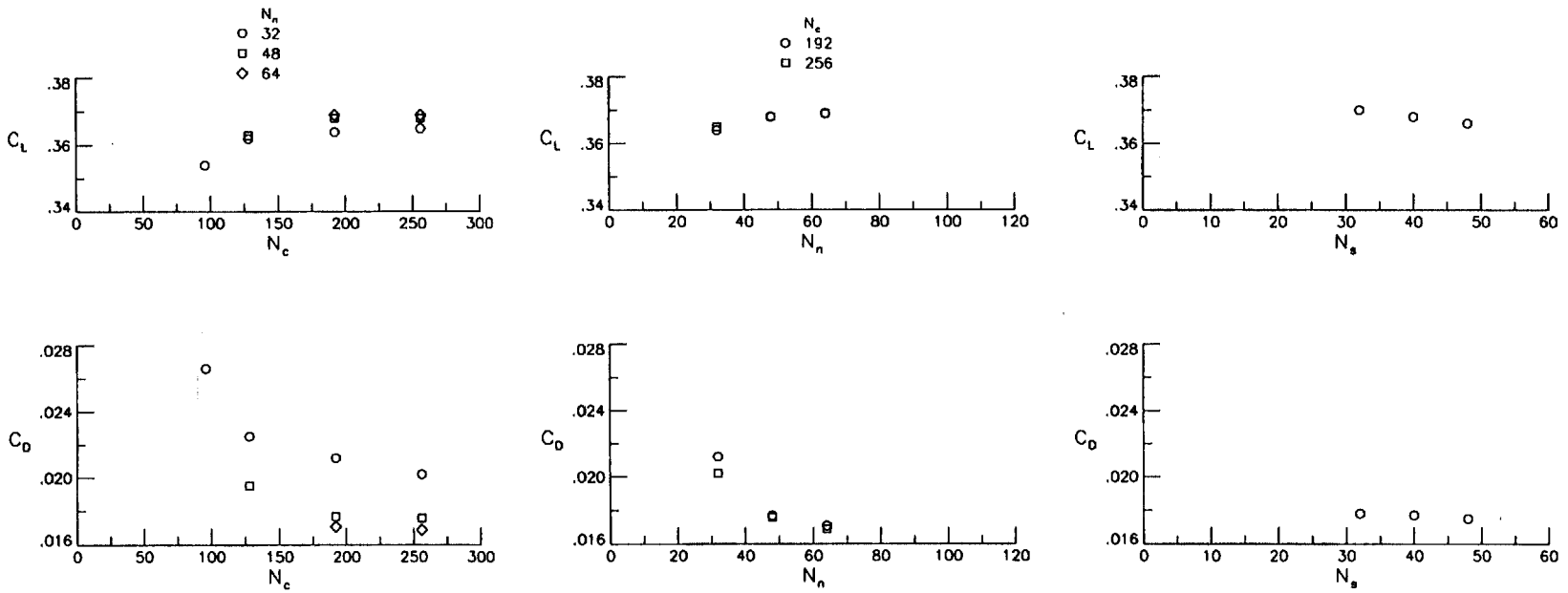

(a) Variation with number of chordwise grid points at $N_s = 32$.

(b) Variation with number of normal grid points at $N_s = 32$.

(c) Variation with number of spanwise grid points $N_c = 192$; $N_n = 256$.

Figure A2. Variation of lift and drag coefficients with number of grid points.

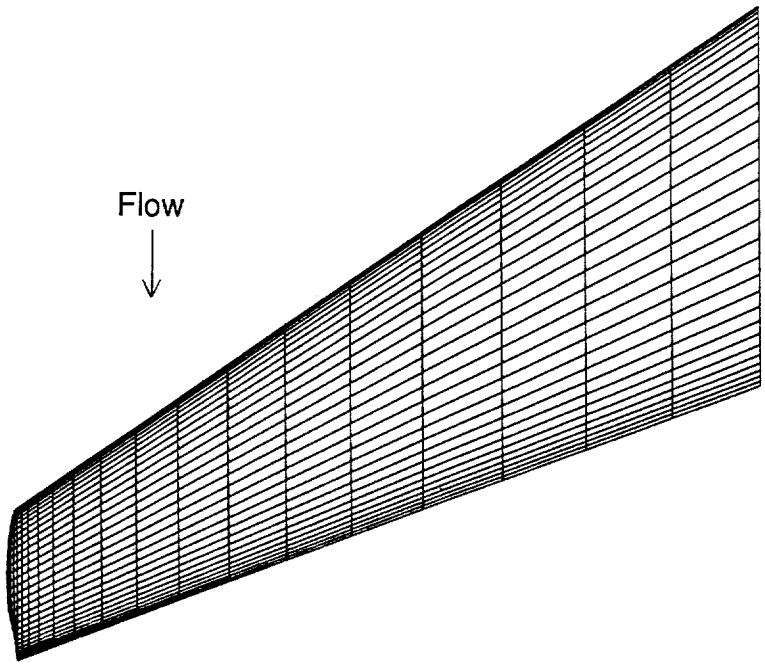

Figure A3. Sketch of final wing-surface grid. (Every other grid line was omitted for clarity.)

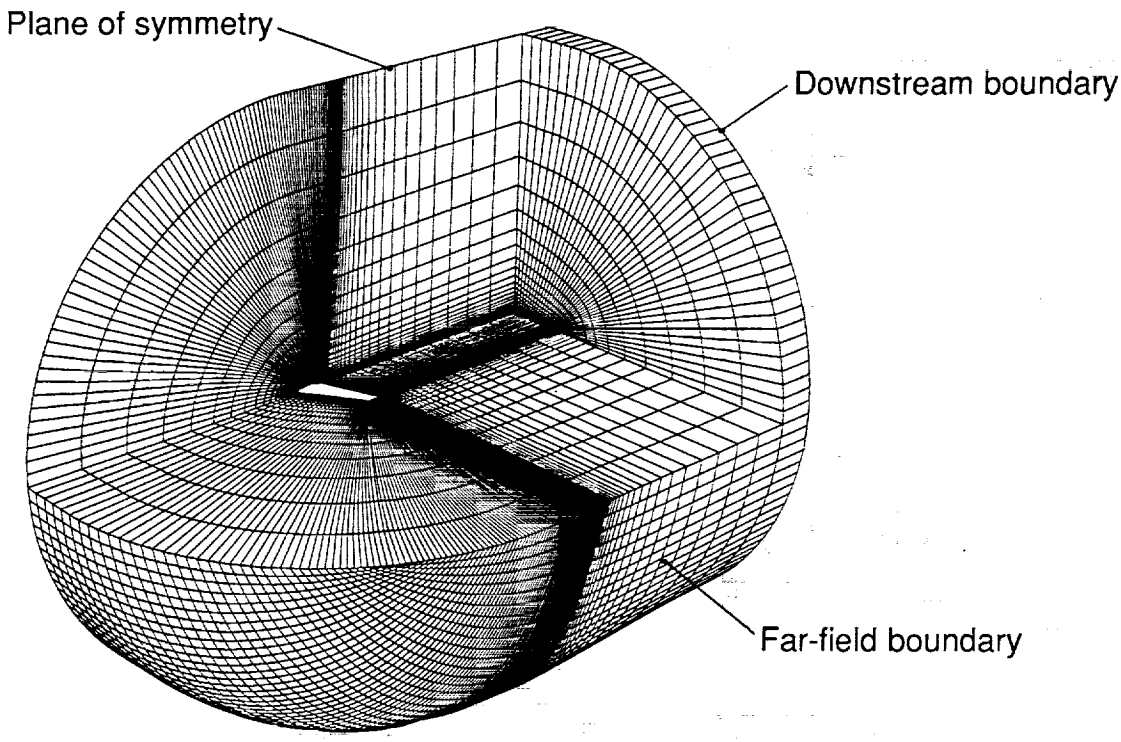

Figure A4. Sketch of final volume grid. (Some grid lines were omitted for clarity.)

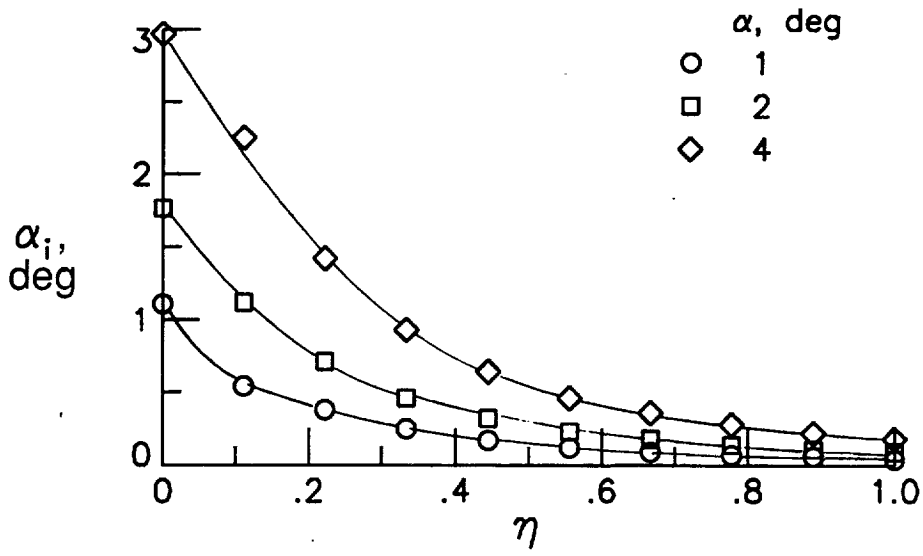

(a) Effect of body on local induced angle of attack at $M_\infty = 0.30$.

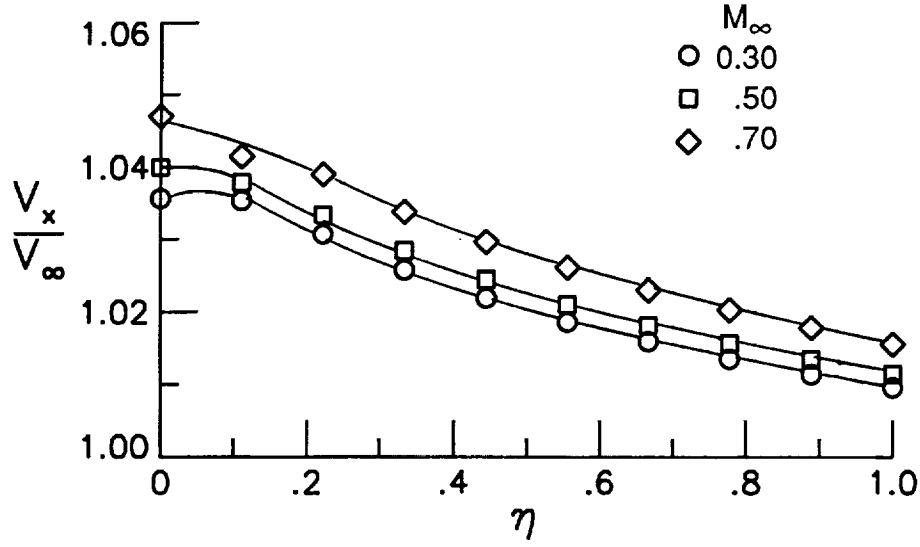

(b) Effect of body on local induced streamwise velocity at $\alpha = 0°$.

Figure A5. Calculated induced effect of body along wing quarter-chord line.

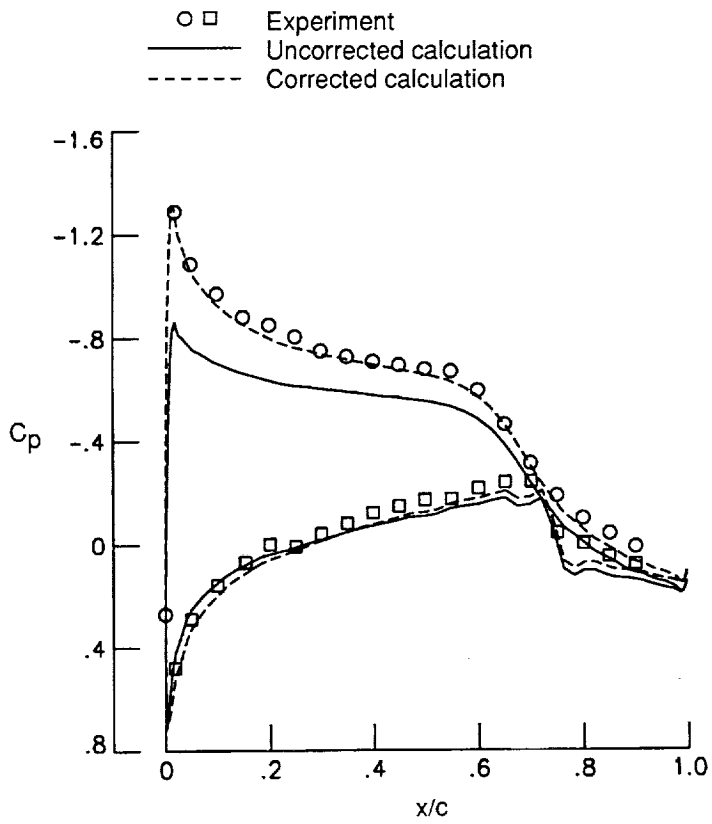

(a) $\eta = 0.25$.

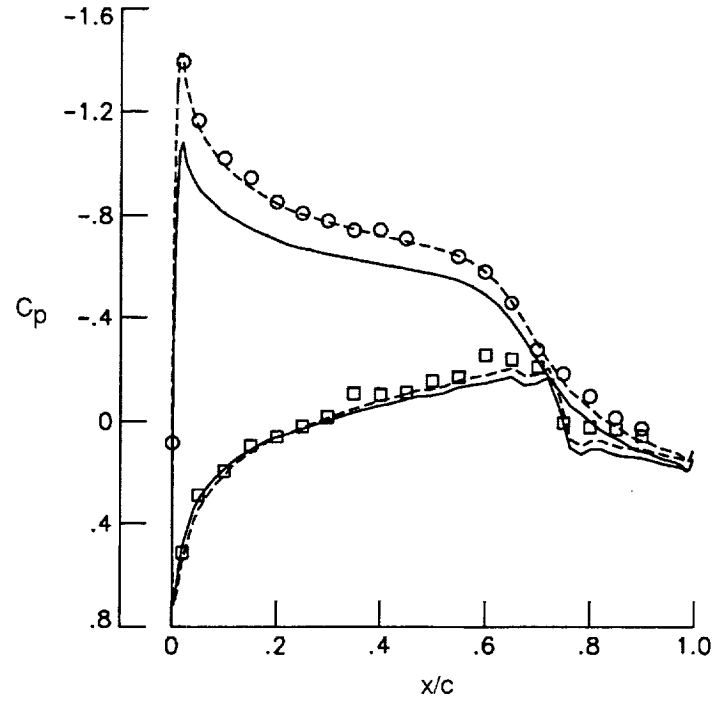

(b) $\eta = 0.50$.

Figure A6. Comparison of calculated (with and without corrections for presence of body) and experimental chordwise pressure distributions at $M_\infty = 0.305$ and $\alpha = 4.03°$.

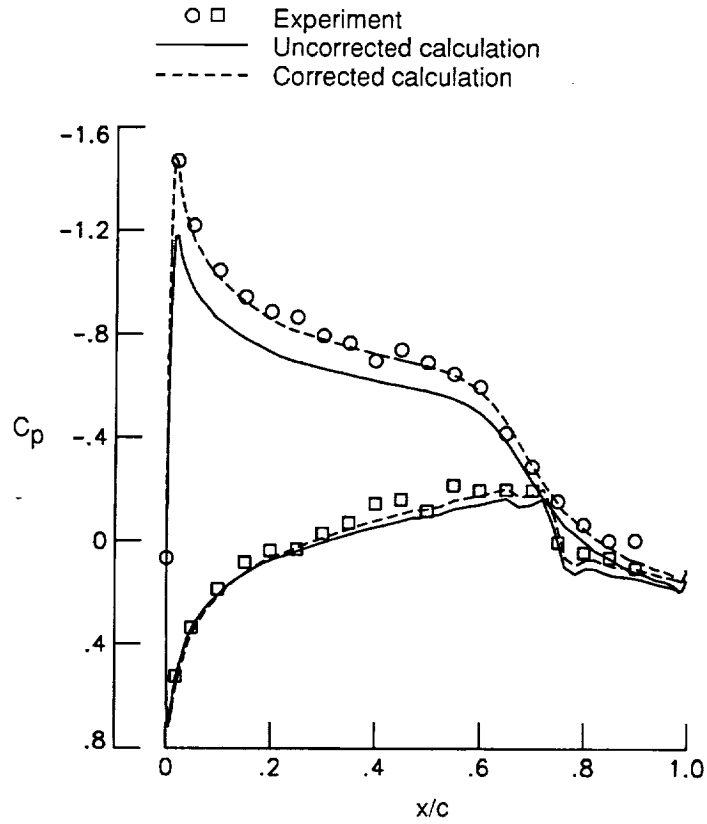

(c) $\eta = 0.70$.

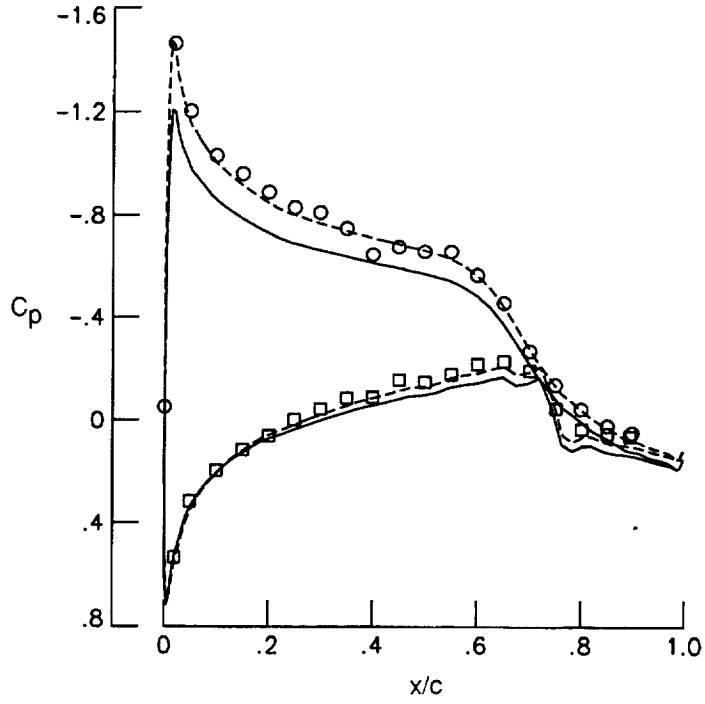

(d) $\eta = 0.80$.

Figure A6. Continued.

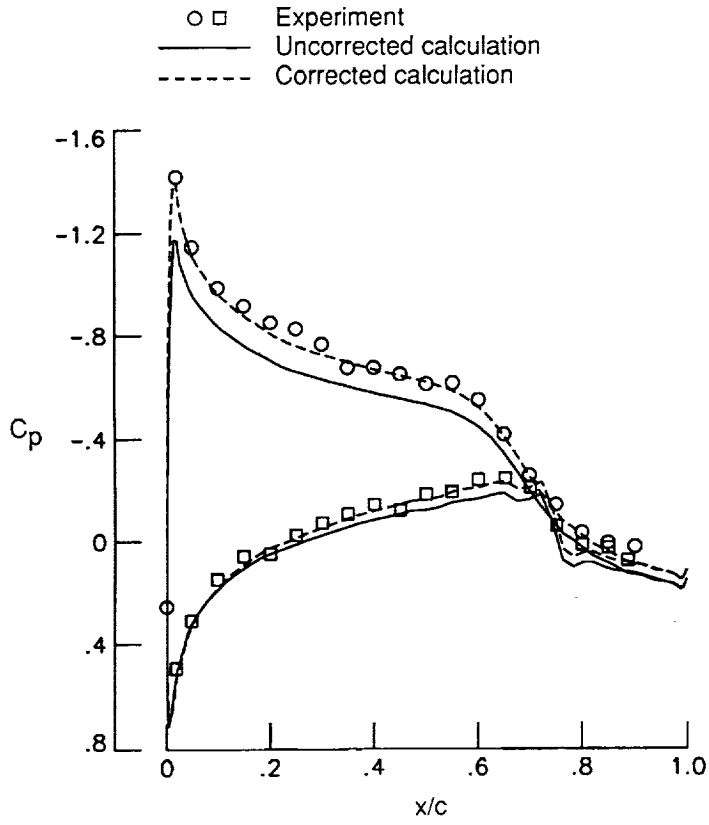

(e) $\eta = 0.90$.

Figure A6. Concluded.

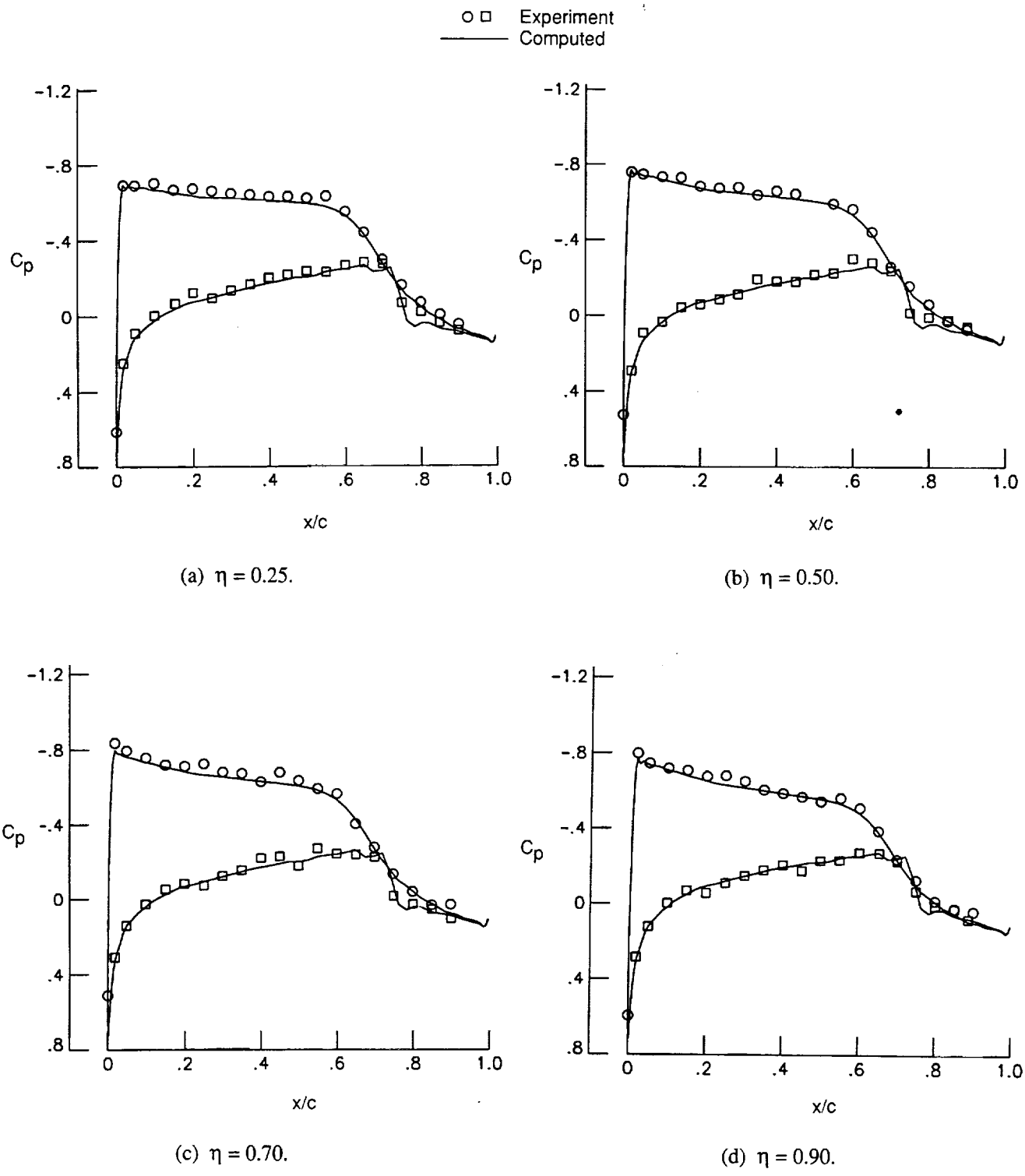

(a) $\eta = 0.25$.

(b) $\eta = 0.50$.

(c) $\eta = 0.70$.

(d) $\eta = 0.90$.

Figure A7. Comparison of computed and experimental chordwise pressure distributions without blowing at several spanwise stations at $M_\infty = 0.306$ and $\alpha = 2.07°$.

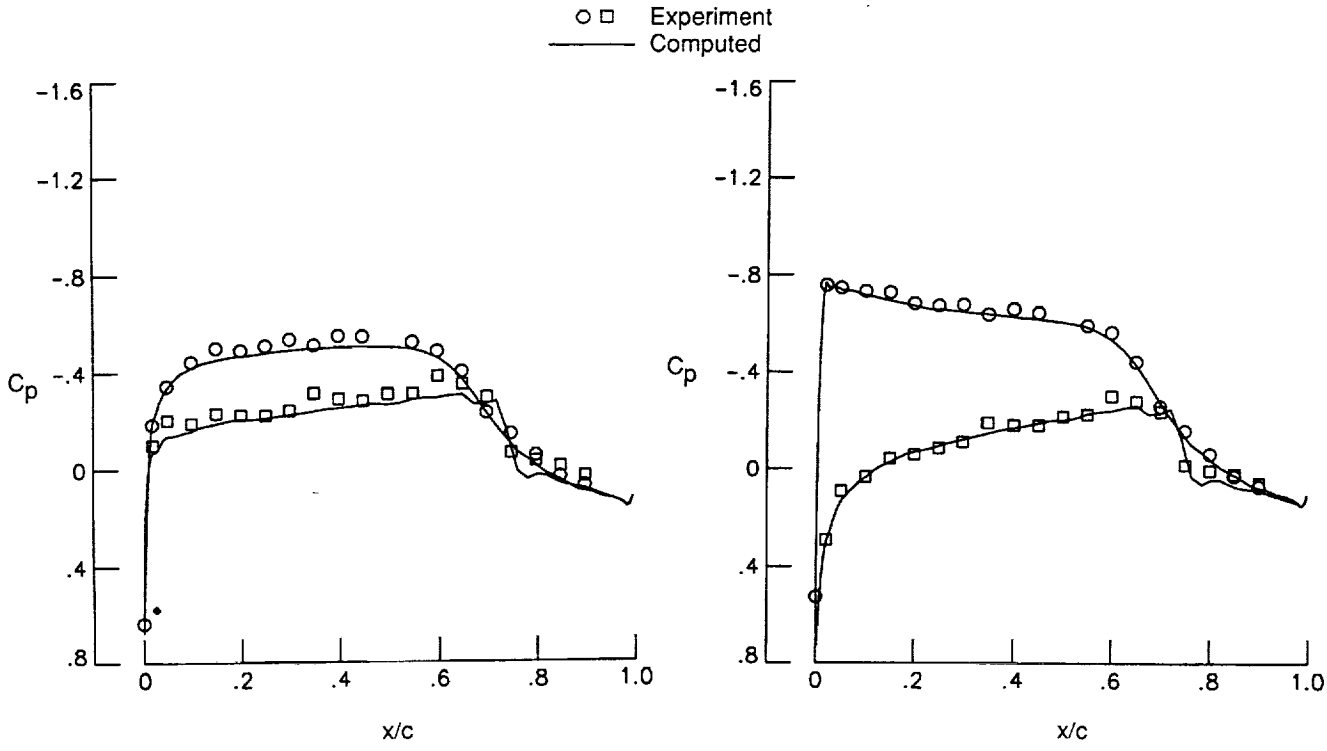

(a) $\alpha = -0.05°$.

(b) $\alpha = 2.07°$.

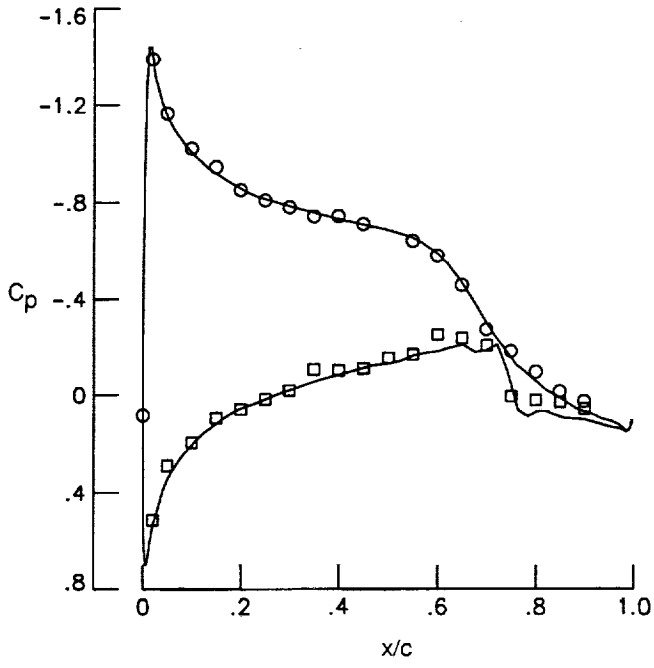

(c) $\alpha = 4.05°$.

Figure A8. Comparison of computed and experimental chordwise pressure distributions without blowing at several angles of attack at $\eta = 0.50$ and $M_\infty = 0.306$.

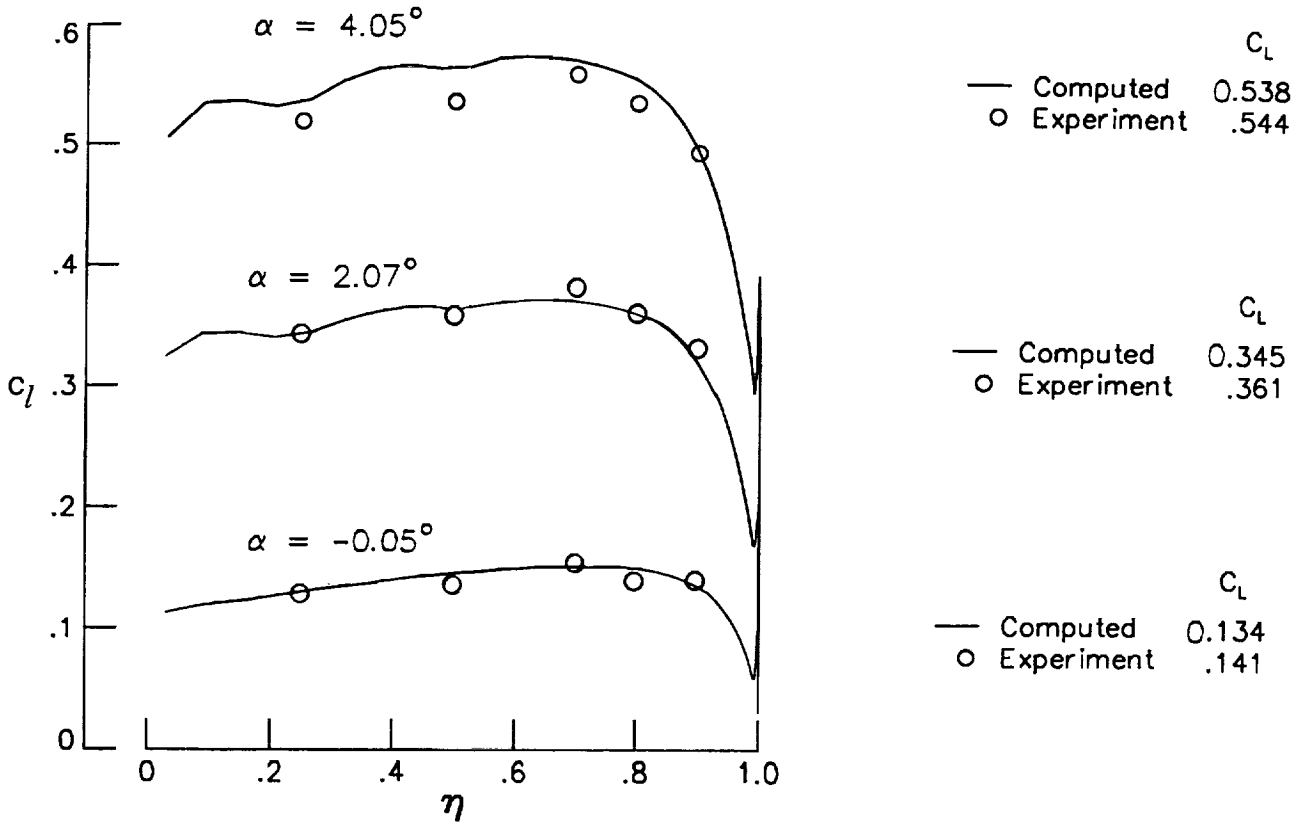

Figure A9. Comparison of computed and experimental spanwise lift distributions without blowing at several angles of attack at $M_\infty = 0.306$.

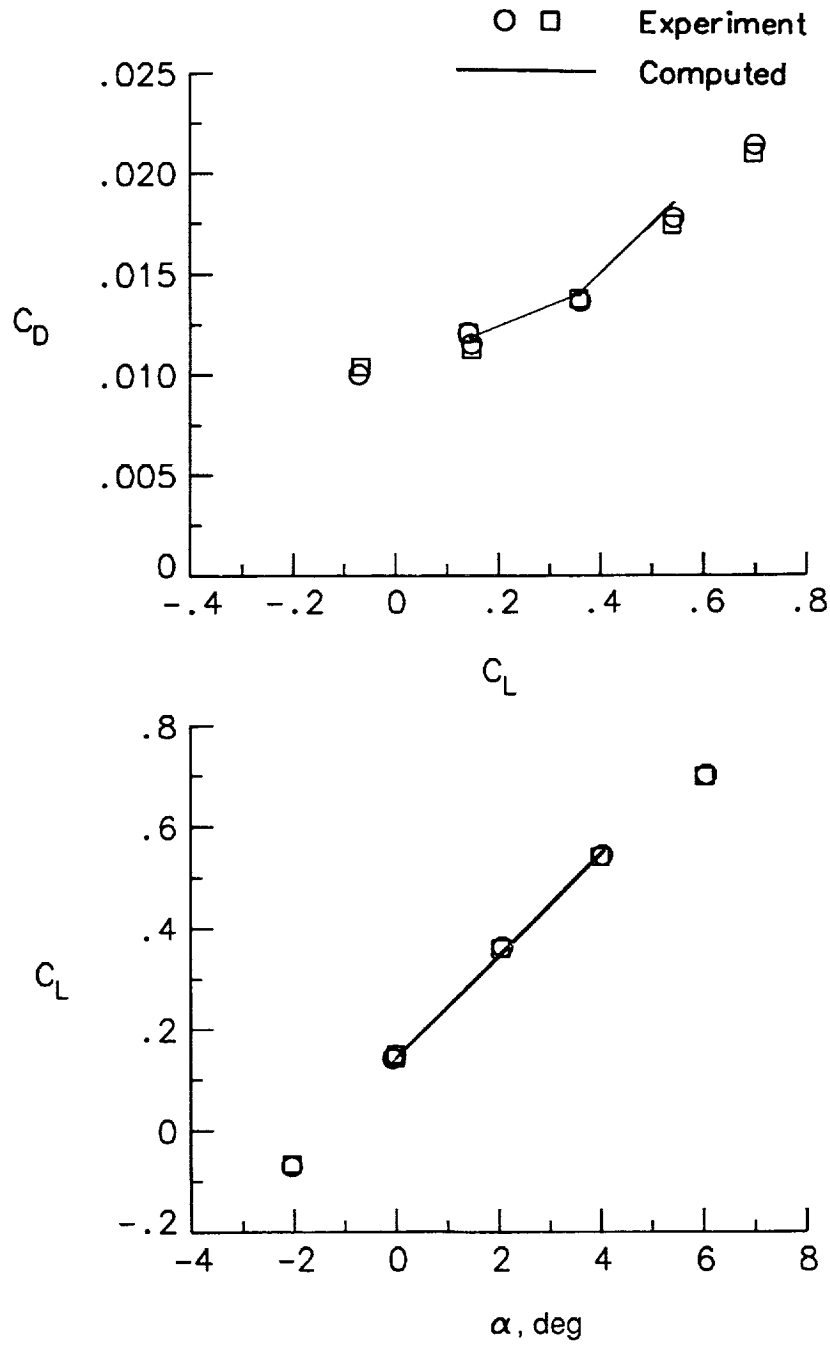

Figure A10. Comparison of computed and experimental wing lift and drag coefficients without blowing at $M_\infty = 0.306$.

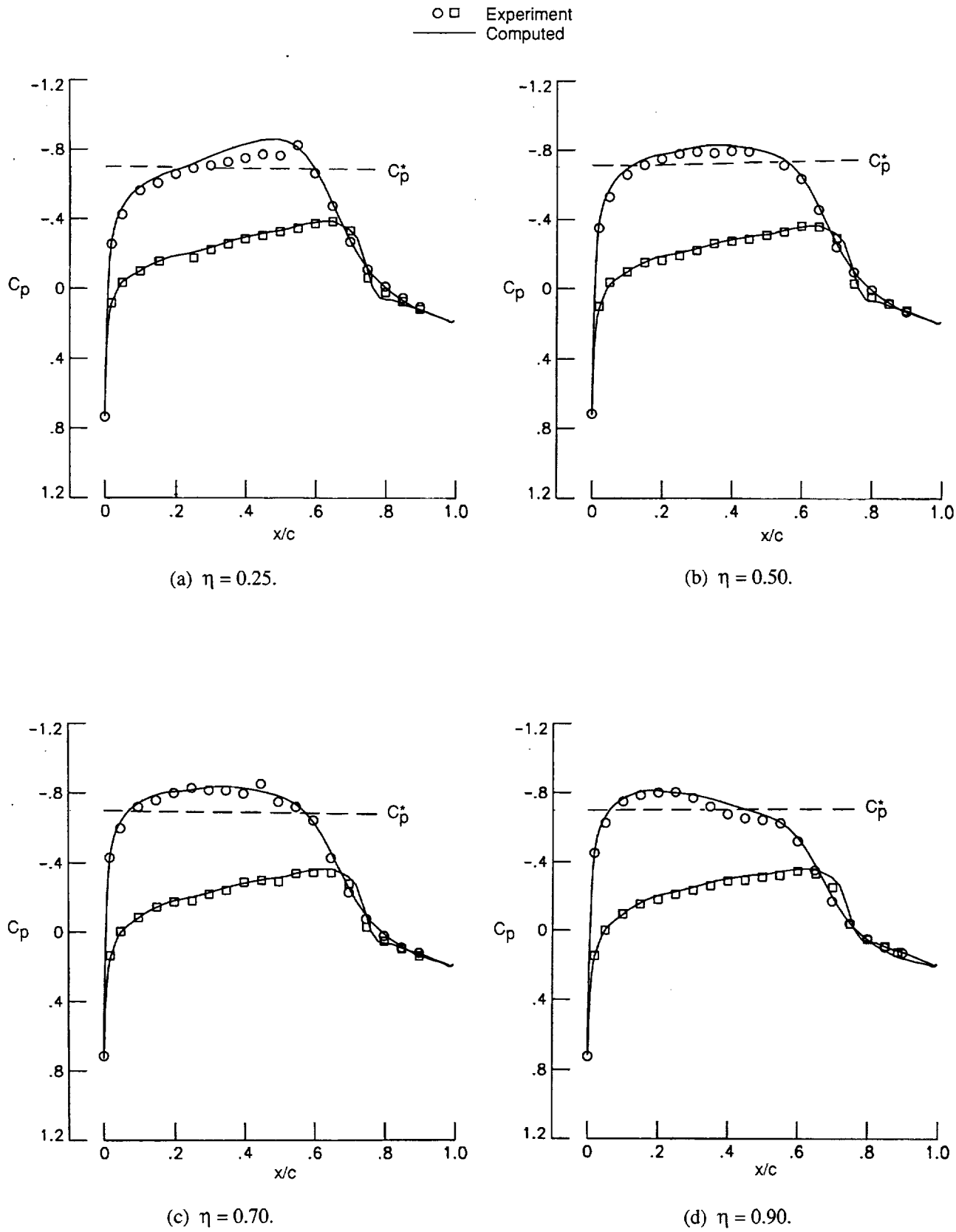

(a) $\eta = 0.25$.

(b) $\eta = 0.50$.

(c) $\eta = 0.70$.

(d) $\eta = 0.90$.

Figure A11. Comparison of computed and experimental chordwise pressure distributions without blowing at several spanwise stations at $M_\infty = 0.721$ and $\alpha = 0.95°$.

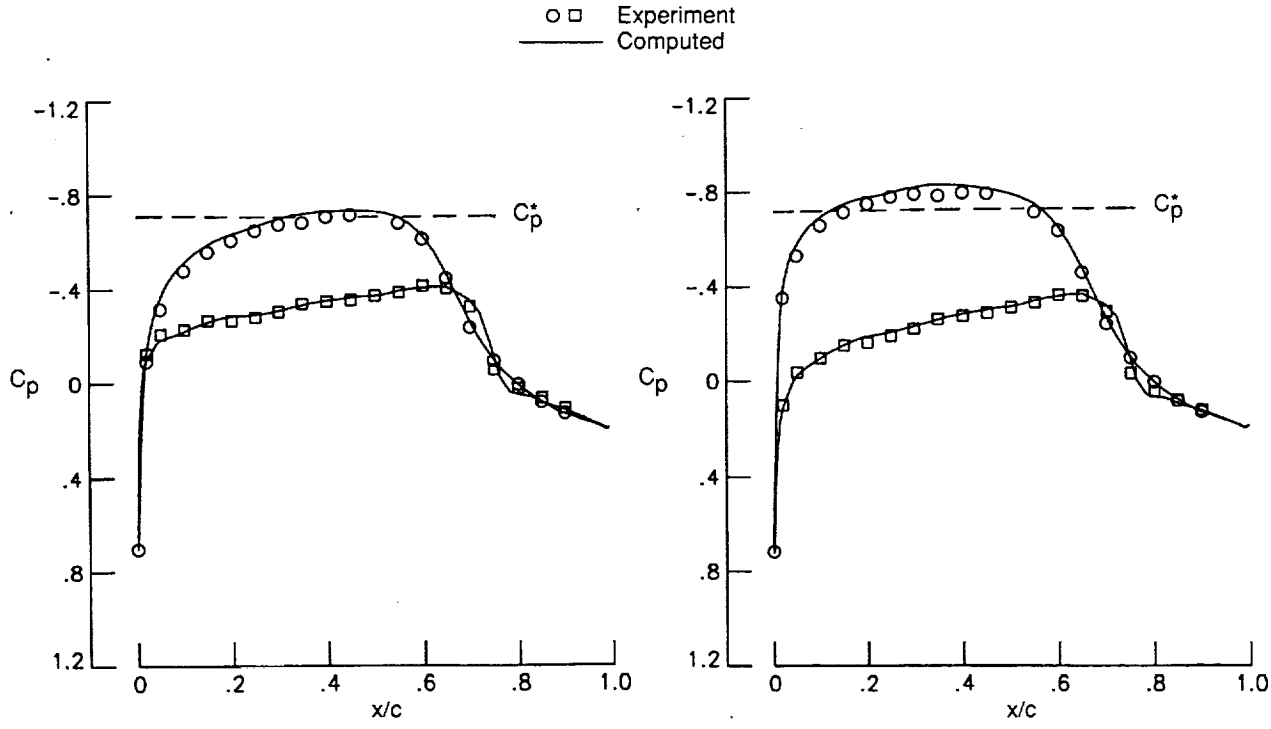

(a) $\alpha = -0.09°$.

(b) $\alpha = 0.95°$.

Figure A12. Comparison of computed and experimental chordwise pressure distributions at two angles of attack at $\eta = 0.50$ and $M_\infty = 0.721$.

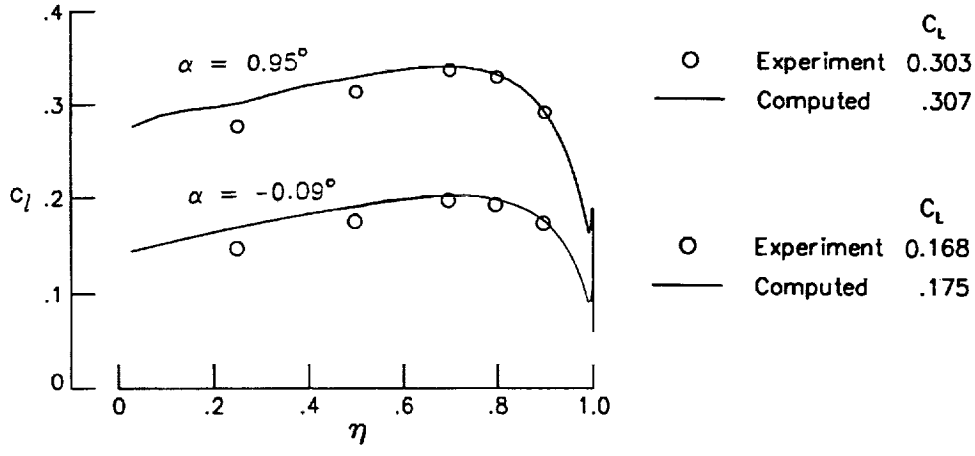

Figure A13. Comparison of computed and experimental spanwise lift distributions without blowing at two angles of attack at $M_\infty = 0.721$.

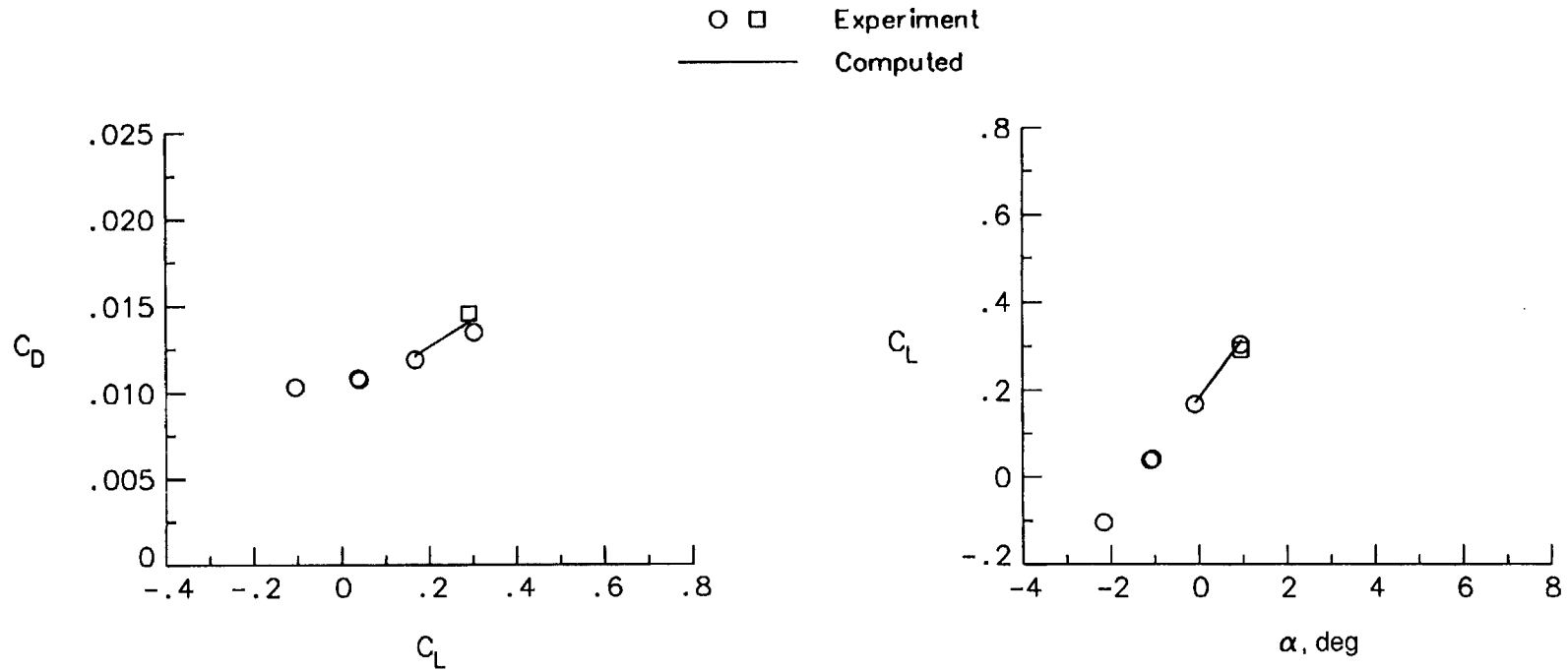

Figure A14. Comparison of computed and experimental wing lift and drag coefficients without blowing at $M_\infty = 0.721$.

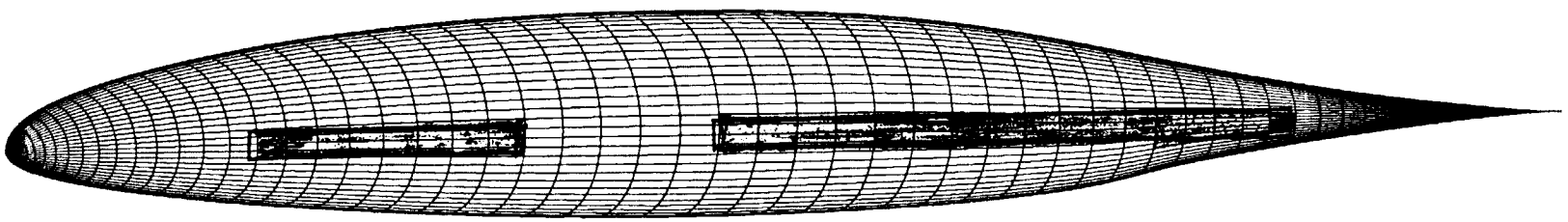

Figure A15. Sketch of wingtip surface grid with 32 cells in spanwise direction. Shaded portions denote cell surfaces with modified boundary conditions to simulate blowing.

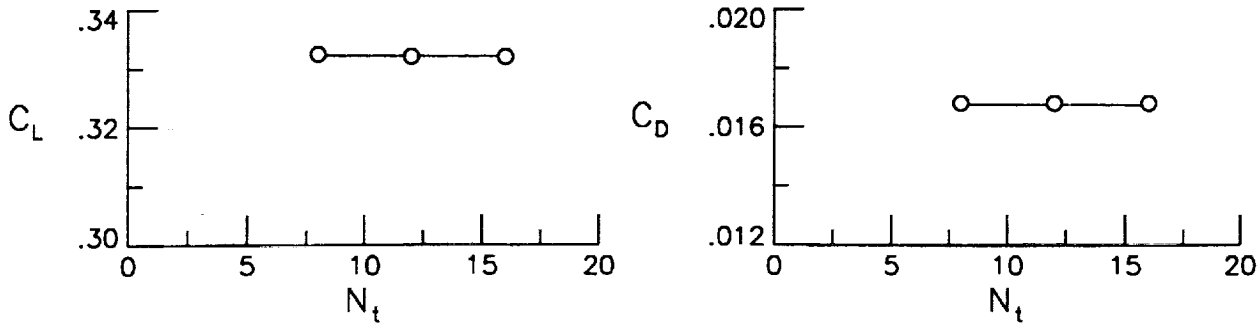

(a) No blowing.

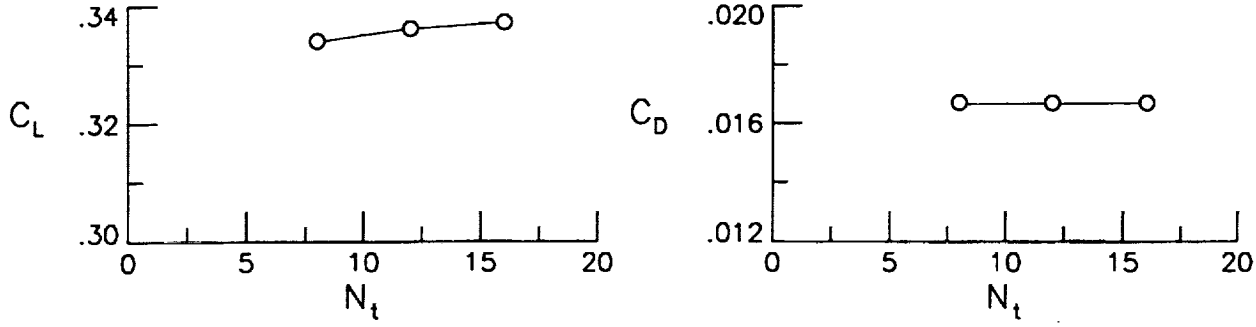

(b) Front jet; $C_\mu = 0.0066$.

Figure A16. Variation of wing lift and drag coefficients with number of grid points around each half of wingtip cap.

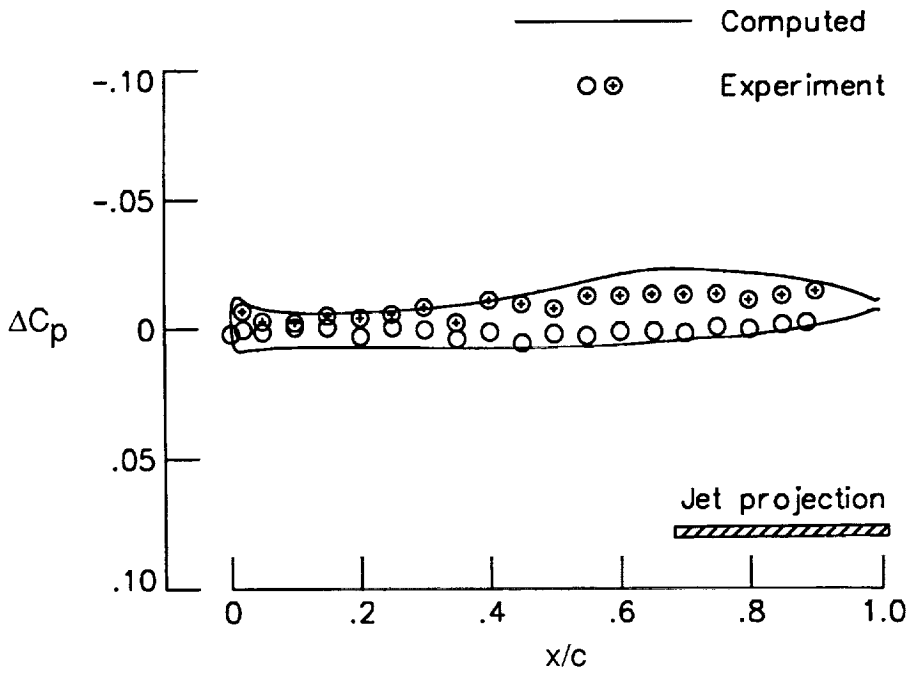

(a) Rear jet.

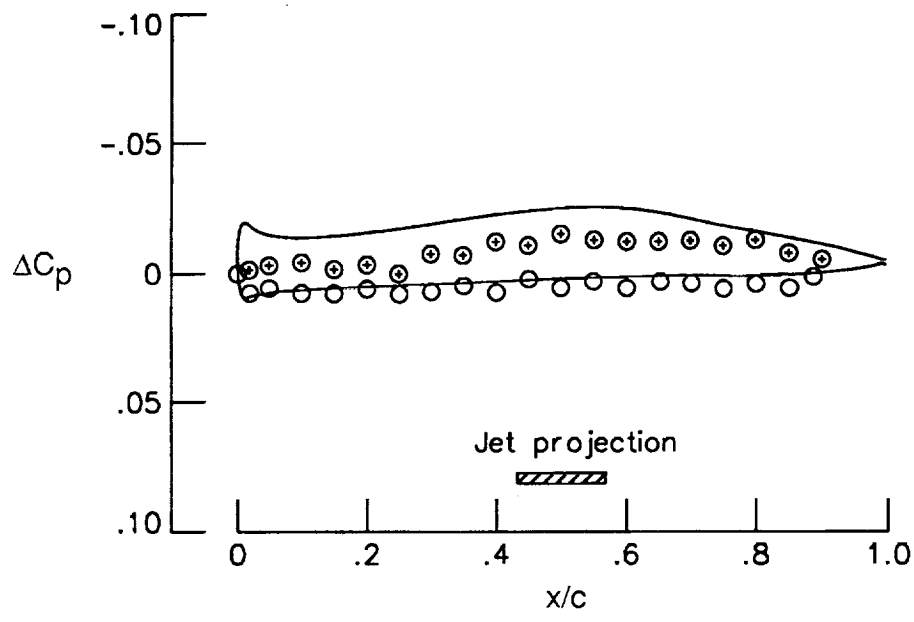

(b) Front jet.

Figure A17. Comparison of computed and experimental changes in chordwise pressure distribution at $\eta = 0.90$ due to blowing at $\alpha = 2.07°$, $M_\infty = 0.307$, and $C_\mu \approx 0.0065$. Upper surface measurements are denoted by a "+".

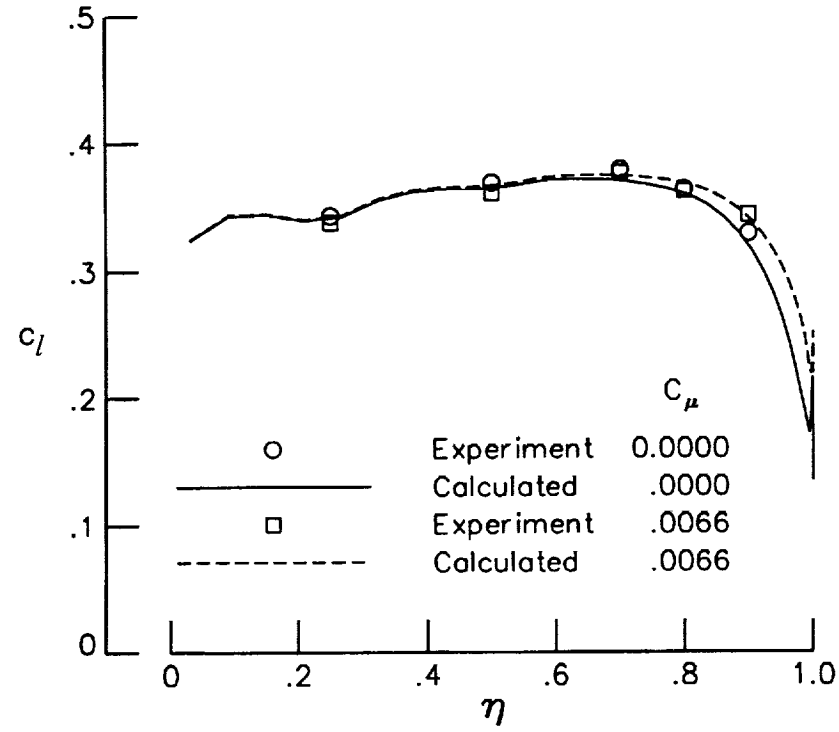

(a) Front jet.

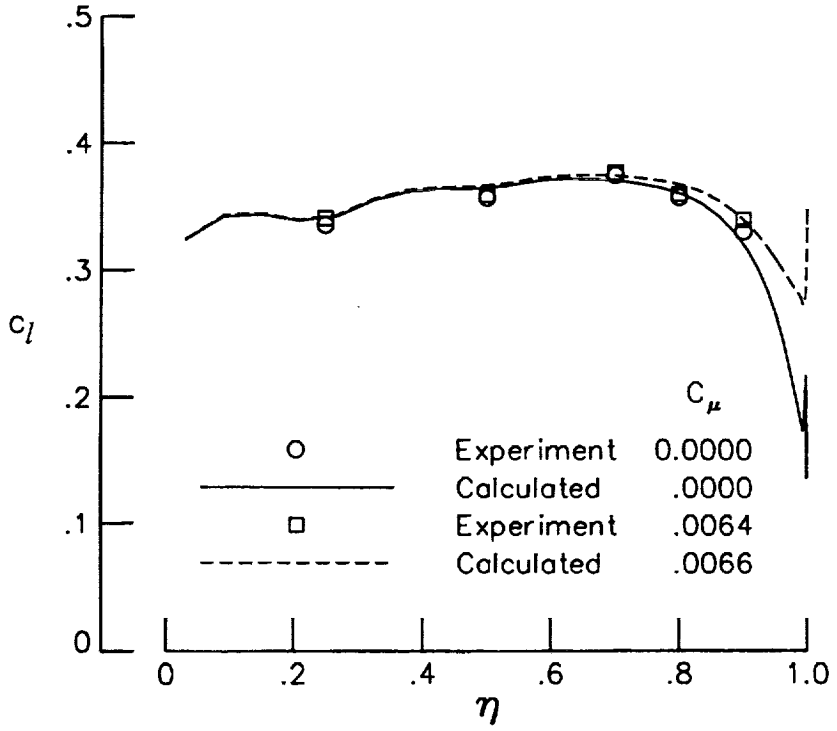

(b) Rear jet.

Figure A18. Comparison of calculated and measured spanwise distributions of section lift coefficient at $M_\infty = 0.315$ and $\alpha = 2.07°$.

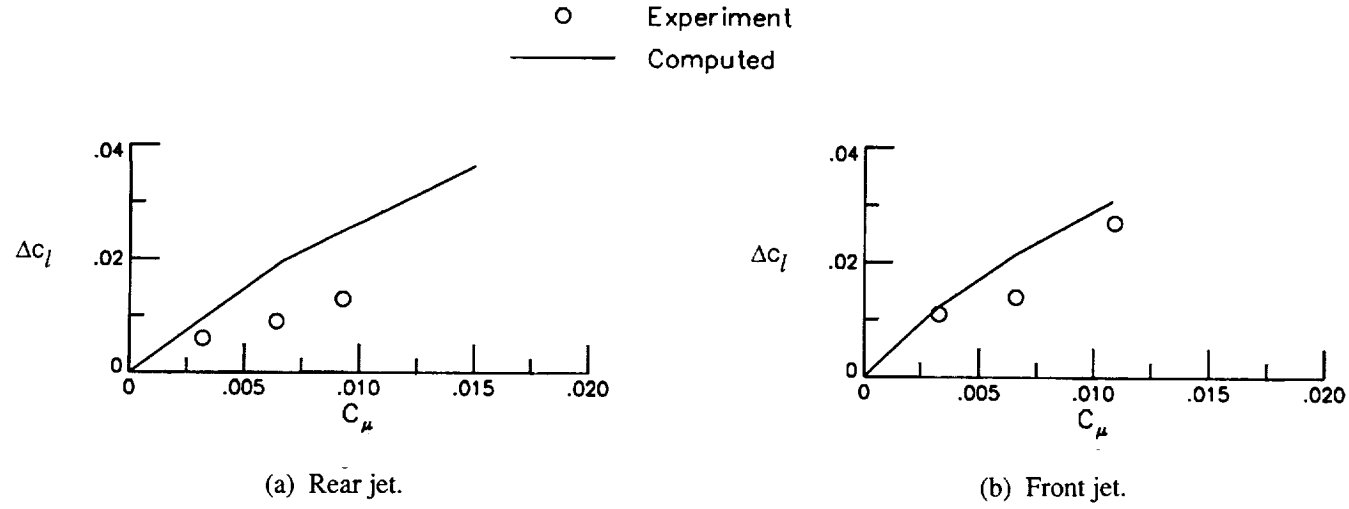

(a) Rear jet.

(b) Front jet.

Figure A19. Comparison of computed and experimental changes in section lift coefficients at $\eta = 0.90$ due to blowing at $M_\infty = 0.307$ and $\alpha = 2.07°$.

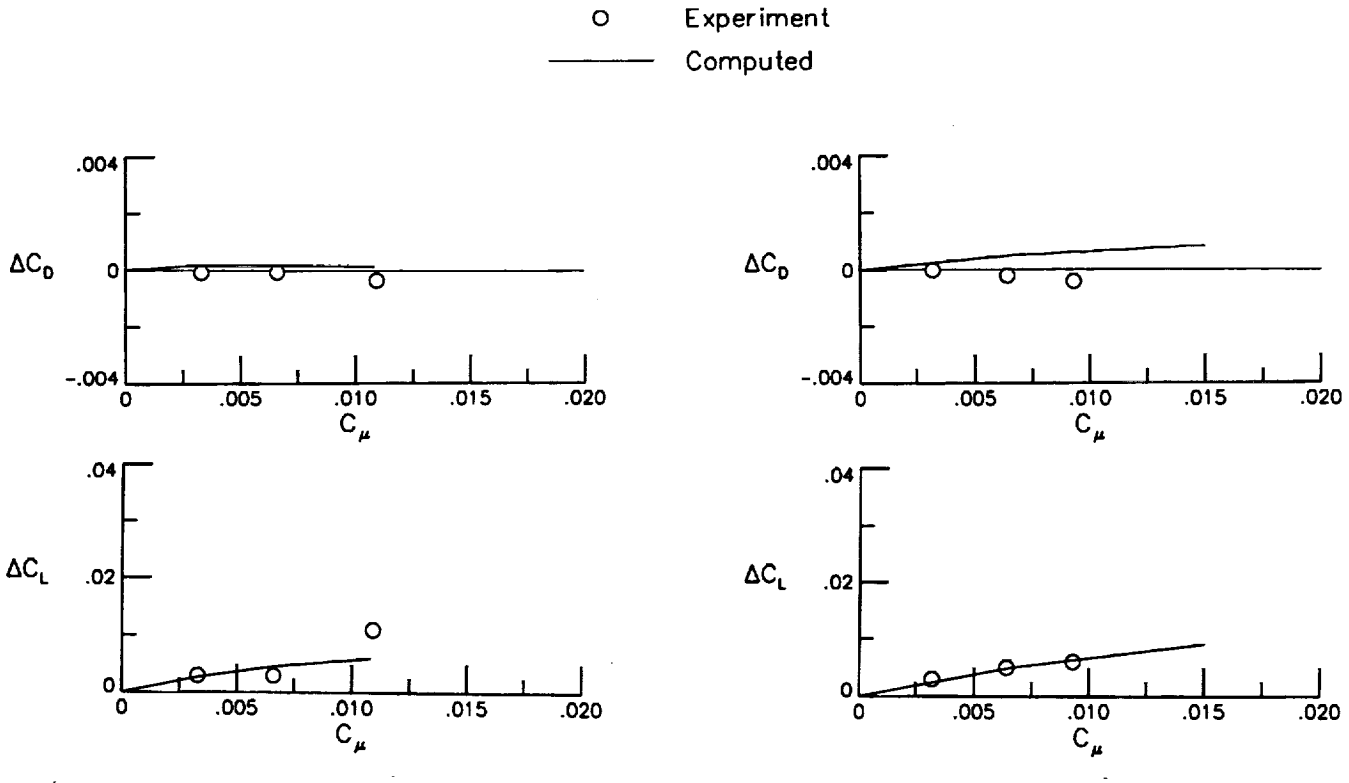

(a) Front jet.

(b) Rear jet.

Figure A20. Comparison of computed and experimental changes in wing lift and drag coefficients due to blowing at $M_\infty = 0.307$ and $\alpha = 1°$.

References

1. Zimmer, H.: *Aerodynamic Optimization of Wings at Subsonic Speeds and the Influence of Wingtip Design.* NASA TM-88534, 1983.

2. Tavella, D. A.; Wood, N. J.; Lee, C. S.; and Roberts, L.: *Two Blowing Concepts for Roll and Lateral Control of Aircraft.* NASA CR-180478, 1986.

3. Ayers, R. F.; and Wilde, M. R.: *Aerodynamic Characteristics of a Swept Wing With Spanwise Blowing.* College of Aeronautics, Cranfield, Note 57, Sept. 1956.

4. Smith, V. J.; and Simpson, G. J.: *A Preliminary Investigation of the Effect of a Thin High Velocity Tip Jet on a Low Aspect Ratio Wing.* Note ARL/A.163, Australia Dep. of Supply, June 1957.

5. Lloyd, Adrian: *The Effect of Spanwise Blowing on the Aerodynamic Characteristics of a Low Aspect Ratio Wing.* von Karman Institute for Fluid Dynamics Project Report 1963–90, 1963.

6. Wu, J. M.; Vakili, A.; and Chen, Z. L.: Wing-Tip Jets Aerodynamic Performance. *ICAS Proceedings, 1982—13th Congress of the International Council of the Aeronautical Sciences/AIAA Aircraft Systems and Technology Conference,* Volume 2, B. Laschka and R. Staufenbiel, eds., Aug. 1982, pp. 1115–1121. (Available as ICAS-82-5.6.3.)

7. Wu, J. M.; Vakili, A. D.; and Gilliam, F. T.: Aerodynamic Interactions of Wingtip Flow With Discrete Wingtip Jets. AIAA-84-2206, Aug. 1984.

8. Wu, J. M.; Vakili, A.; Chen, Z. L.; and Gilliam, F. T.: Investigation on the Effects of Discrete Wingtip Jets. AIAA-83-0546, Jan. 1983.

9. Mineck, Raymond Edward: *Assessment of Potential Aerodynamic Benefits From Spanwise Blowing at the Wing Tip.* NASA TM-107847, 1992.

10. Fox, Charles H., Jr.; and Huffman, Jarrett K.: *Calibration and Test Capabilities of the Langley 7- by 10-Foot High Speed Tunnel.* NASA TM X-74027, 1977.

11. Sewall, William G.; McGhee, Robert J.; Viken, Jeffery K.; Waggoner, Edgar G.; Walker, Betty S.; and Millard, Betty F.: *Wind Tunnel Results for a High-Speed, Natural Laminar-Flow Airfoil Designed for General Aviation Aircraft.* NASA TM-87602, 1985.

12. Braslow, Albert L.; and Knox, Eugene C.: *Simplified Method for Determination of Critical Height of Distributed Roughness Particles for Boundary-Layer Transition at Mach Numbers From 0 to 5.* NACA TN 4363, 1958.

13. Gillis, Clarence L.; Polhamus, Edward C.; and Gray, Joseph L., Jr.: *Charts for Determining Jet-Boundary Corrections for Complete Models in 7- by 10-Foot Closed Rectangular Wind Tunnels.* NACA WR L-123, 1945. (Formerly NACA ARR L5G31.)

14. Vatsa, V. N.: Accurate Numerical Solutions for Transonic Viscous Flow Over Finite Wings. *J. Aircr.,* vol. 24, no. 6, June 1987, pp. 377–385.

15. Vatsa, Veer N.; and Wedan, Bruce W.: Development of an Efficient Multigrid Code for 3-D Navier-Stokes Equations. AIAA-89-1791, June 1989.

16. Jameson, A.; Schmidt, Wolfgang; and Turkel, Eli: Numerical Solution of the Euler Equations by Finite Volume Methods Using Runge Kutta Time Stepping Schemes. AIAA-81-1259, June 1981.

17. Baldwin, Barrett; and Lomax, Harvard: Thin-Layer Approximation and Algebraic Model for Separated Turbulent Flows. AIAA-78-257, Jan. 1978.

18. Thomas, J. L.; and Salas, M. D.: Far-Field Boundary Conditions for Transonic Lifting Solutions to the Euler Equations. AIAA-85-0020, Jan. 1985.

19. Maskew, Brian: Prediction of Subsonic Aerodynamic Characteristics: A Case for Low-Order Panel Methods. *J. Aircr.,* vol. 19, no. 2, Feb. 1982, pp. 157–163.

Table 1. Coordinates of NASA HSNLF(1)-0213 Airfoil

	z/c			z/c	
x/c	Upper	Lower	x/c	Upper	Lower
0.00000	0.00000	0.00000	0.30000	0.07223	−0.05327
.00025	.00301	−.00160	.35000	.07375	−.05610
.00050	.00428	−.00230	.40000	.07400	−.05817
.00075	.00526	−.00286	.45000	.07301	−.05947
.00100	.00609	−.00335	.50000	.07069	−.05998
.00150	.00747	−.00419	.55000	.06678	−.05980
.00200	.00863	−.00492	.60000	.06078	−.05857
.00250	.00964	−.00556	.65000	.05219	−.05594
.00500	.01351	−.00796	.70000	.04132	−.05093
.01000	.01867	−.01120	.75000	.02954	−.04106
.02000	.02524	−.01551	.80000	.01829	−.03313
.04000	.03400	−.02155	.85000	.00810	−.02695
.06000	.04049	−.02602	.90000	−.00058	−.02188
.08000	.04573	−.02977	.95000	−.00761	−.01752
.10000	.05015	−.03308	.97500	−.01066	
.15000	.05878	−.03997	.98000		−.01555
.20000	.06498	−.04535	.99000	−.01224	−.01503
.25000	.06936	−.04971	1.00000	−.01322	−.01456

Table 2. Coordinates of Forward and Aft Portions of Body

Forward portion	
x station, in.	Height, in.
0.00	0.00
.05	.27
.10	.37
.15	.30
.20	.33
.25	.35
.30	.38
.35	.40
.40	.43
.45	.45
.50	.48
.60	.53
.70	.58
.80	.63
.90	.68
1.00	.73
1.50	.98
2.00	1.24
2.50	1.48
3.00	1.72
3.50	1.95
4.00	2.17
4.50	2.38
5.00	2.56
5.50	2.73
6.00	2.87
6.50	2.98
7.00	3.06
7.50	3.11
8.00	3.12

Aft portion	
x station, in.	Height, in.
40.50	3.12
41.00	3.12
41.50	3.09
42.00	3.04
42.50	2.98
43.00	2.89
43.50	2.79
44.00	2.68
44.50	2.55
45.00	2.40
45.50	2.25
46.00	2.08
46.50	1.90
47.00	1.71
47.50	1.51
48.00	1.30
48.50	1.09
49.00	.88
49.50	.65
49.60	.61
49.70	.56
49.80	.52
49.90	.47
50.00	.43
50.05	.41
50.10	.38
50.15	.36
50.20	.34
50.25	.32
50.30	.29
50.35	.27
50.40	.25
50.45	.27
50.50	.00

Table 3. Measured Nondimensional Orifice Locations (x/c)

[Values are nondimensionalized by local wing chord]

Values of x/c at pressure orifices of—									
η = 0.25		η = 0.50		η = 0.70		η = 0.80		η = 0.90	
Upper	Lower	Upper	Lower	Upper	Lower	Upper	Lower	Upper	Lower
0.000		0.000		0.000		0.000		0.000	
.019	0.019	.019	0.020	.018	0.019	.019	0.020	.018	0.019
.049	.050	.049	.050	.049	.049	.050	.050	.049	.049
.099	.100	.099	.100	.099	.099	.100	.101	.099	.099
.149	.153	.149	.150	.149	.150	.150	.151	.149	.149
.199	.200	.199	.200	.199	.199	.200	.201	.200	.200
.249	.250	.249	.250	.249	.250	.250	.250	.249	.250
.299	.300	.299	.299	.299	.299	.299	.300	.299	.300
.349	.350	.349	.349	.349	.349	.350	.350	.349	.350
.399	.399	.399	.400	.399	.400	.400	.400	.399	.400
.449	.449	.449	.450	.449	.450	.450	.451	.449	.450
.499	.499	.499	.500	.499	.499	.500	.501	.499	.499
.549	.550	.549	.550	.549	.549	.550	.551	.550	.549
.599	.600	.599	.600	.599	.599	.600	.601	.600	.600
.649	.650	.649	.650	.649	.650	.651	.651	.649	.652
.699	.700	.699	.700	.699	.700	.701	.701	.698	.700
.749	.750	.749	.750	.749	.750	.750	.751	.749	.750
.799	.800	.800	.800	.799	.800	.800	.801	.799	.800
.850	.849	.849	.850	.849	.850	.851	.851	.849	.850
.899	.899	.899	.900	.899	.900	.899	.895	.899	.886

Table 4. Summary of Jet Parameters for Each Wingtip

Tip							
Number	Position	x_j/c_{tip}	z_j/c_{tip}	c_j/c_{tip}	δ_j, deg	ψ_j, deg	Figure
1	Front	0.206	–0.008	0.062	0	0	8(a)
	Rear	.494	–.008	.062	0	0	8(a)
2	Front	0.299	–0.008	0.062	0	0	8(b)
	Rear	.604	–.008	.062	0	0	8(b)
3	Front	0.299	–0.008	0.062	20	0	8(c)
	Rear	.714	–.008	.062	0	0	8(c)
6	Front	0.299	0.023	0.062	0	0	8(d)
	Rear	.494	.023	.062	0	0	8(d)
8	Front	0.252	–0.008	0.155	0	0	8(e)
	Rear	.619	–.008	.375	0	0	8(e)
9	Front	0.299	–0.008	0.062	0	30	8(f)
	Rear	.604	–.008	.062	0	30	8(f)

Table 5. Wing Aerodynamic Characteristics for Each Wingtip Without Blowing

Tip	C_{L_α}, deg^{-1}	α_0, deg	$C_{D,0}$	$C_{B_{C_L}}$	$C_{B,0}$	$C_{m_{C_L}}$	$C_{m,0}$	Run
1	0.1010	–1.457	0.0104	0.4166	–0.0037	0.0050	–0.011	
2	.1016	–1.382	.0103	.4162	.0017	.0054	–.013	1
2	.1019	–1.389	.0099	.4168	–.0003	.0061	–.012	2
3	.1003	–1.411	.0102	.4151	–.0001	.0057	–.013	
6	.1006	–1.307	.0110	.4160	.0028	.0048	–.014	
8	.1008	–1.287	.0103	.4188	.0052	.0039	–.014	1
8	.1010	–1.419	.0112	.4171	–.0009	.0050	–.012	2
8	.1009	–1.423	.0112	.4174	–.0013	.0052	–.011	3
9	.1014	–1.344	.0098	.4134	.0003	.0072	–.013	
Average . . .	0.1011	–1.382	0.0104	0.4159	0.0004	0.0054	–0.013	

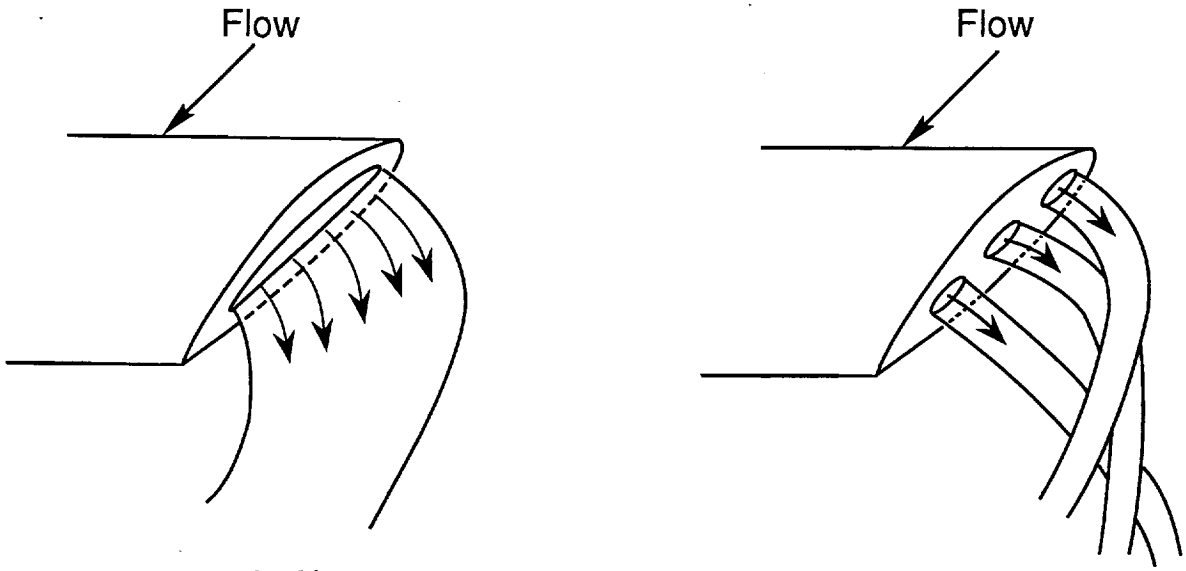

(a) Long-chord jet. (b) Short-chord jet.

Figure 1. Concepts of spanwise wingtip blowing.

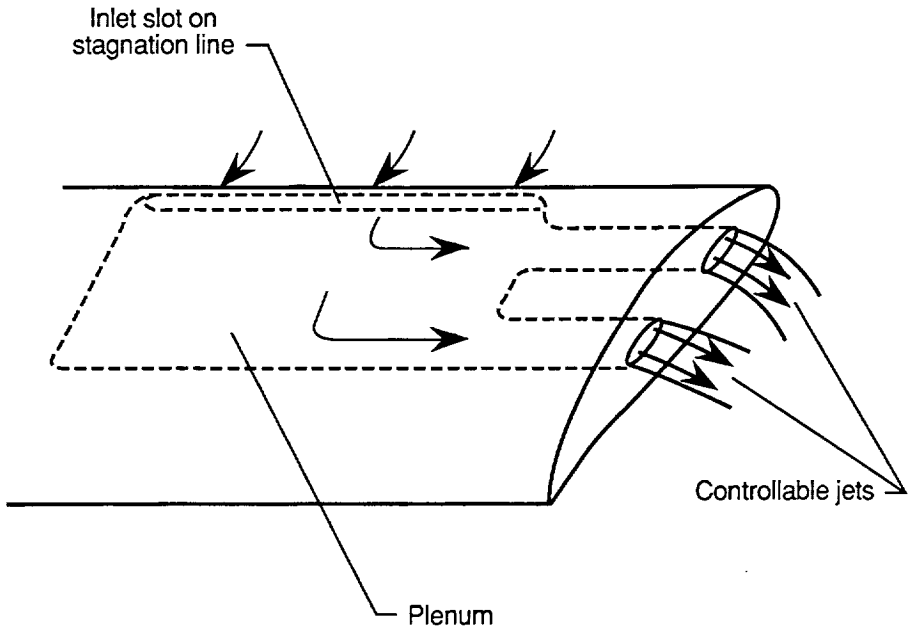

Figure 2. Passive wingtip blowing system.

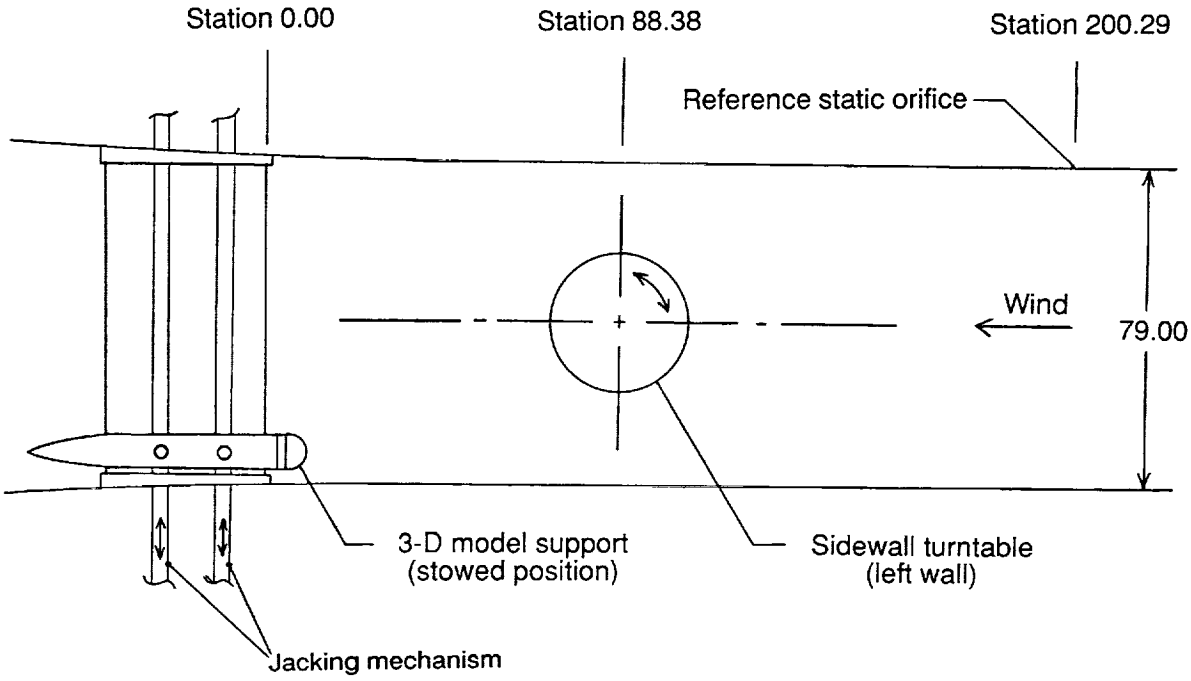

Figure 3. Sketch of test section of the Langley 7- by 10-Foot High-Speed Tunnel. All dimensions and stations are given in inches.

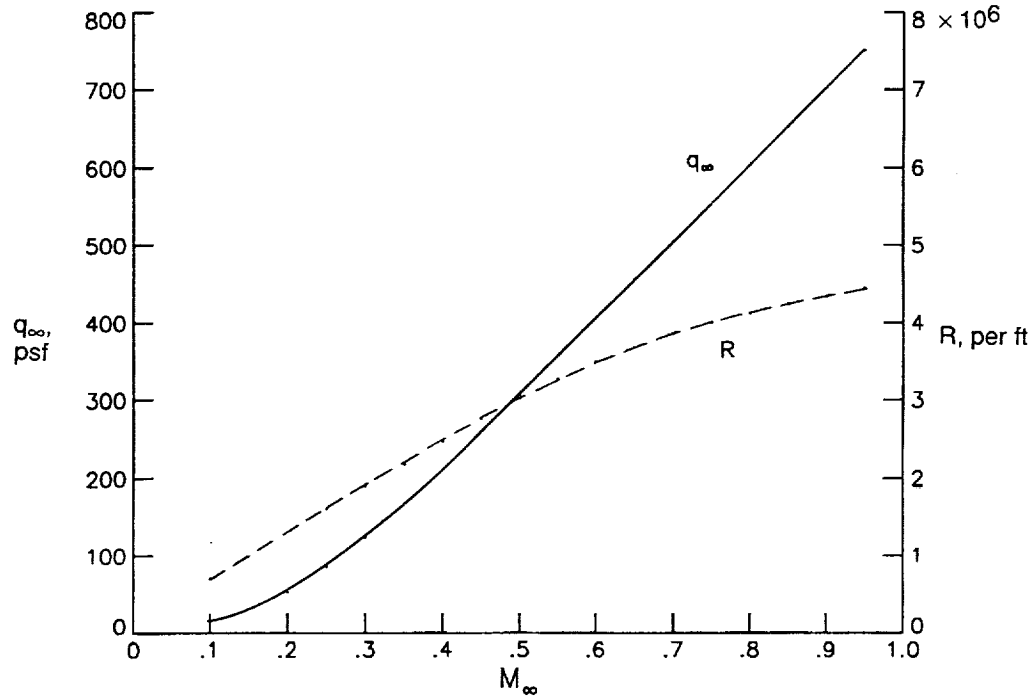

Figure 4. Nominal testing conditions for the Langley 7- by 10-Foot High-Speed Tunnel.

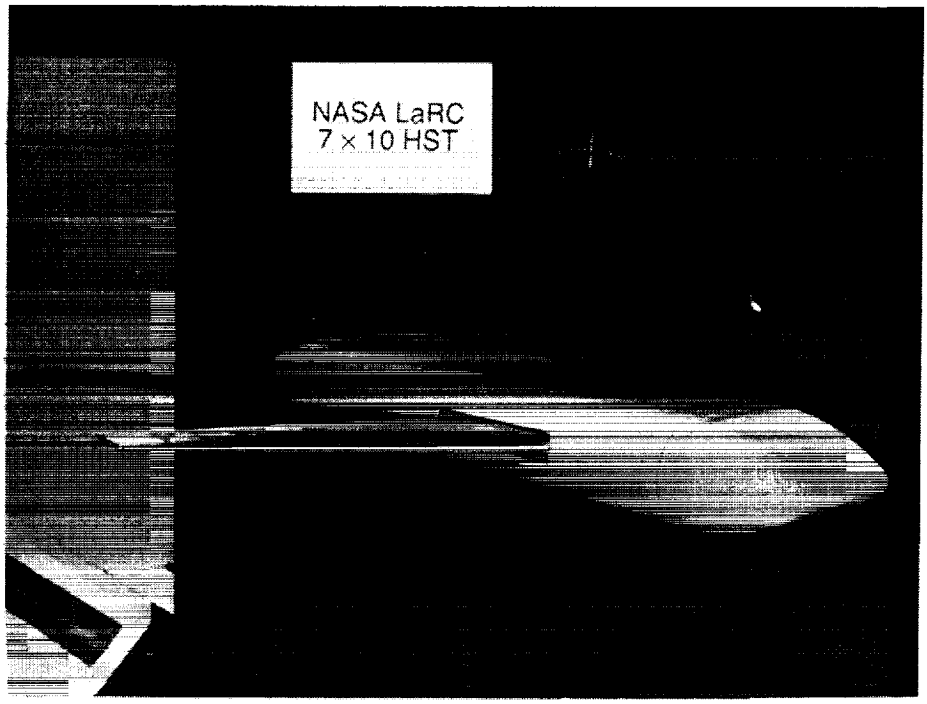

L-89-10608

(a) Model with covers installed on centerbody section.

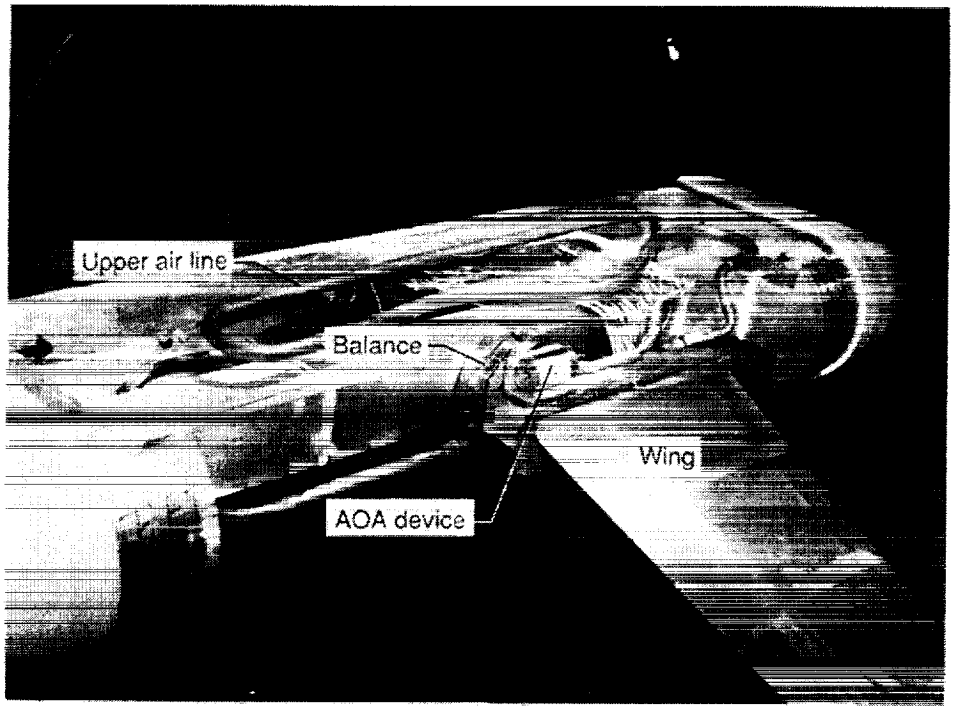

L-89-11515

(b) Model with cover removed from centerbody section.

Figure 5. Photographs of model mounted on sidewall turntable in the Langley 7- by 10-Foot High-Speed Tunnel.

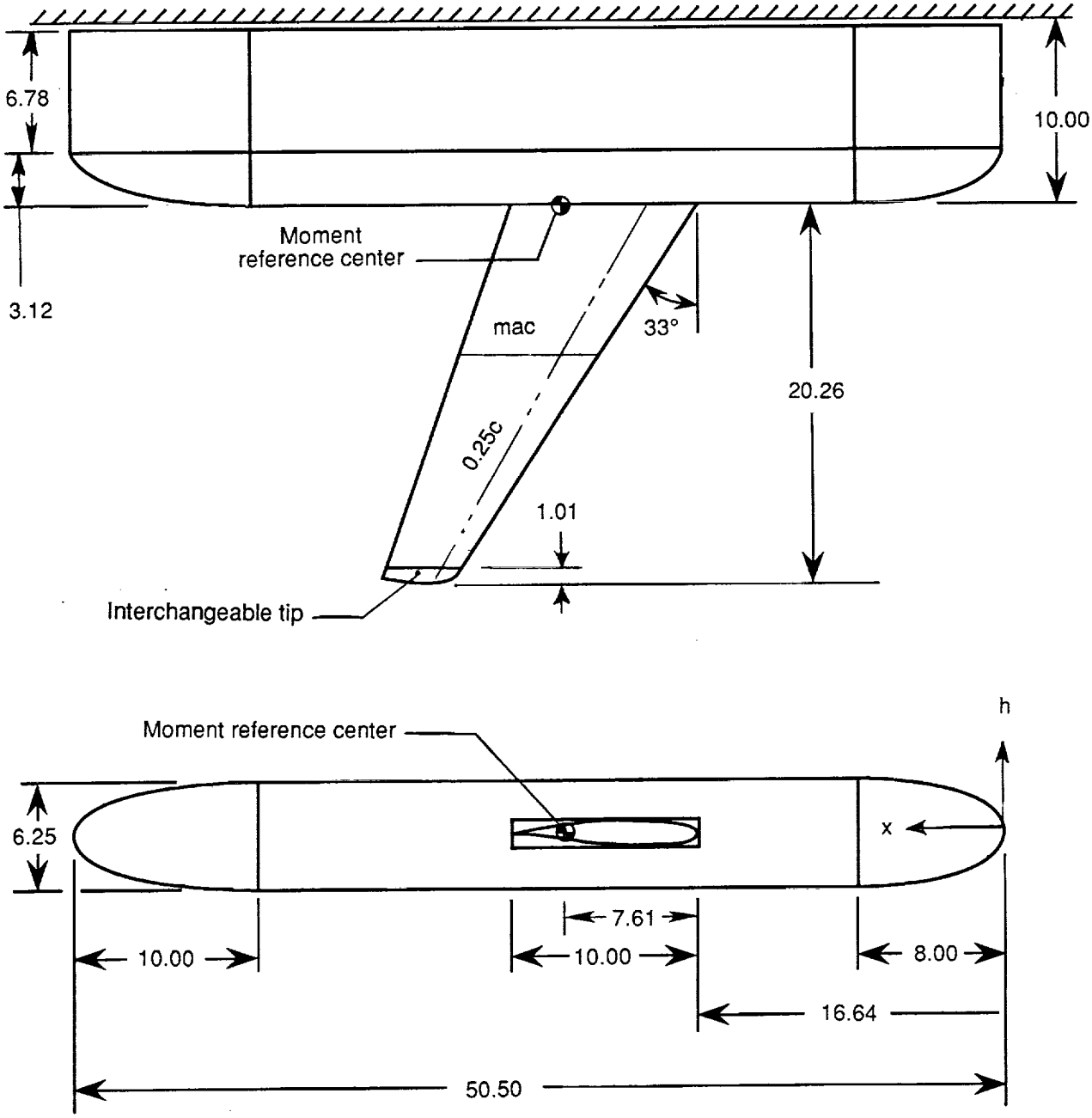

(a) Wing and body.

Figure 6. Details of model and experimental setup. All linear dimensions are given in inches.

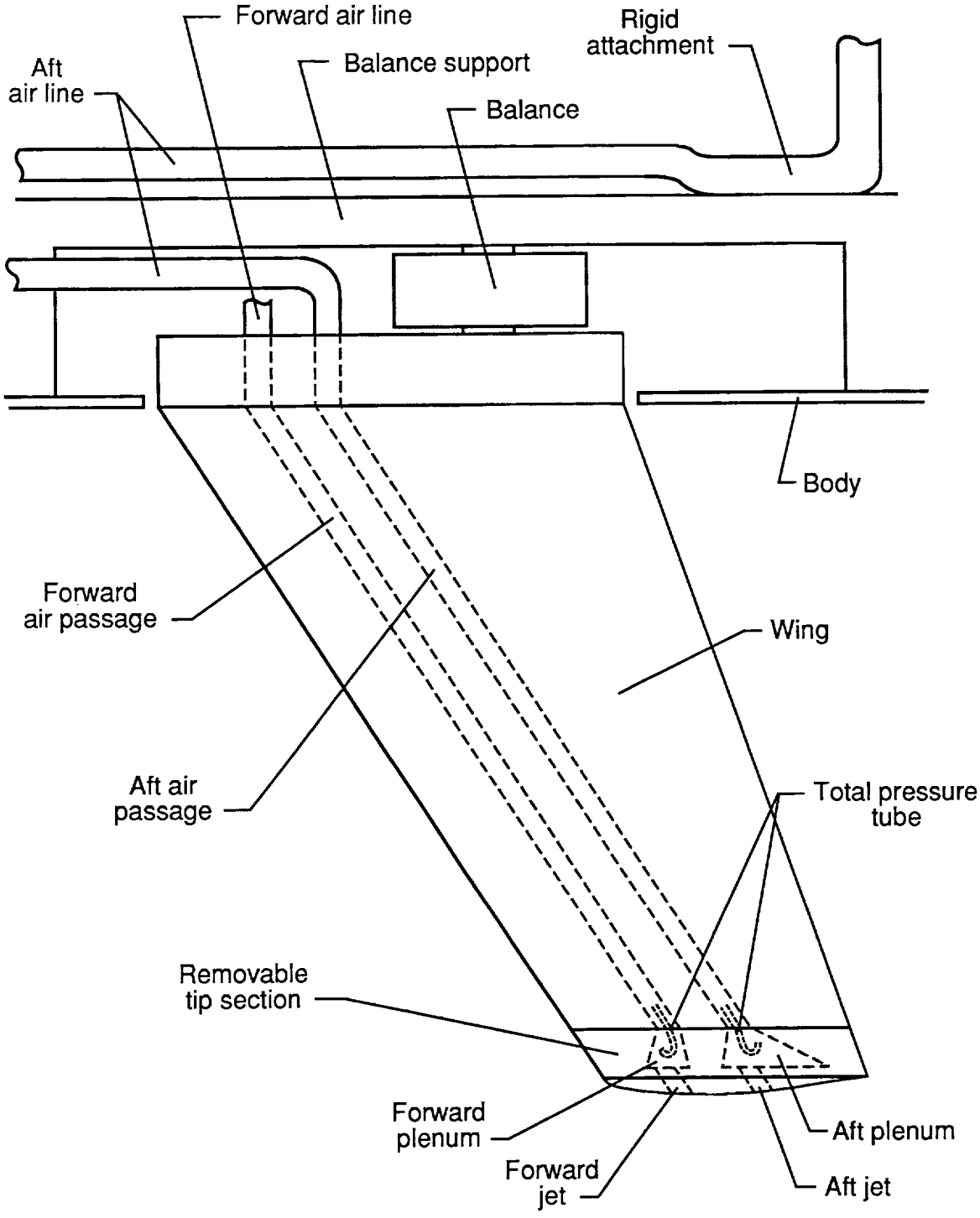

(b) Model components and experimental setup.

Figure 6. Continued.

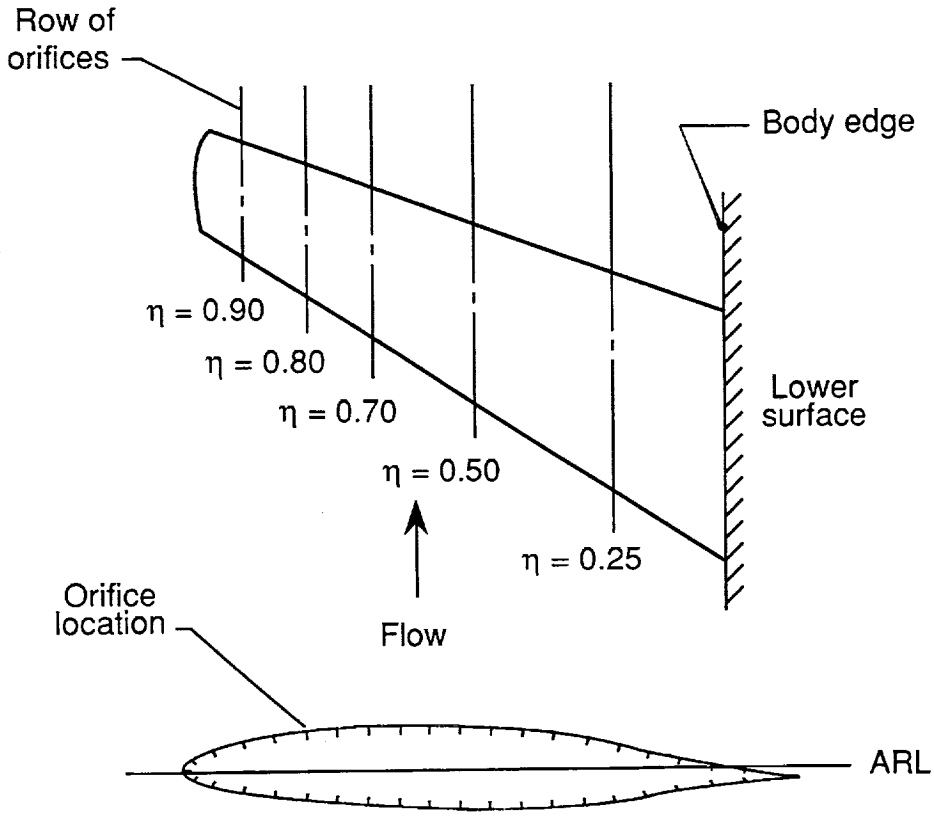

(c) Locations of static pressure orifices on upper and lower surfaces of model.

Figure 6. Concluded.

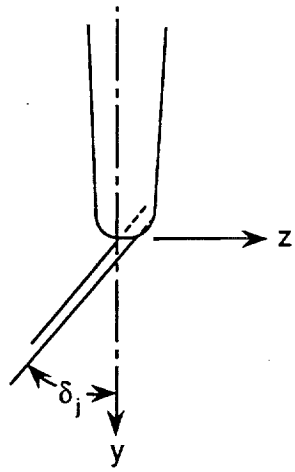

(a) View from downstream.

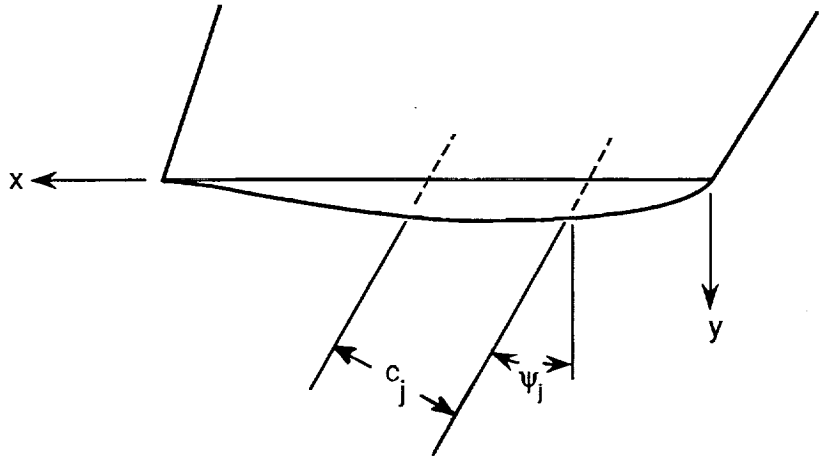

(b) View of upper surface.

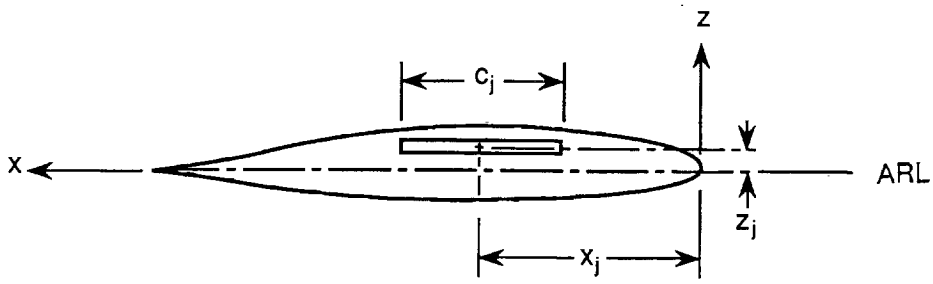

(c) View from side.

Figure 7. Parameters used to describe wingtip jets. Tip is shown upright.

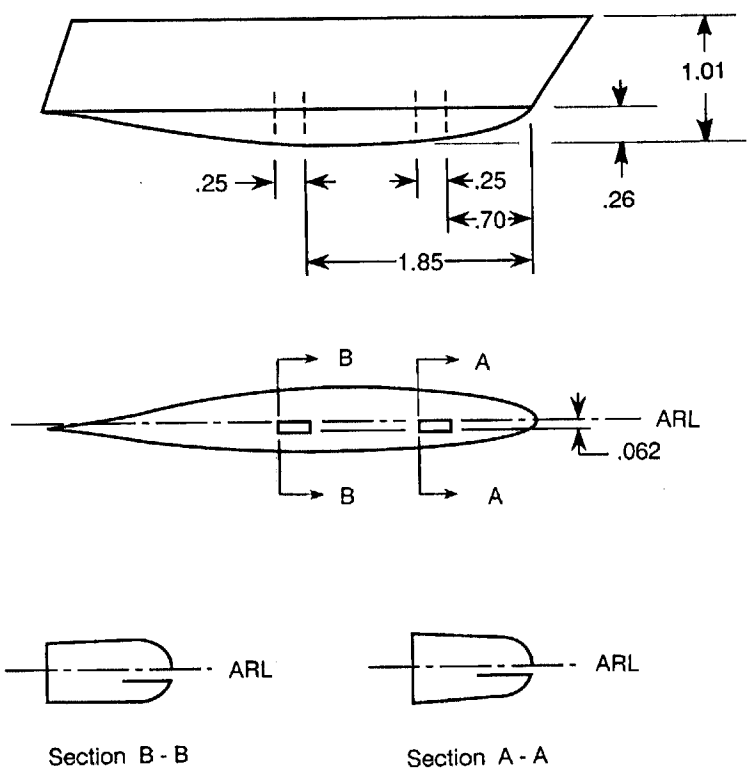

(a) Tip 1.

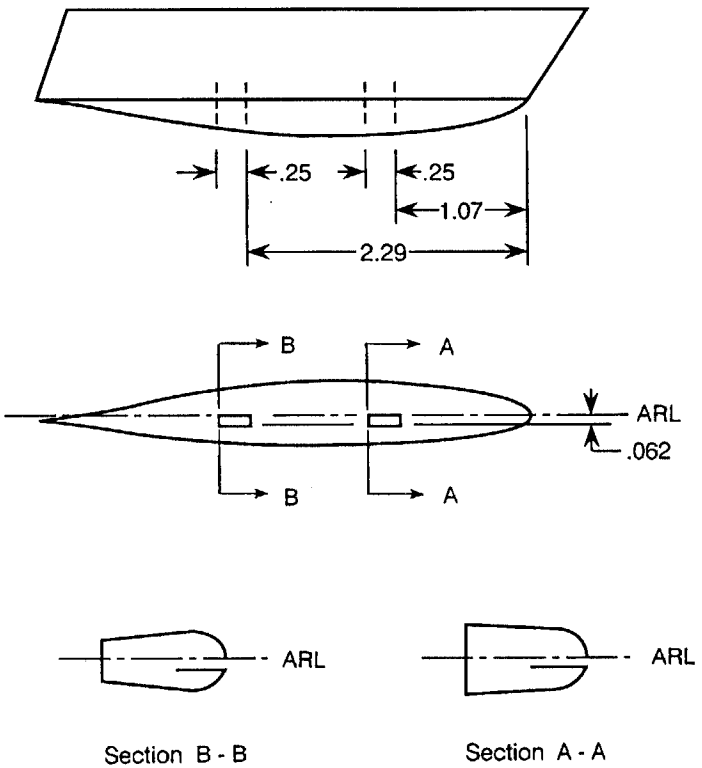

(b) Tip 2.

Figure 8. Sketches of interchangeable wingtip sections showing jet-exit locations. All linear dimensions are given in inches.

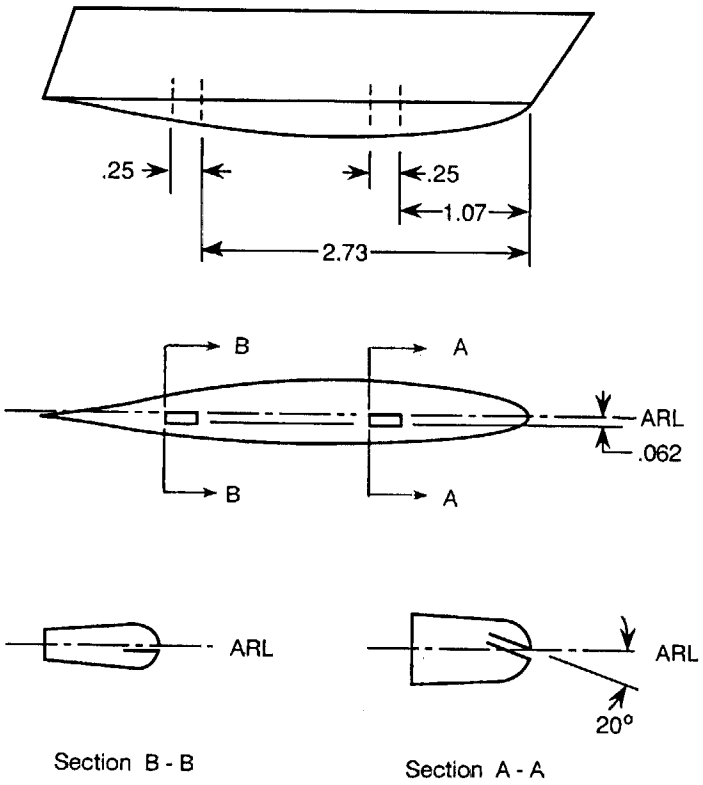

(c) Tip 3.

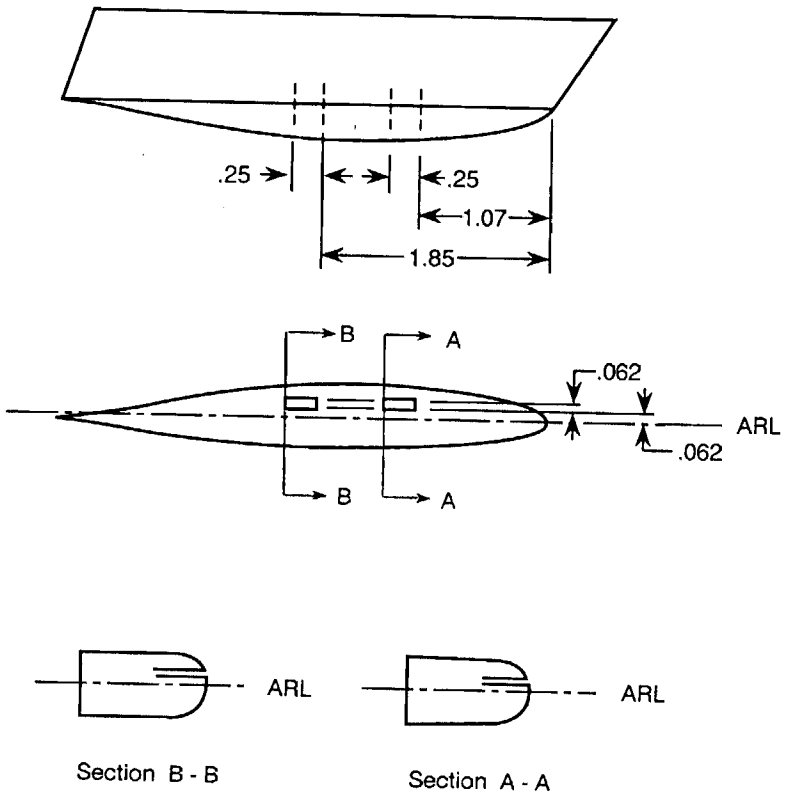

(d) Tip 6.

Figure 8. Continued.

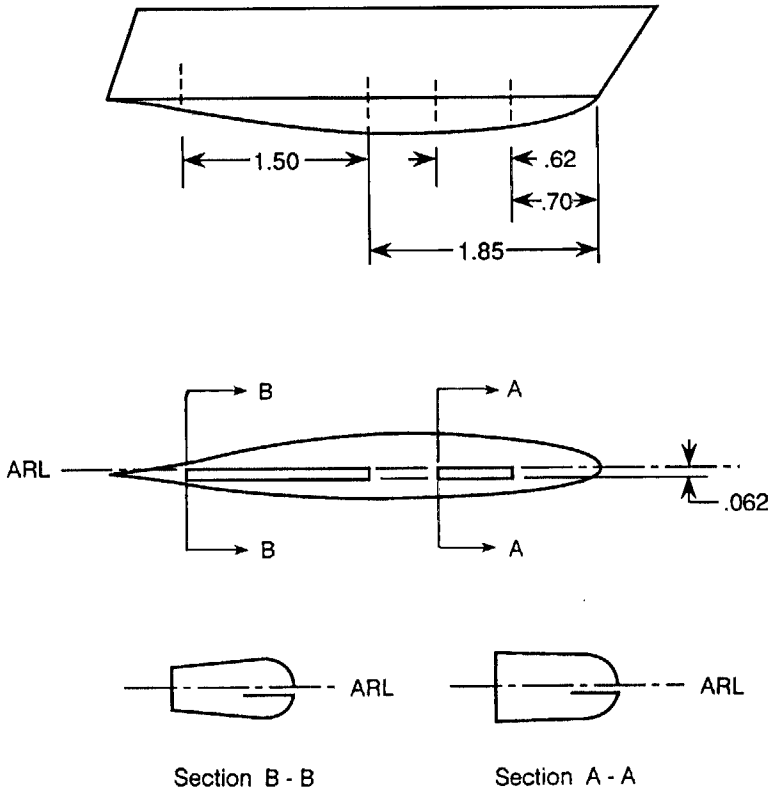

(e) Tip 8.

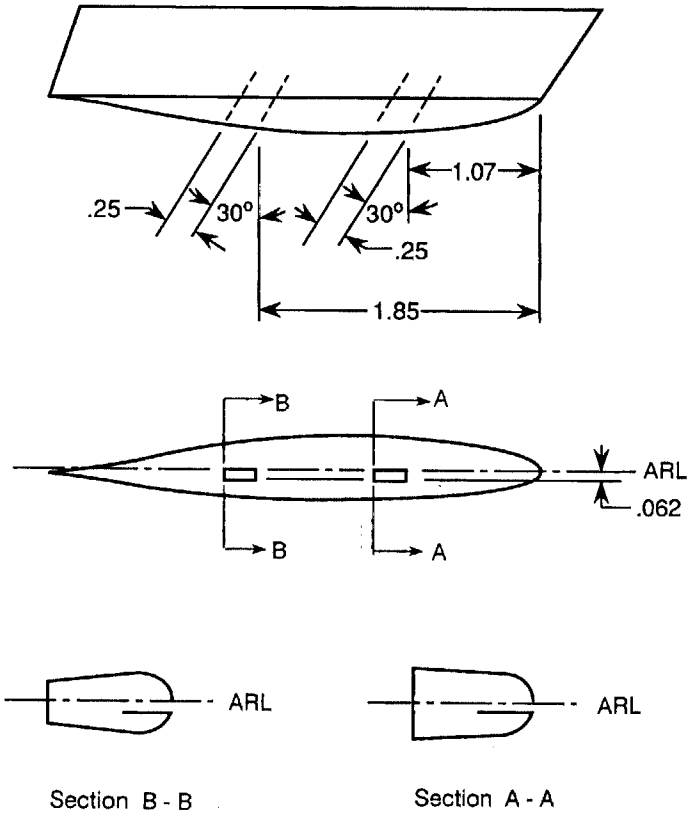

(f) Tip 9.

Figure 8. Concluded.

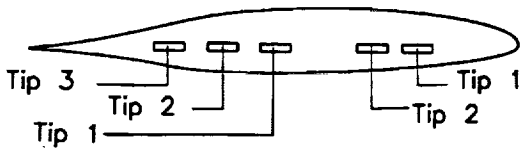

(a) Chordwise location.

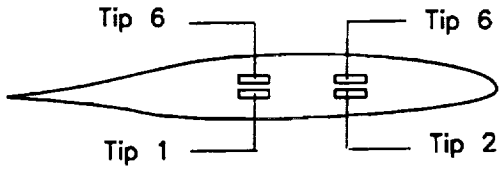

(b) Vertical location.

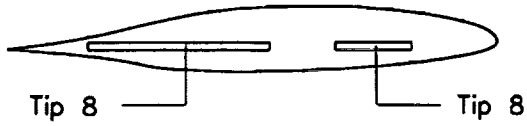

(c) Chordwise length.

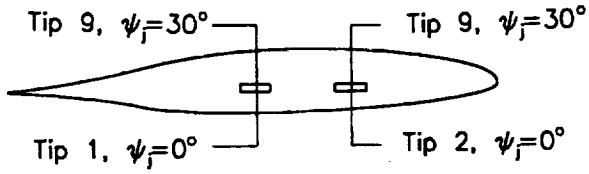

(d) In-plane deflection (sweep).

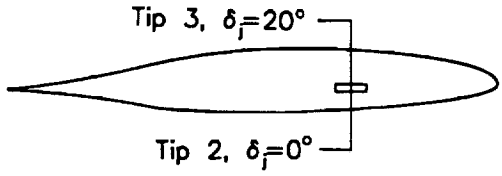

(e) Out-of-plane deflection (dihedral).

Figure 9. Comparison of jet-exit locations and exhaust directions for interchangeable tip sections.

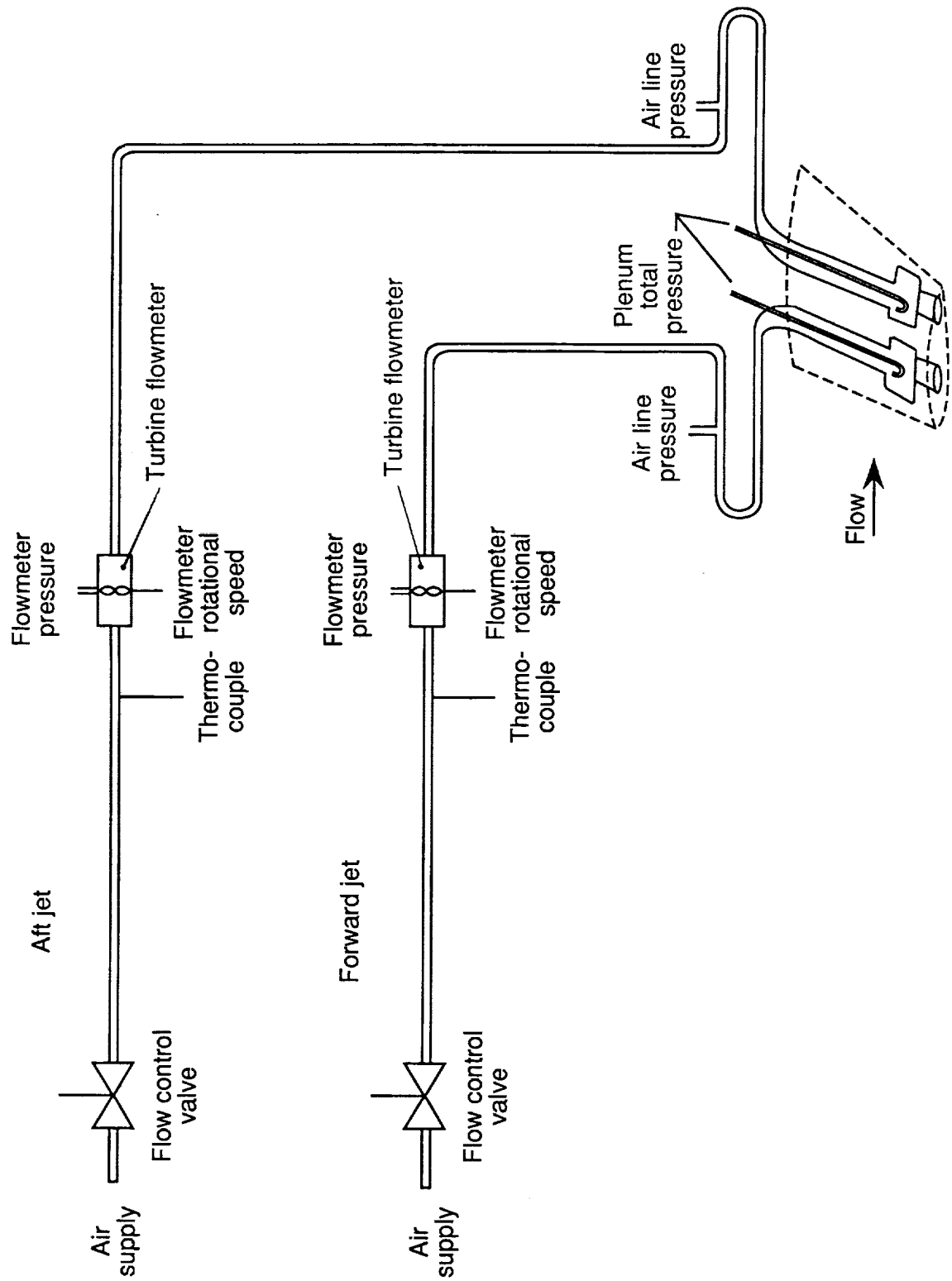

Figure 10. Schematic diagram of air supply system and associated instrumentation.

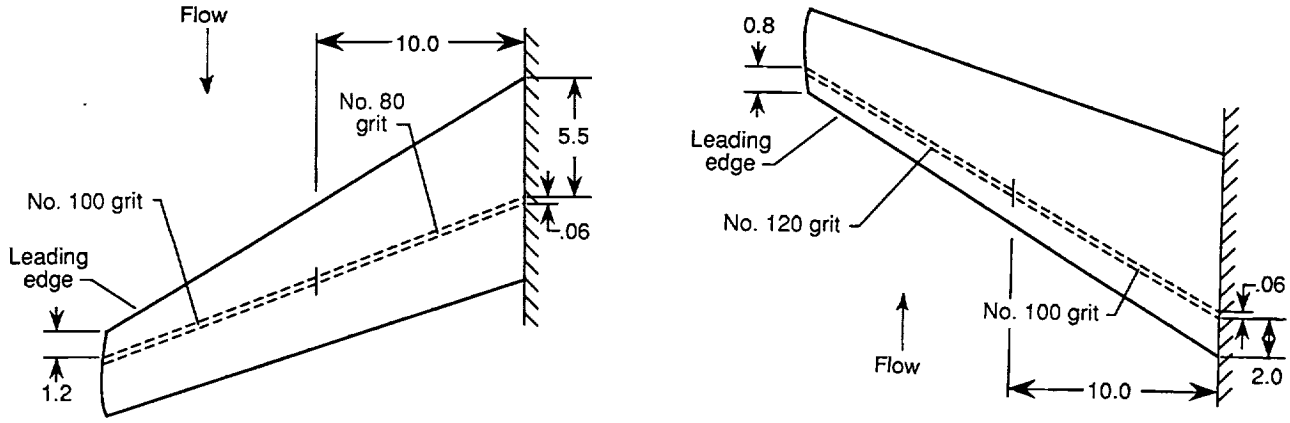

(a) Upper surface.

(b) Lower surface.

Figure 11. Sketch showing size and location of grit transition strips. All dimensions are given in inches.

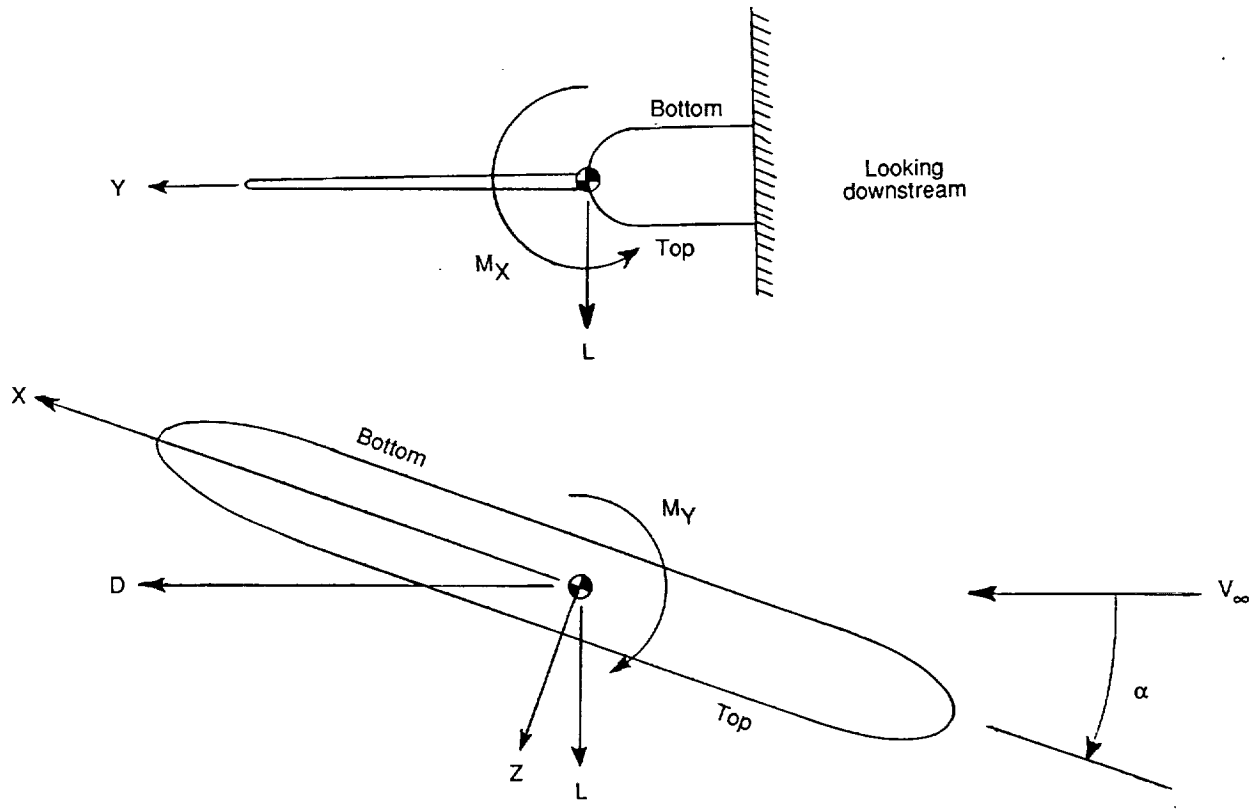

Figure 12. Axis system used for forces and moments. Model is shown inverted (as tested).

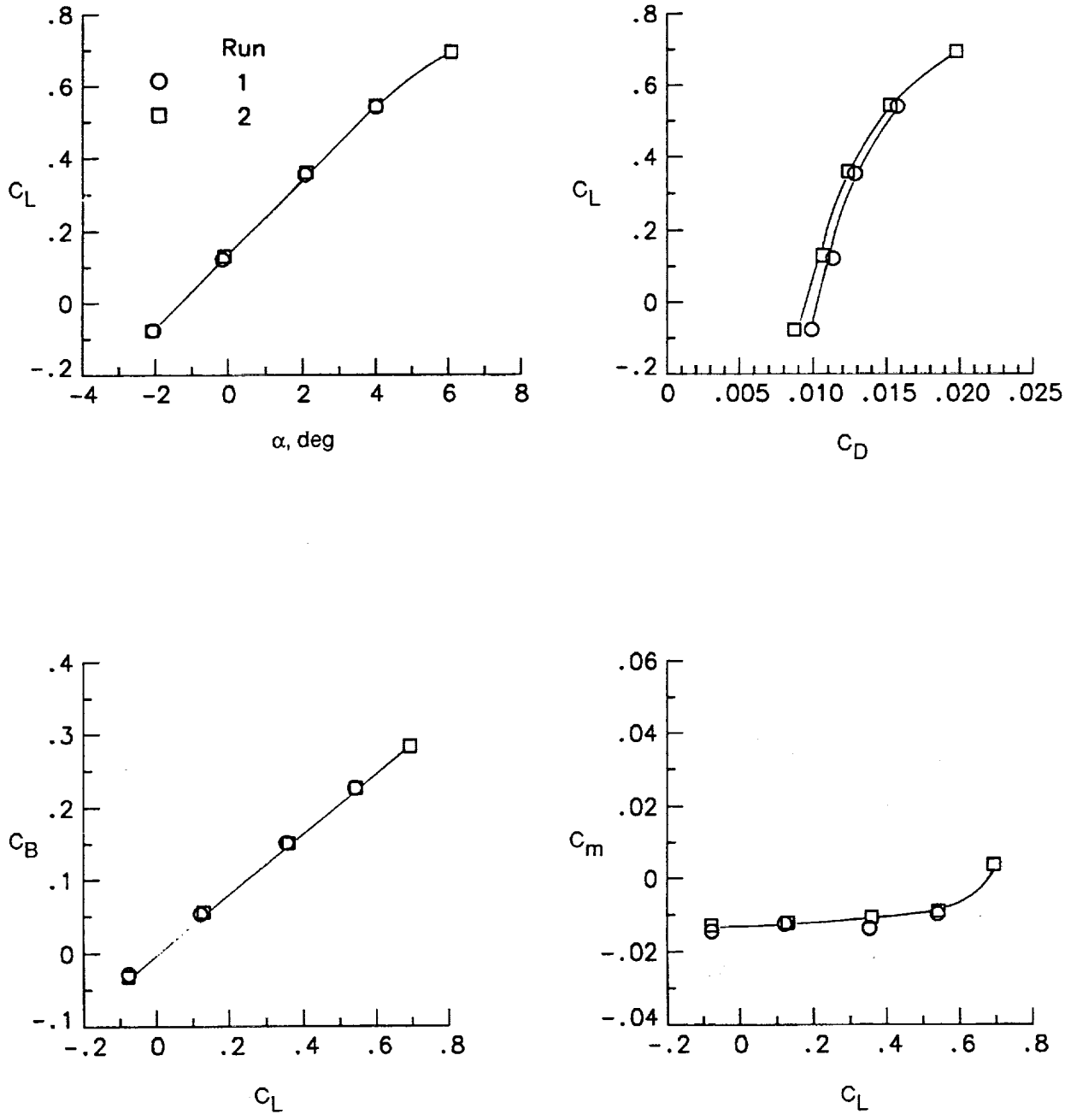

(a) Tip 2.

Figure 13. Repeatability of wing force and moment coefficients without blowing at $M_\infty = 0.30$.

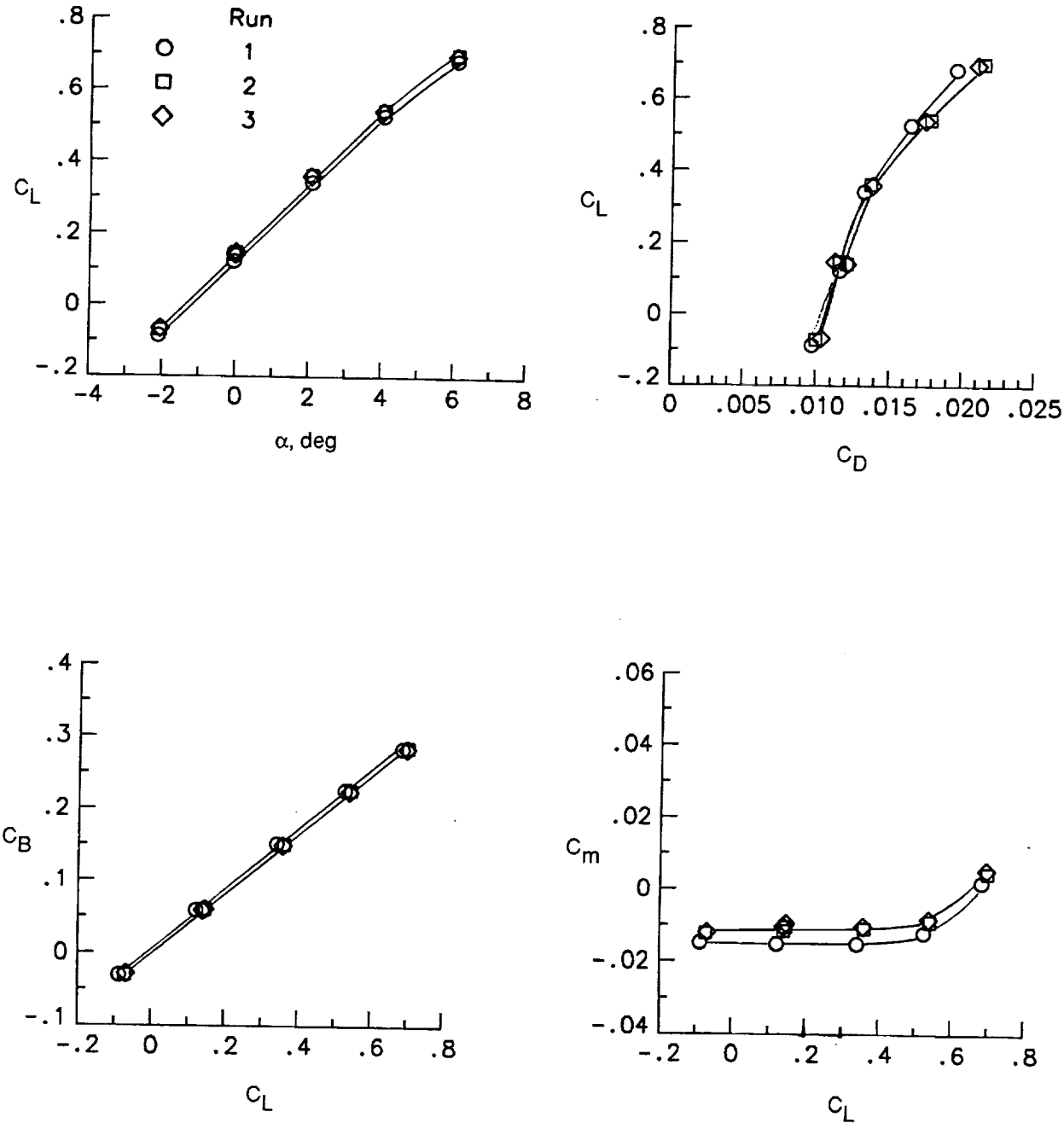

(b) Tip 8.

Figure 13. Concluded.

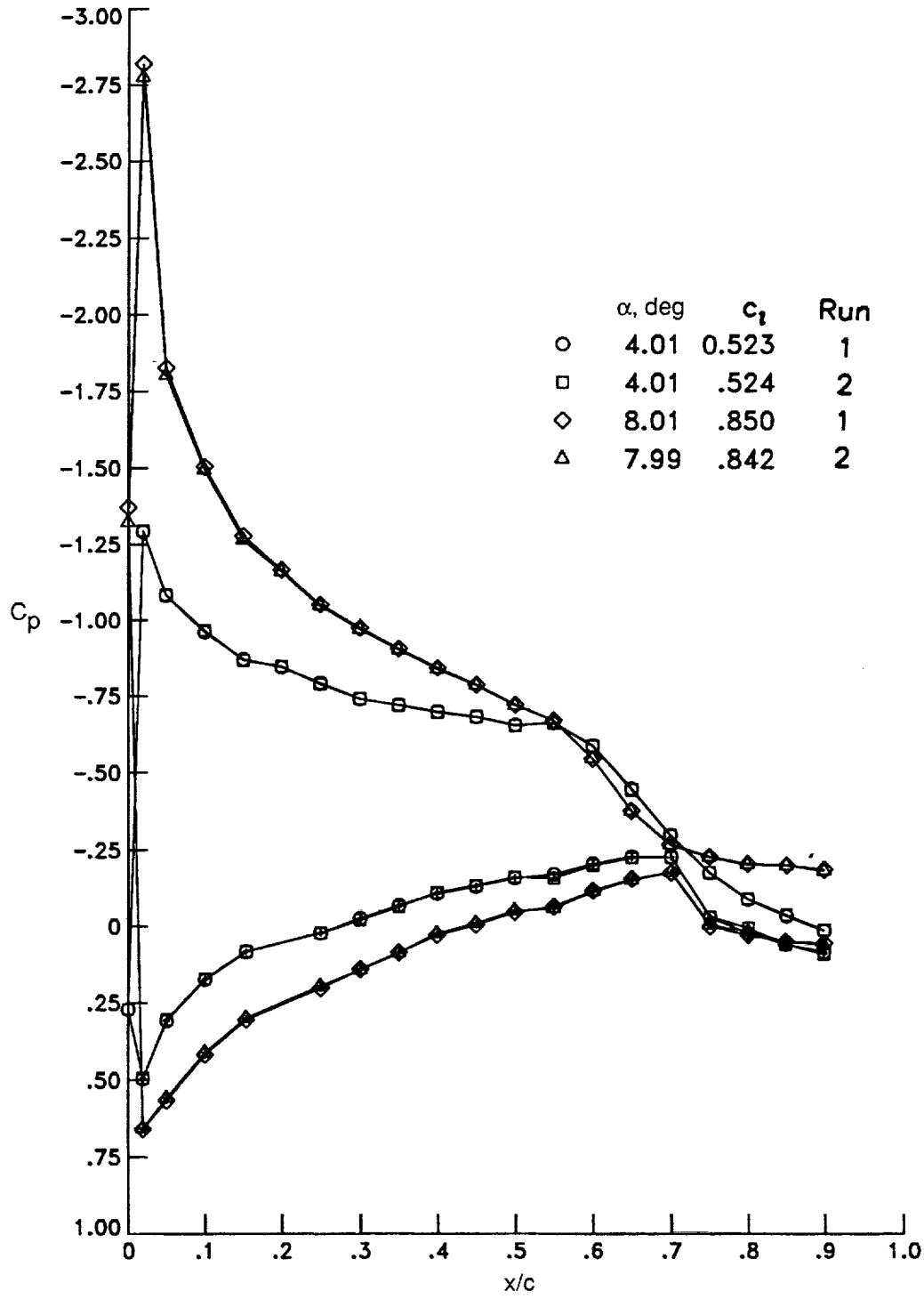

(a) $\eta = 0.25$.

Figure 14. Repeatability of wing chordwise pressure distribution without blowing for tip 2 at $M_\infty = 0.30$. Symbols with "+" denote lower surface results.

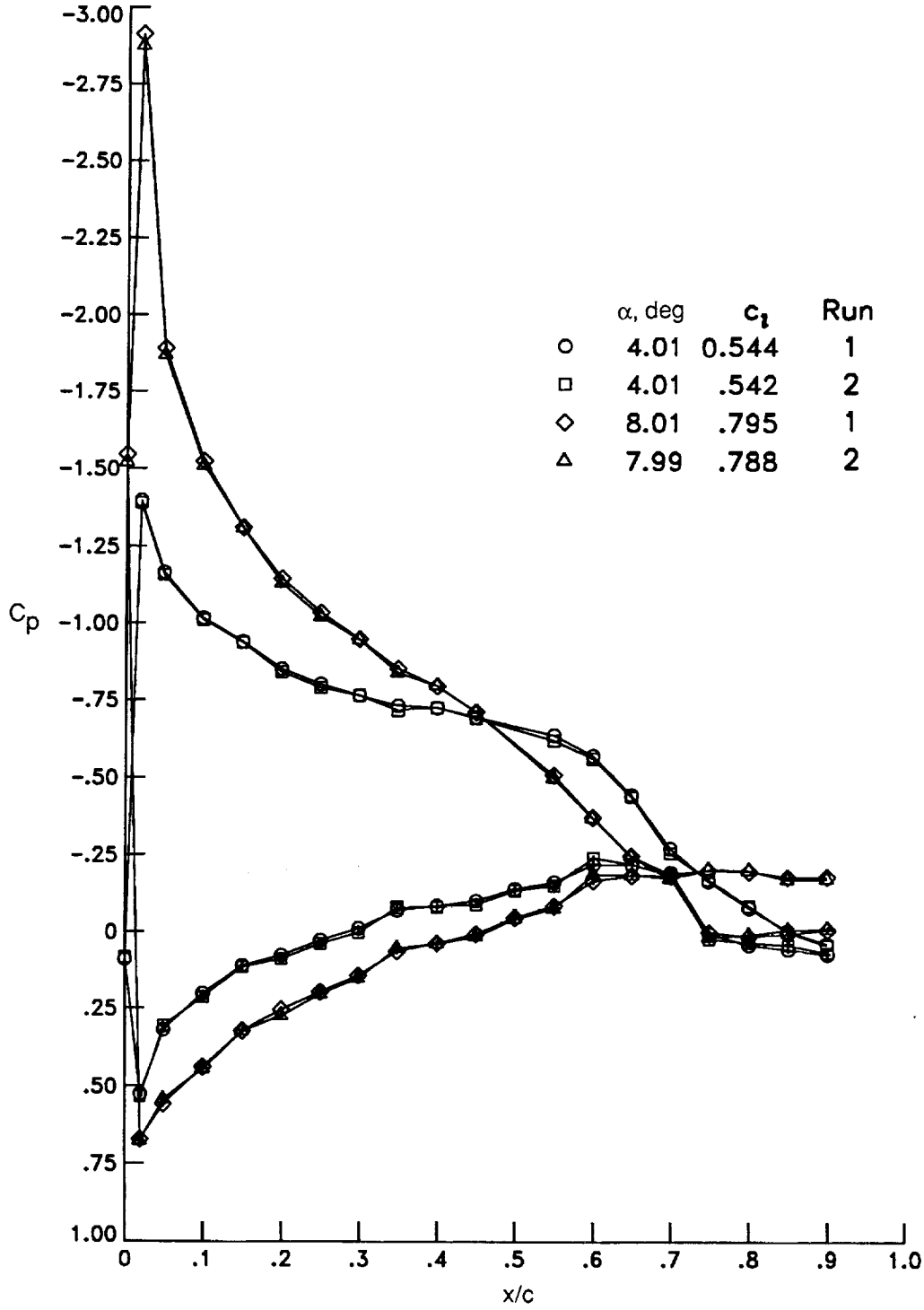

(b) $\eta = 0.50$.

Figure 14. Continued.

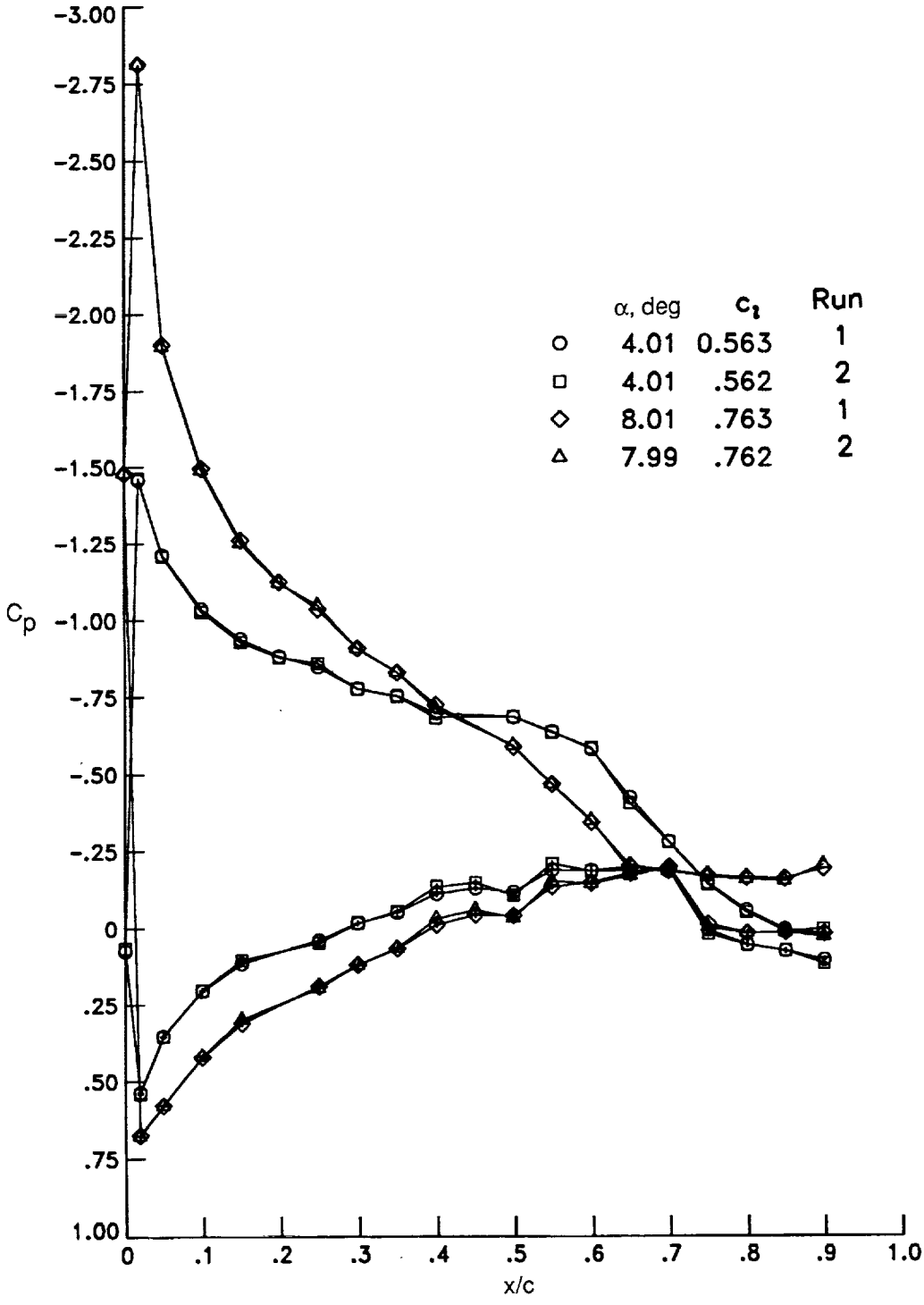

(c) $\eta = 0.70$.

Figure 14. Continued.

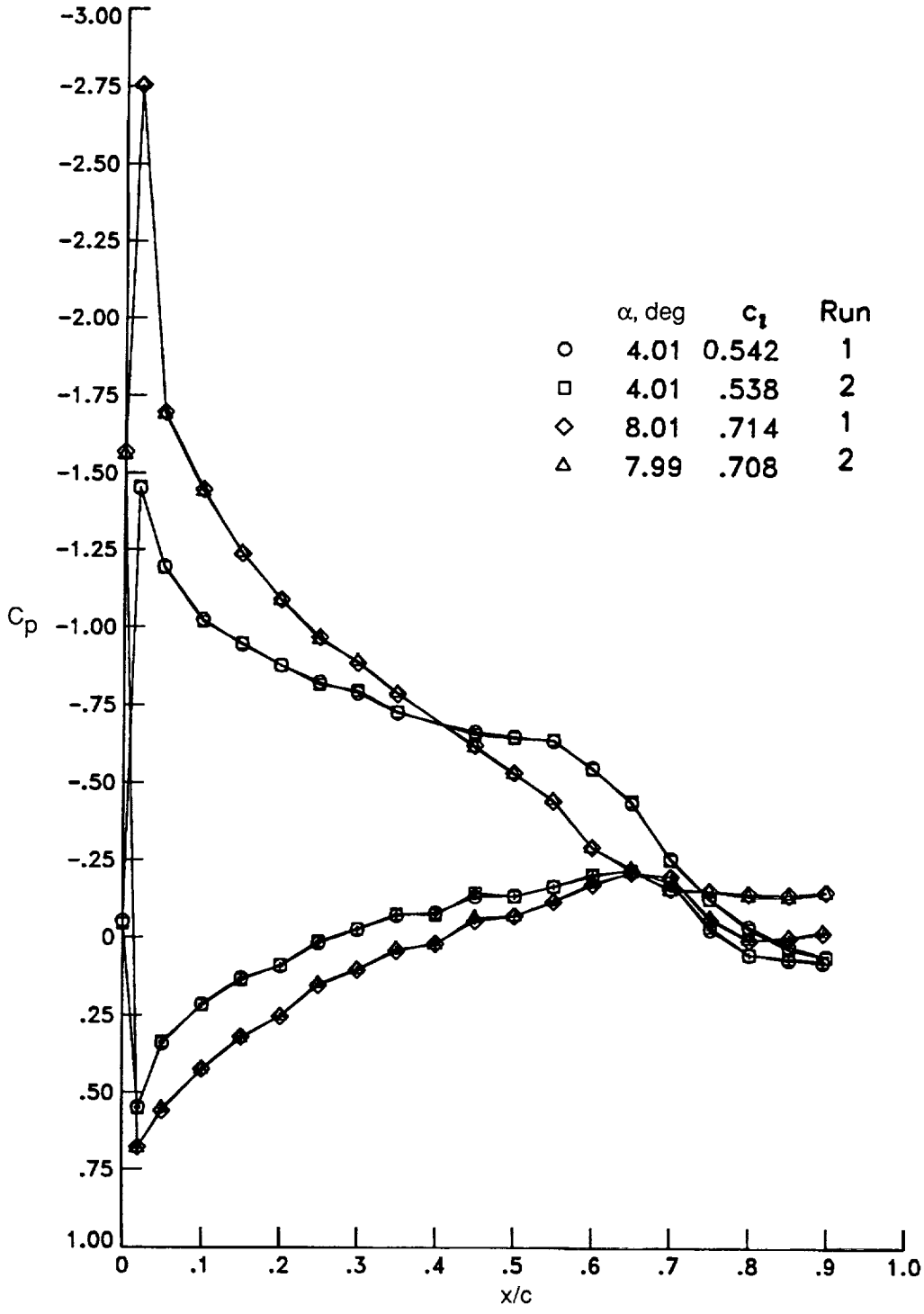

(d) $\eta = 0.80$.

Figure 14. Continued.

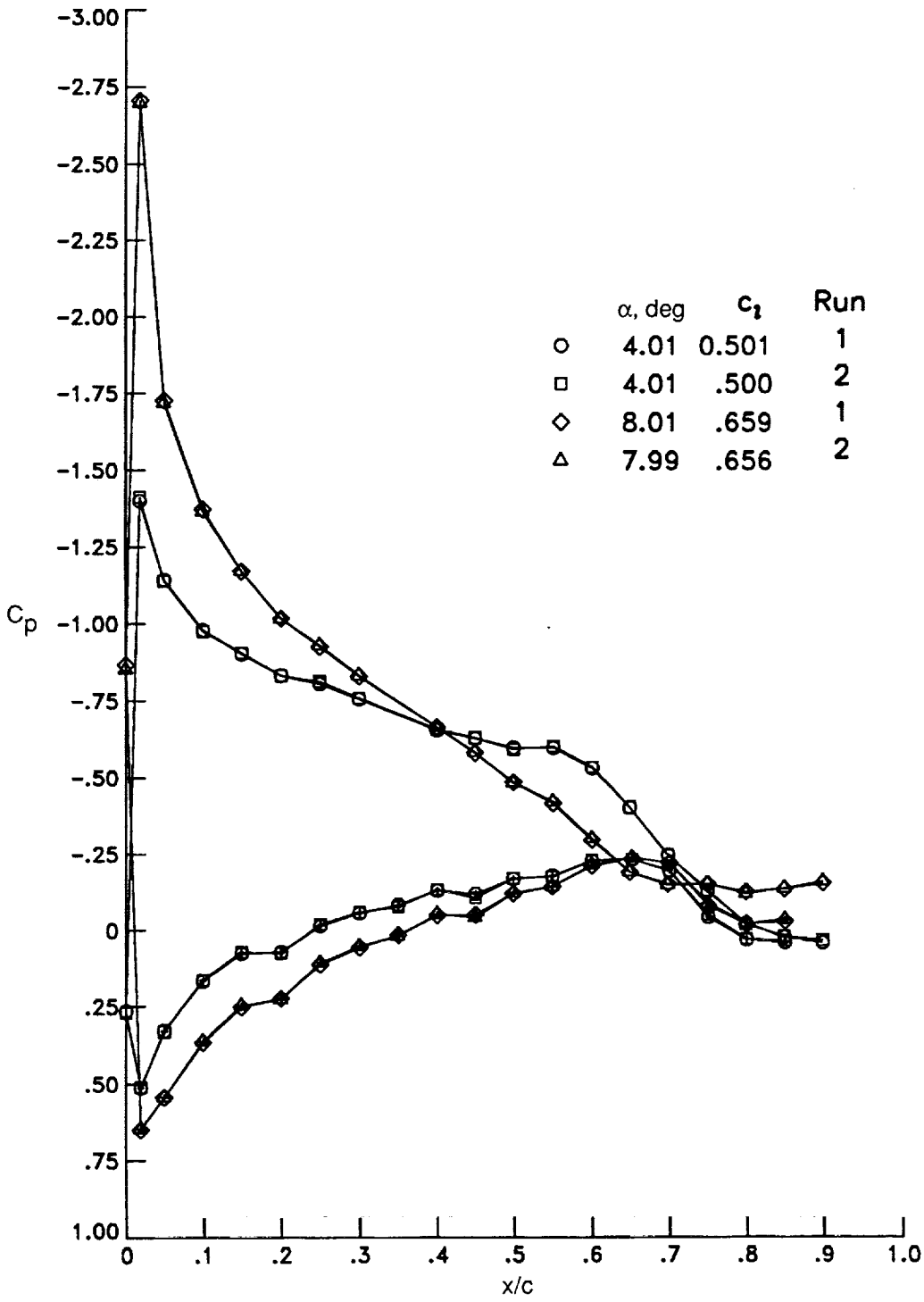

(e) $\eta = 0.90$.

Figure 14. Concluded.

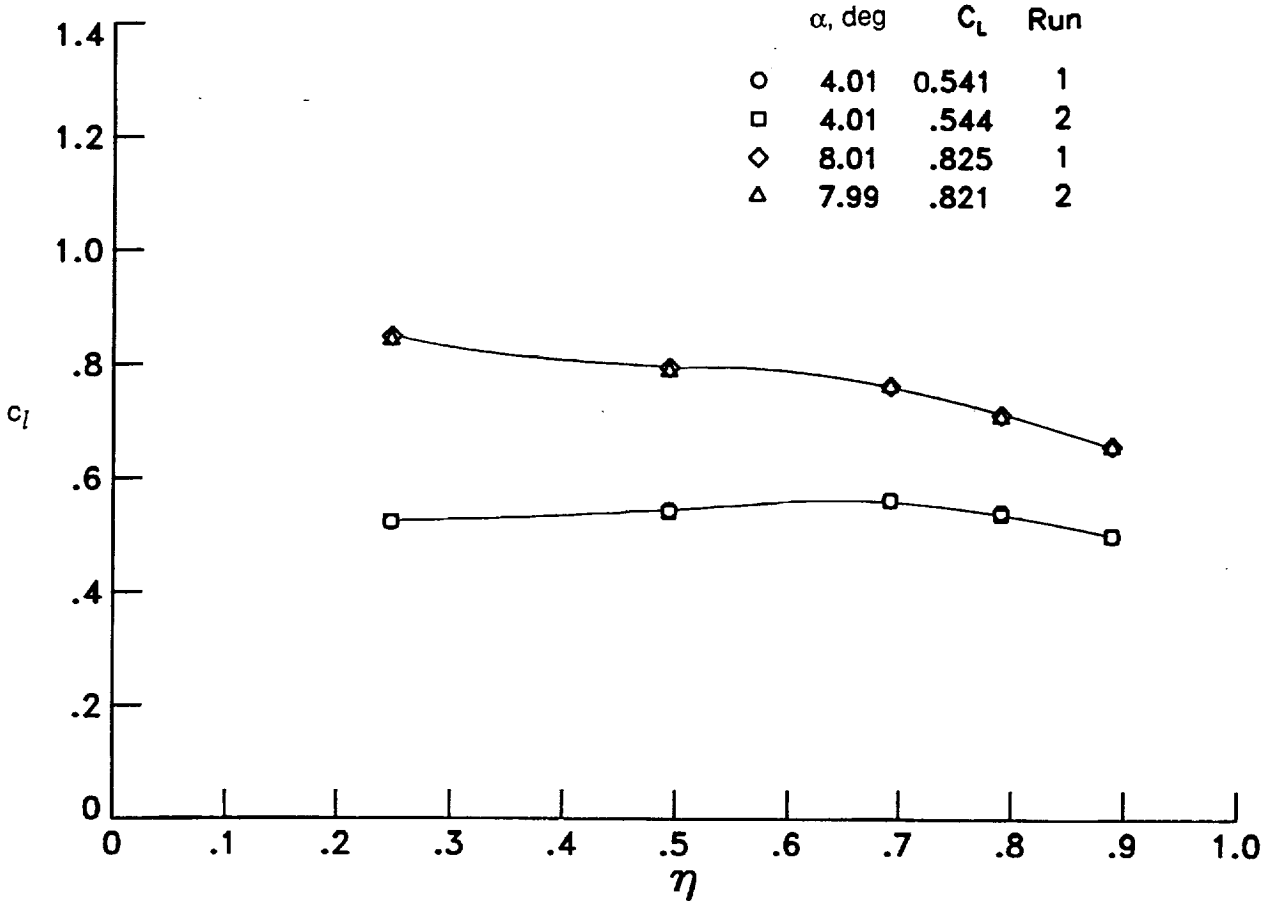

Figure 15. Repeatability of spanwise variation of section lift coefficient without blowing for tip 2 at $M_\infty = 0.30$.

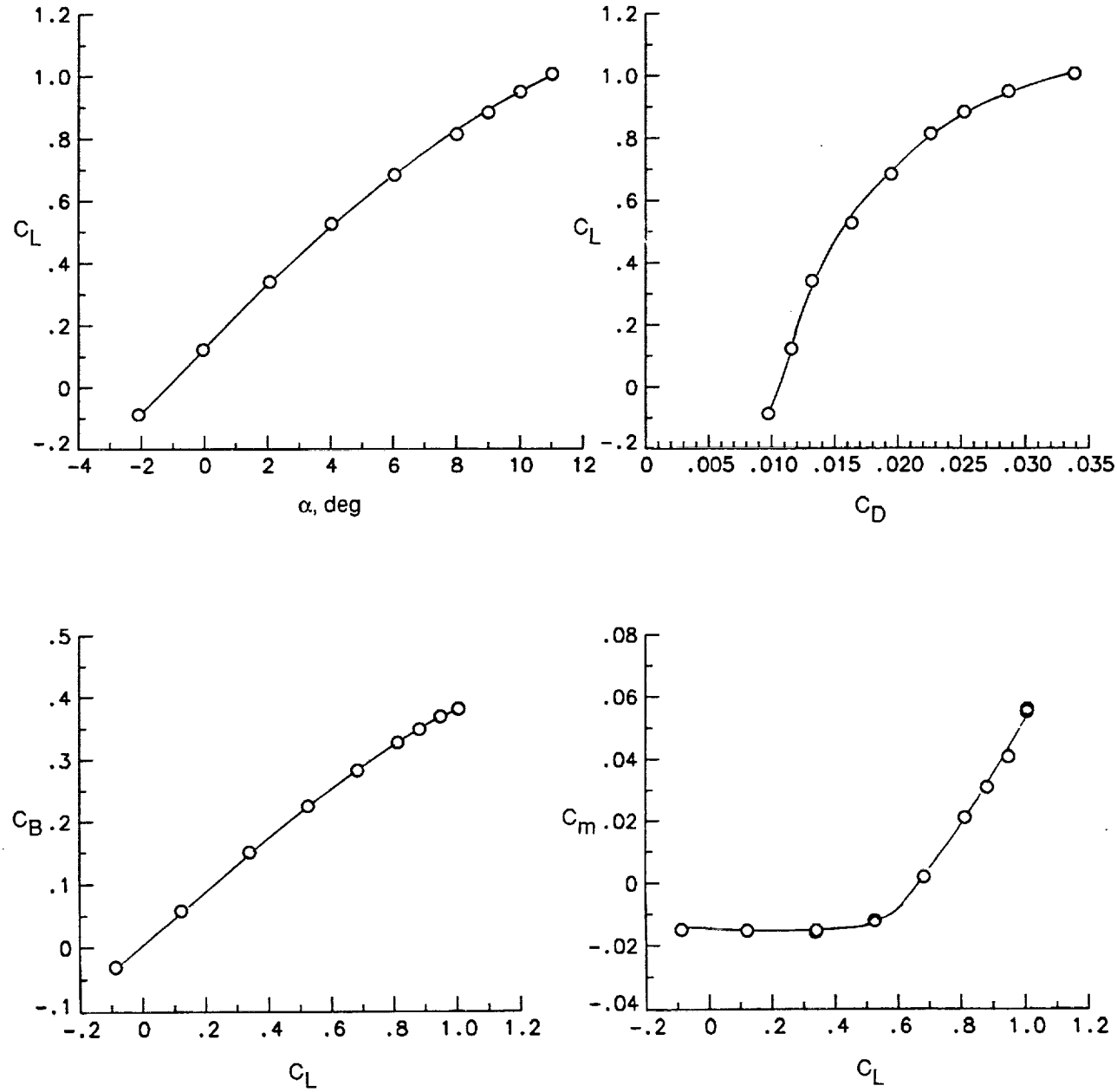

Figure 16. Wing force and moment coefficients without blowing for tip 8 at $M_\infty = 0.30$.

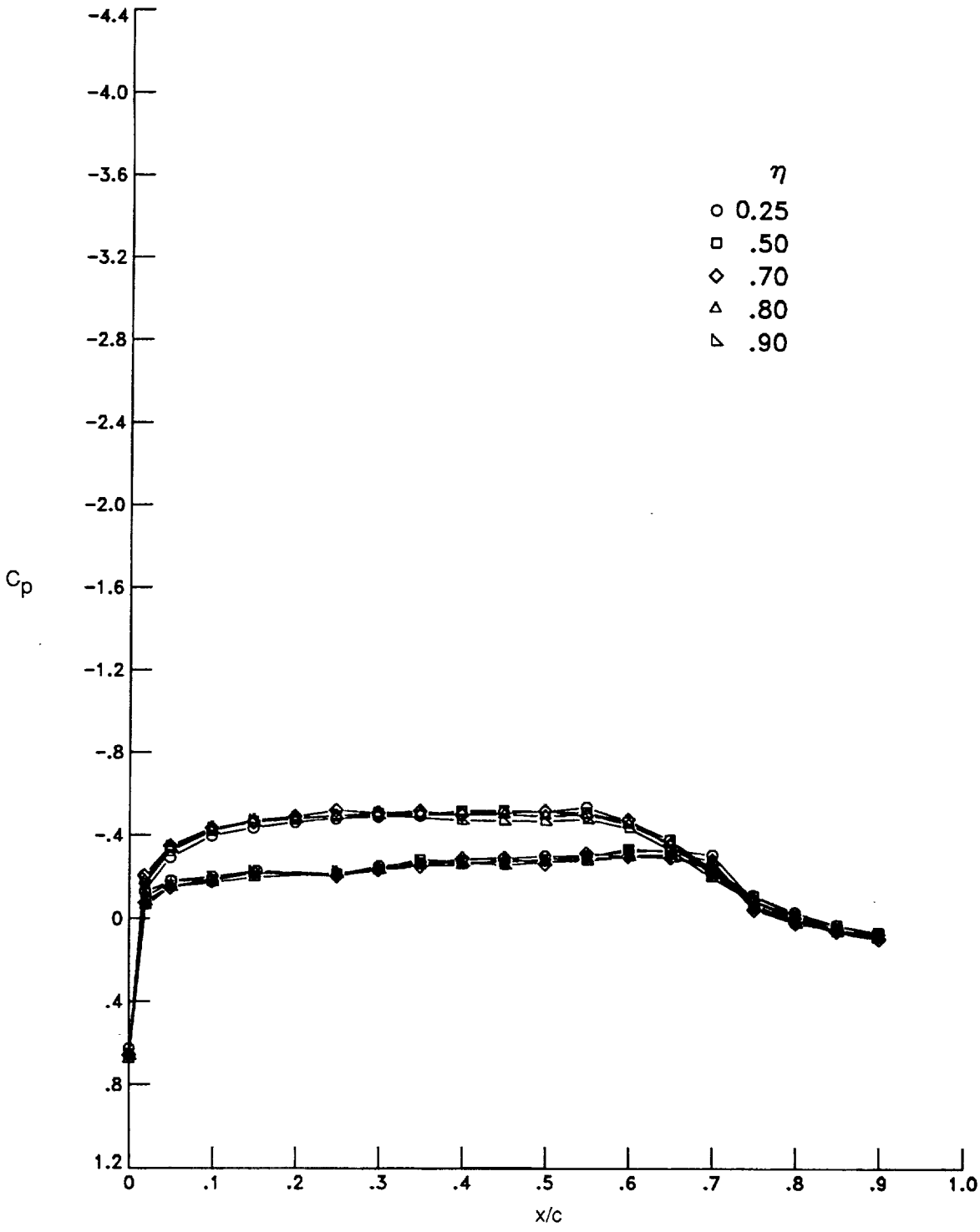

(a) $\alpha = -0.1°$.

Figure 17. Effect of spanwise location on chordwise pressure distribution without blowing for tip 8 at $M_\infty = 0.30$. Symbols with "+" denote lower surface results.

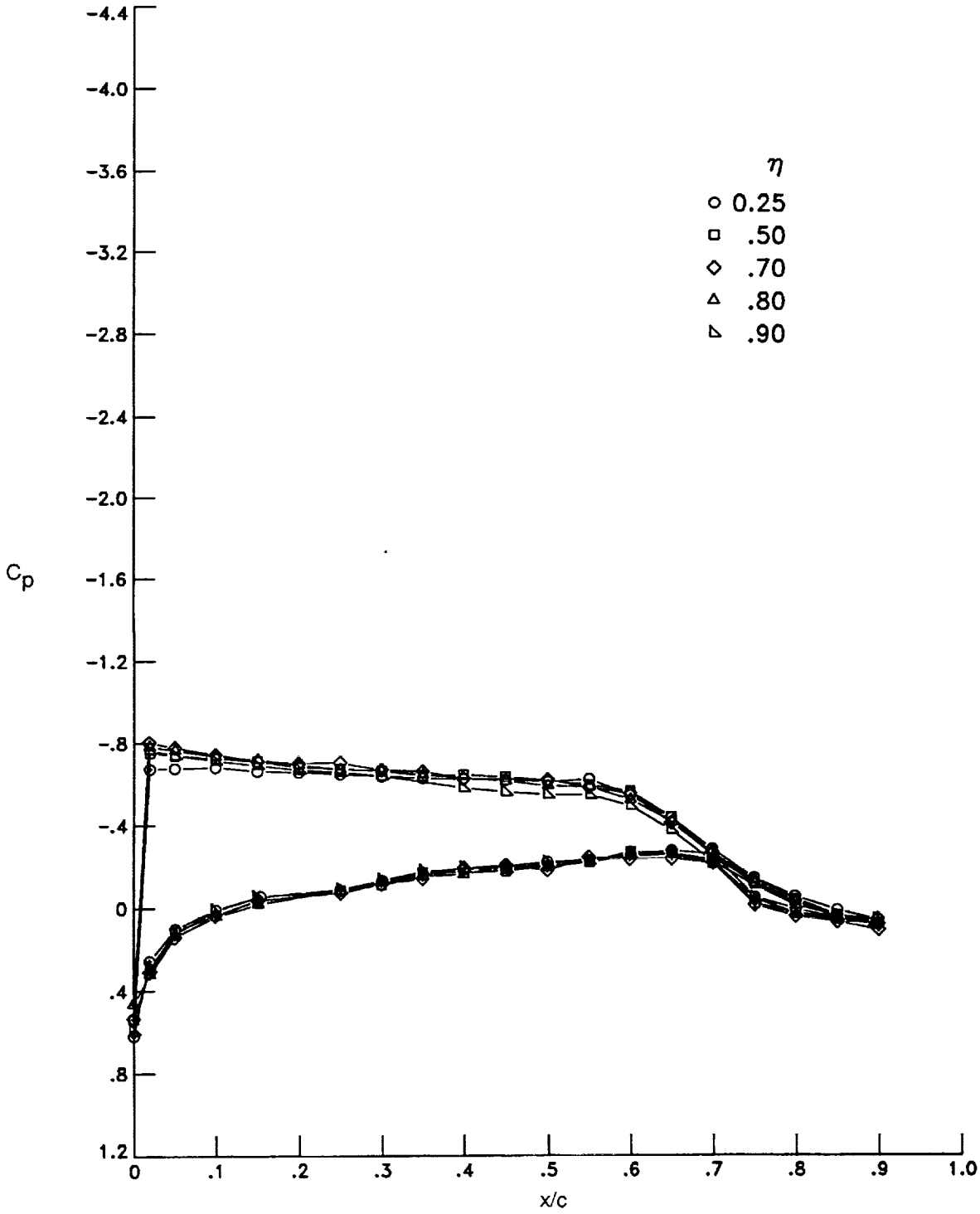

(b) $\alpha = 2.1°$.

Figure 17. Continued.

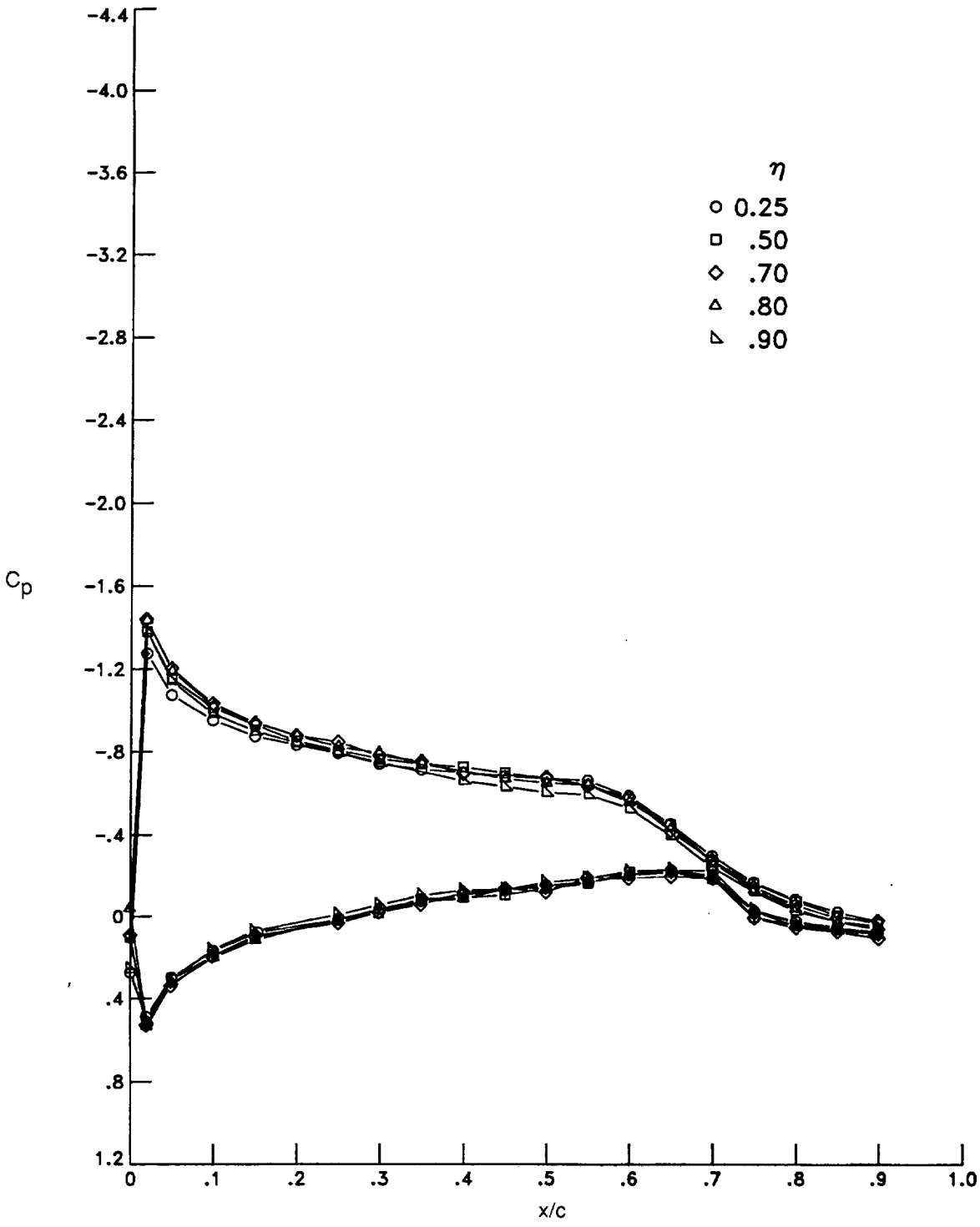

(c) $\alpha = 4°$.

Figure 17. Continued.

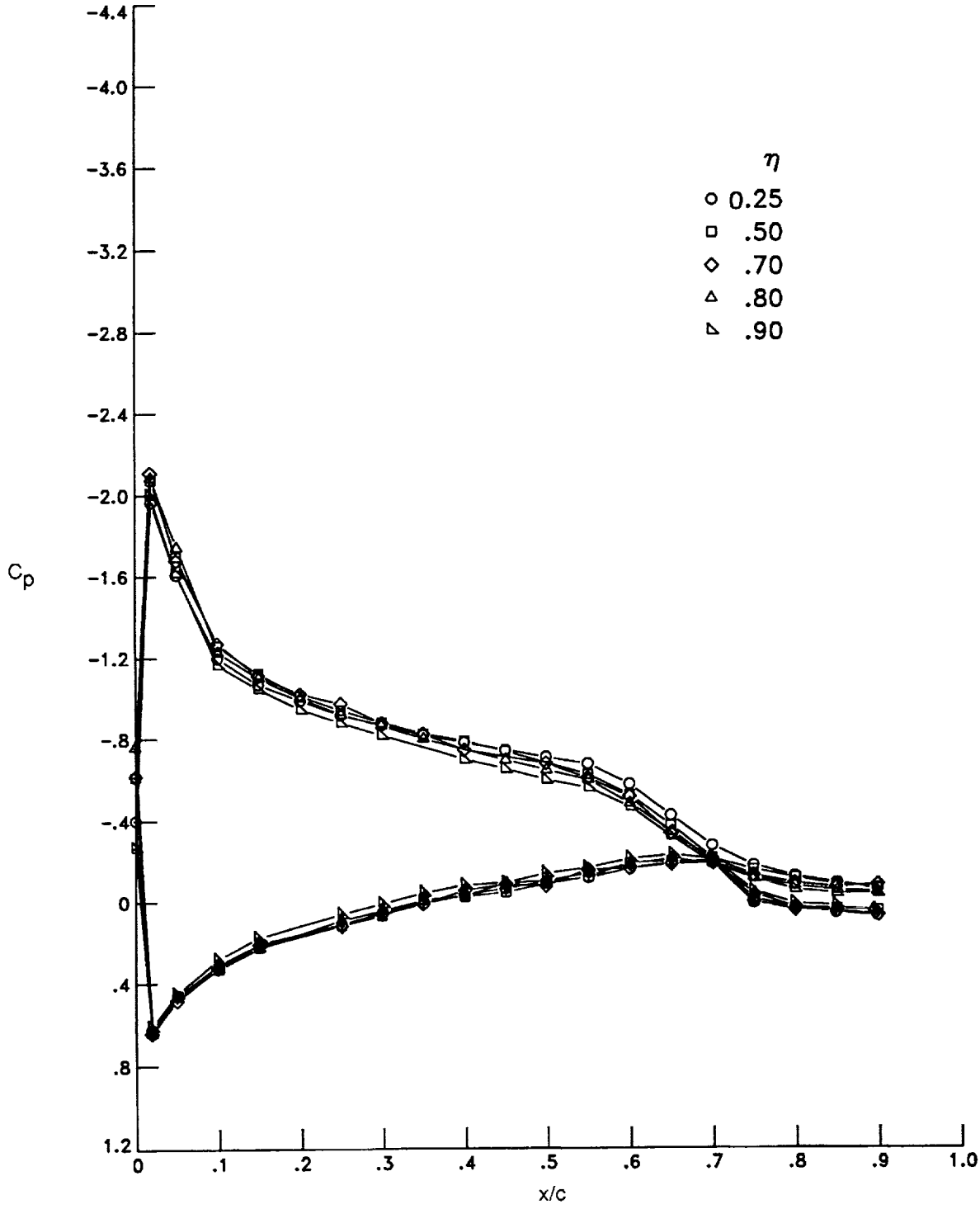

(d) $\alpha = 6°$.

Figure 17. Continued.

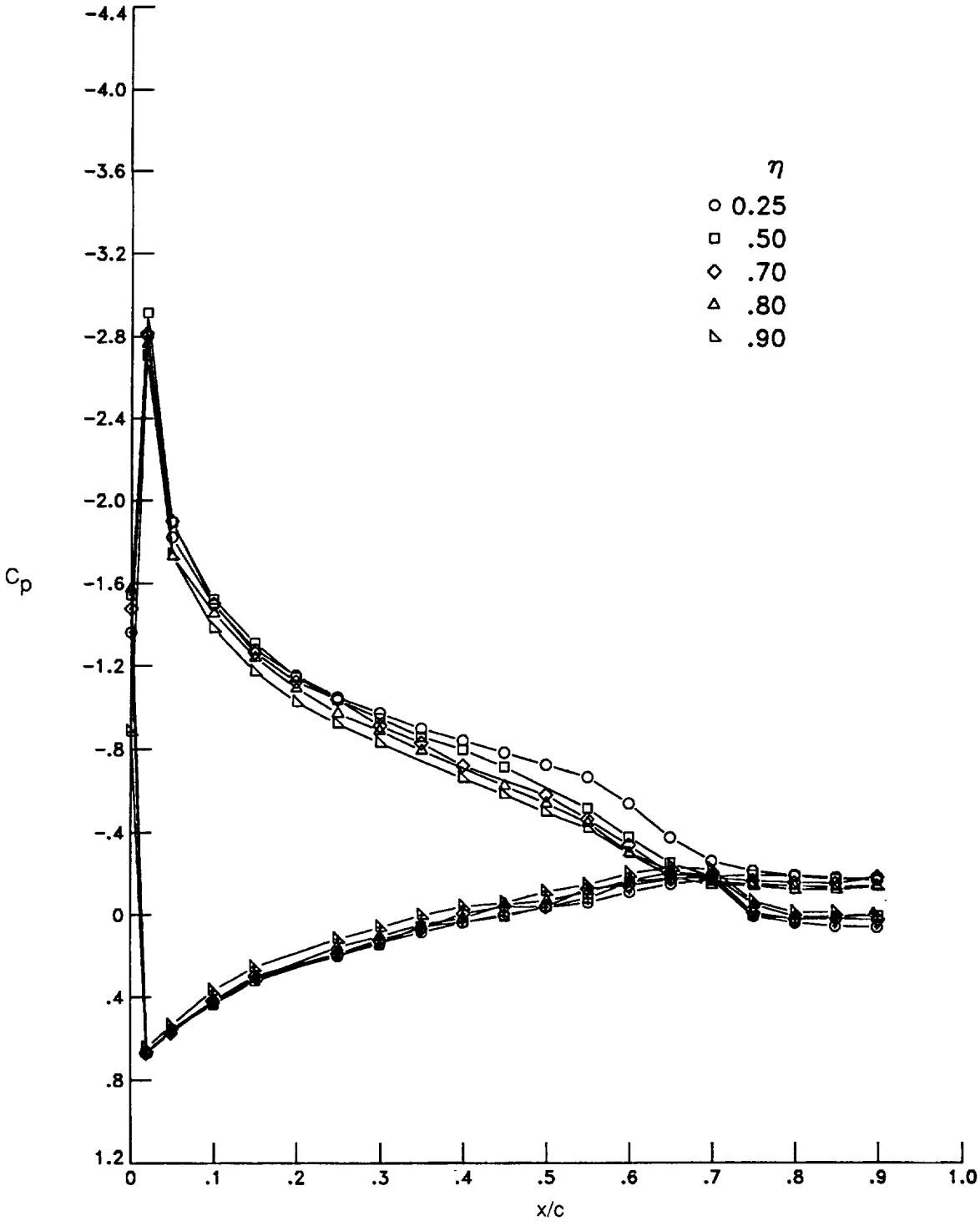

(e) $\alpha = 8°$.

Figure 17. Continued.

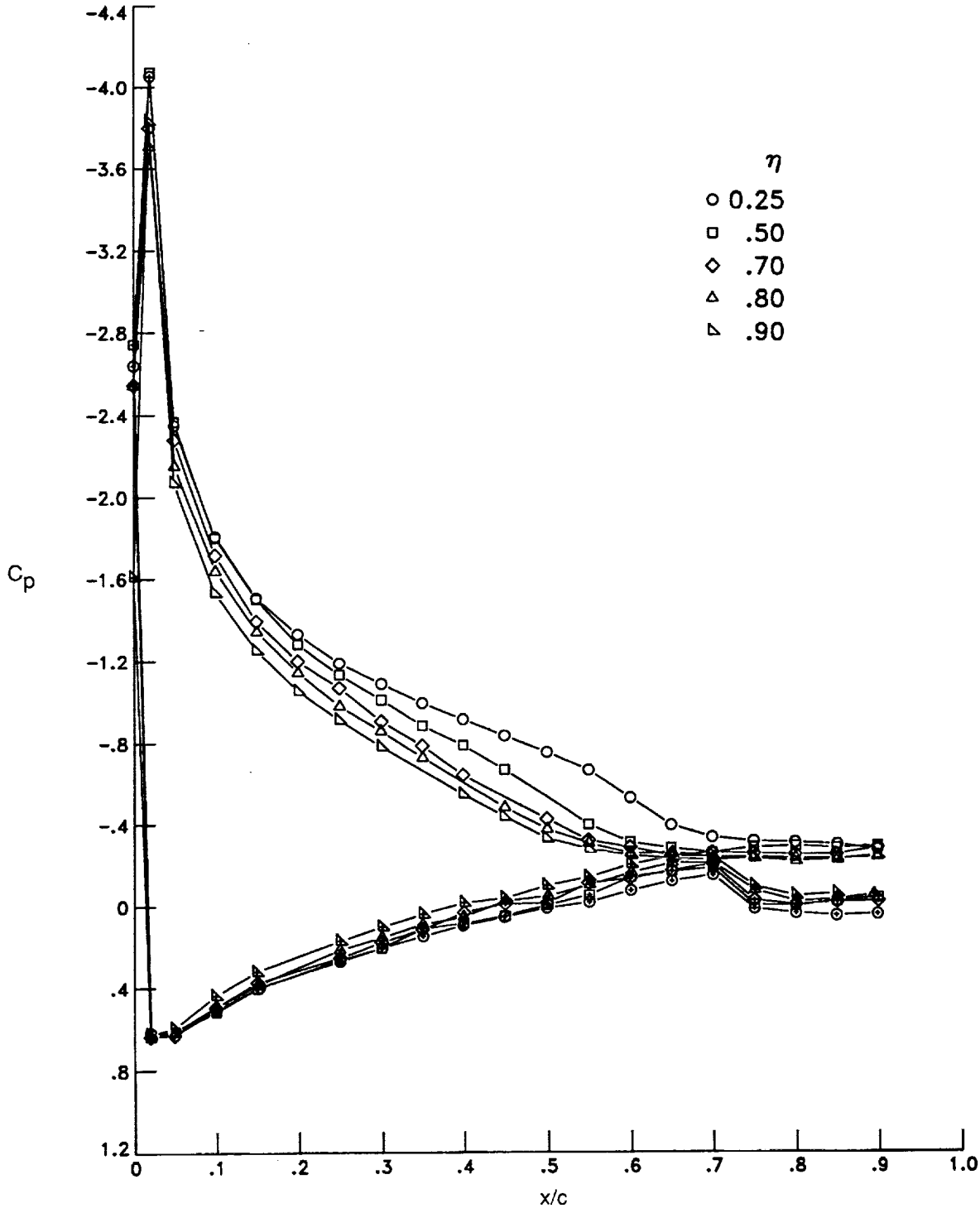

(f) $\alpha = 10°$.

Figure 17. Concluded.

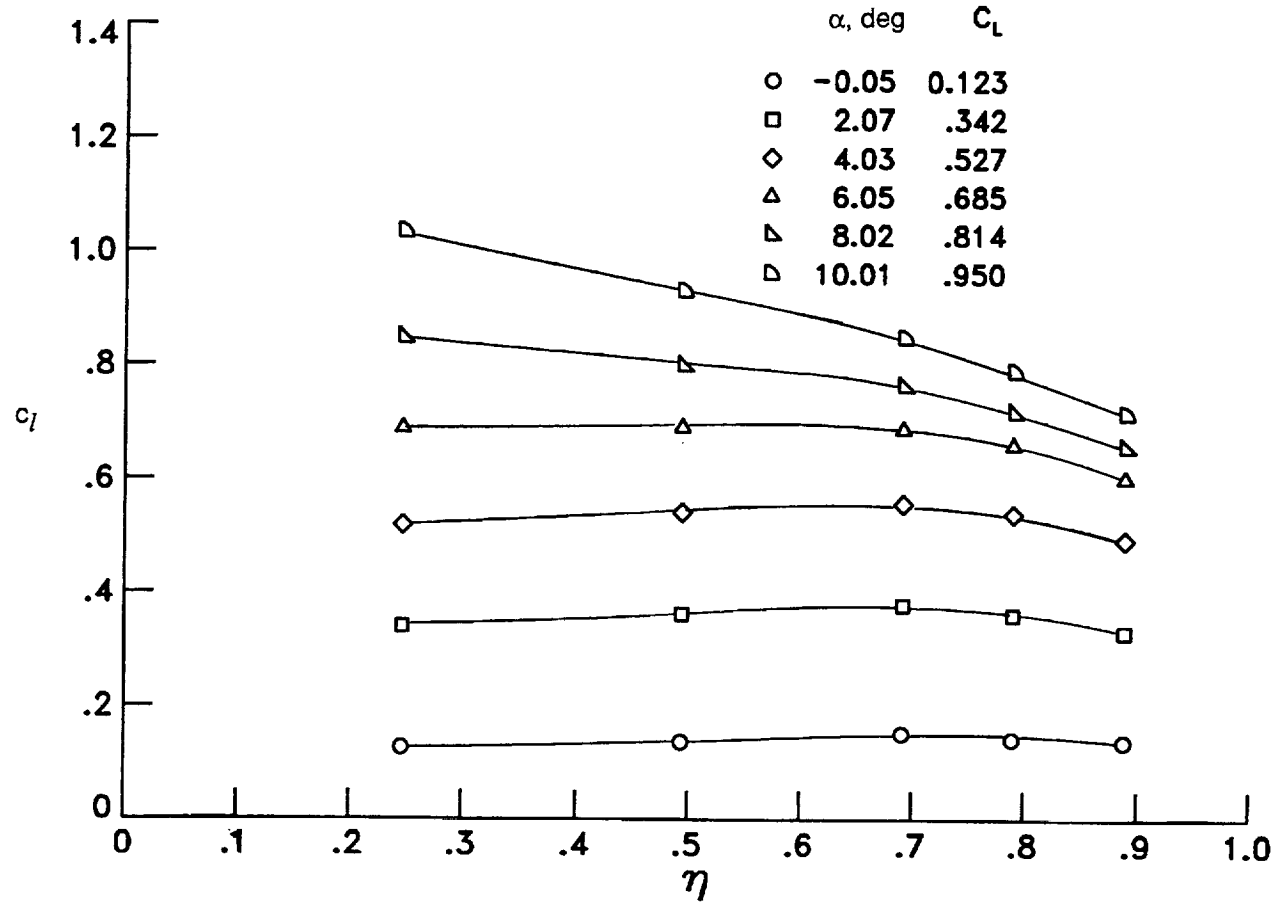

Figure 18. Effect of angle of attack on spanwise variation of section lift coefficient without blowing for tip 8 at $M_\infty = 0.30$.

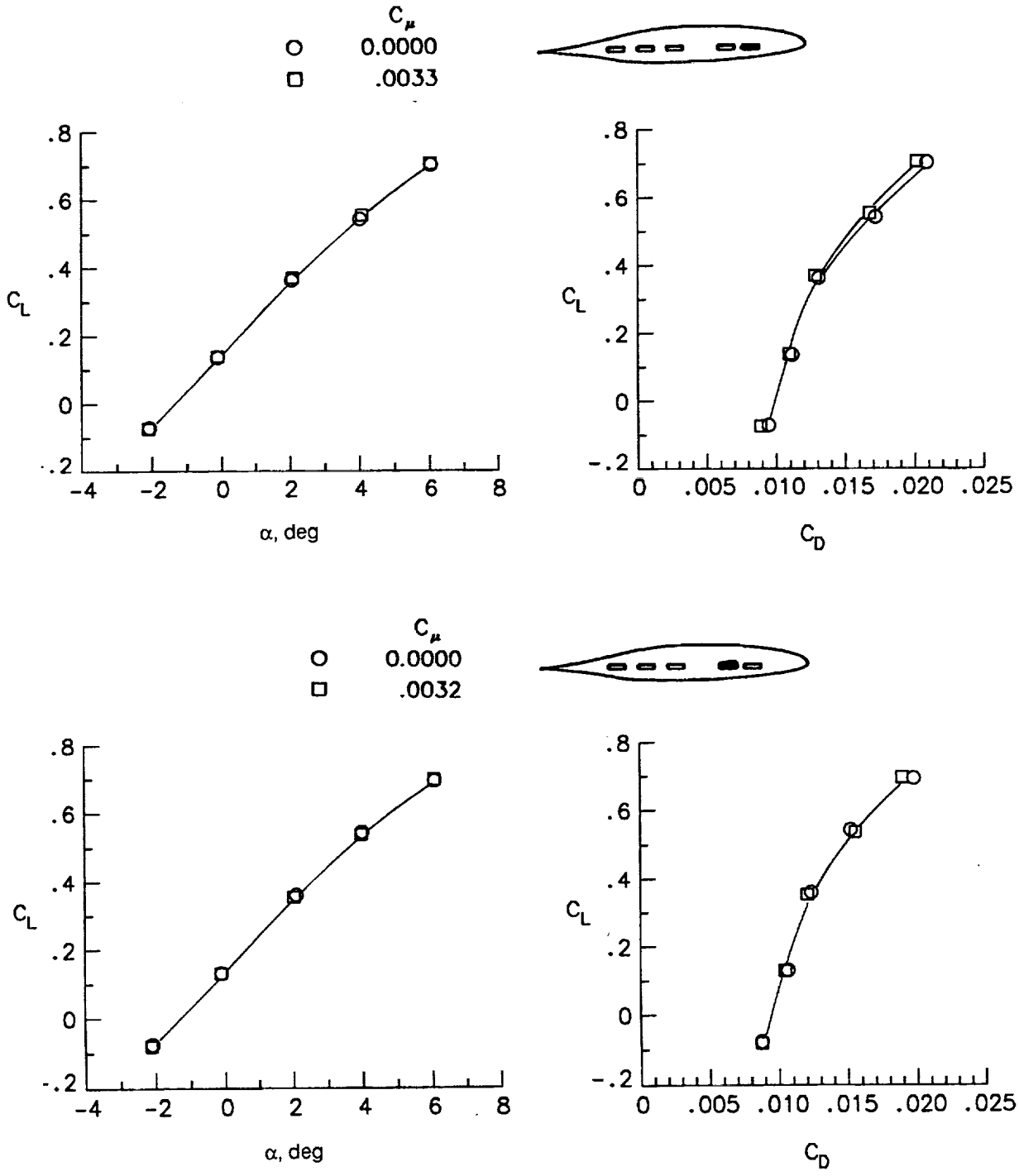

Figure 19. Effect of blowing at various jet chordwise locations on wing lift and drag coefficients at $M_\infty = 0.30$.

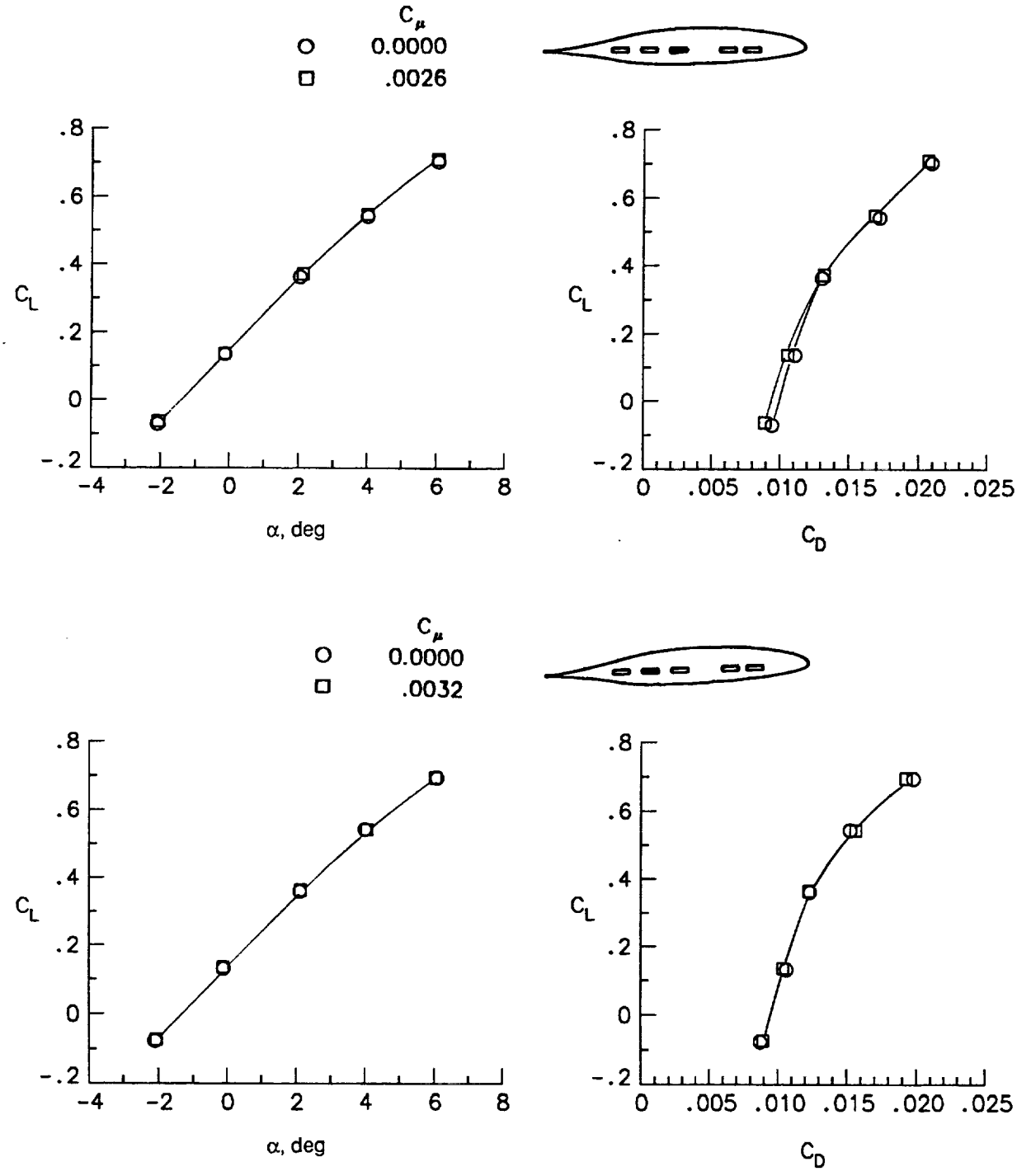

Figure 19. Continued.

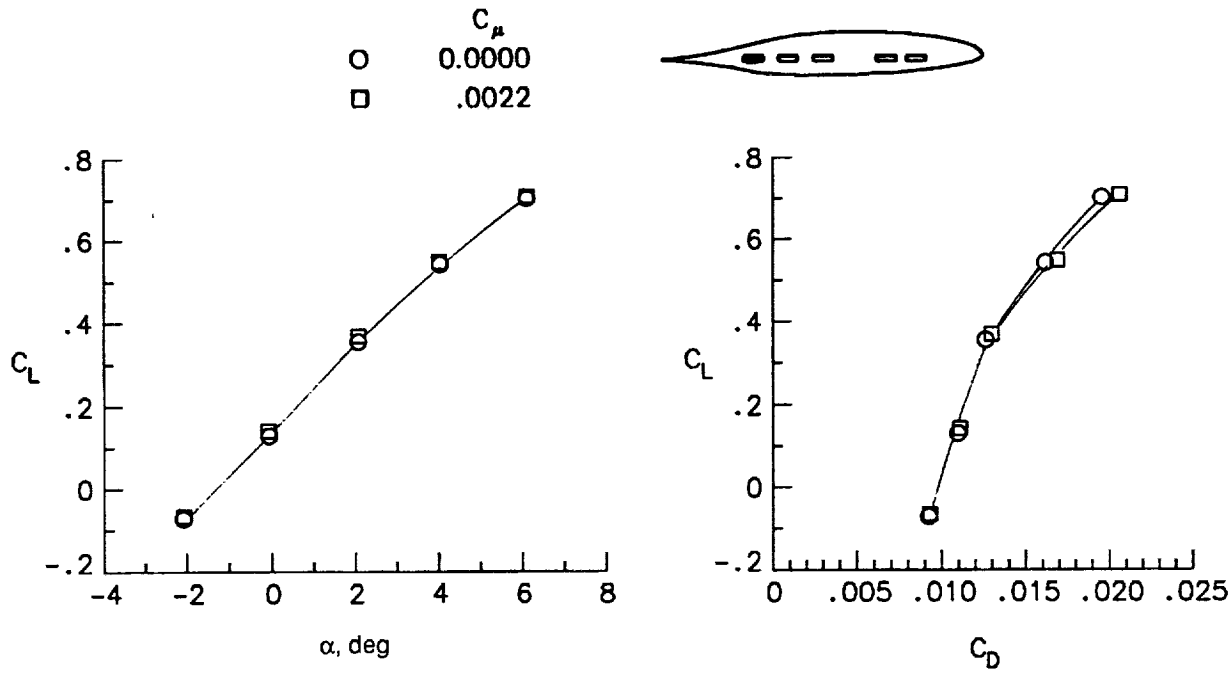

Figure 19. Concluded.

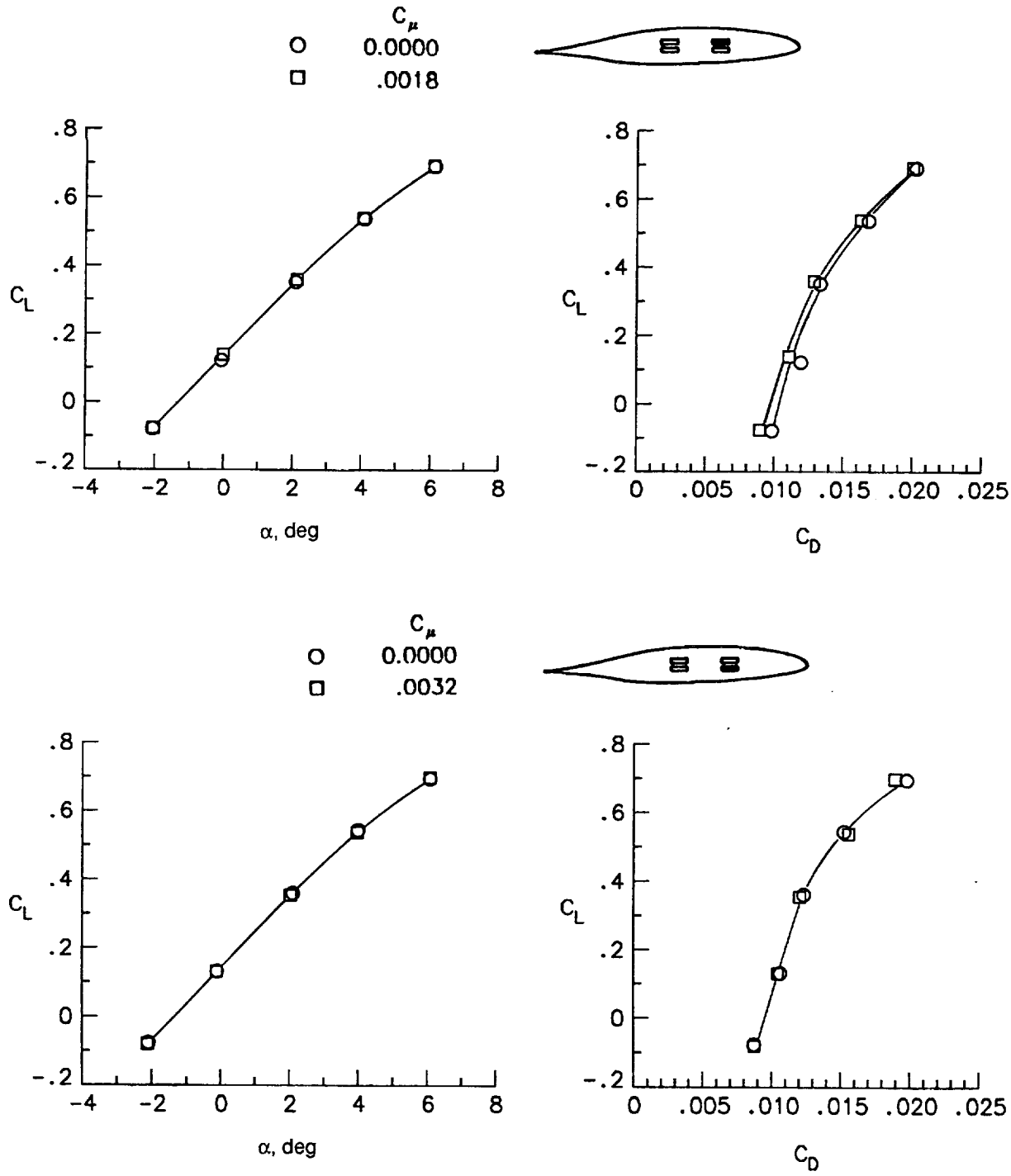

(a) $x_j/c_{tip} = 0.30$.

Figure 20. Effect of blowing at two jet vertical locations on wing lift and drag coefficients at $M_\infty = 0.30$.

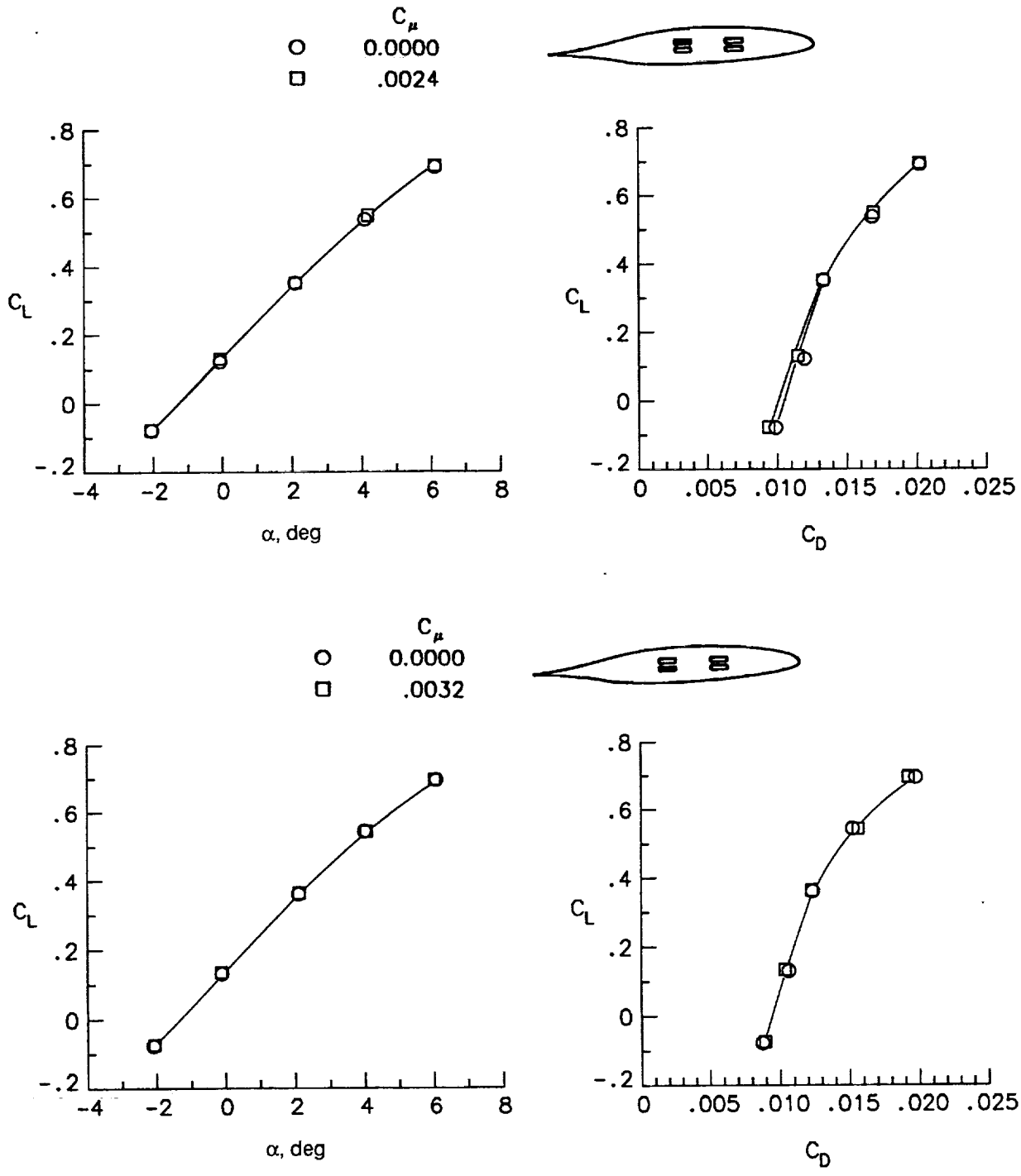

(b) $x_j/c_{tip} = 0.50$.

Figure 20. Concluded.

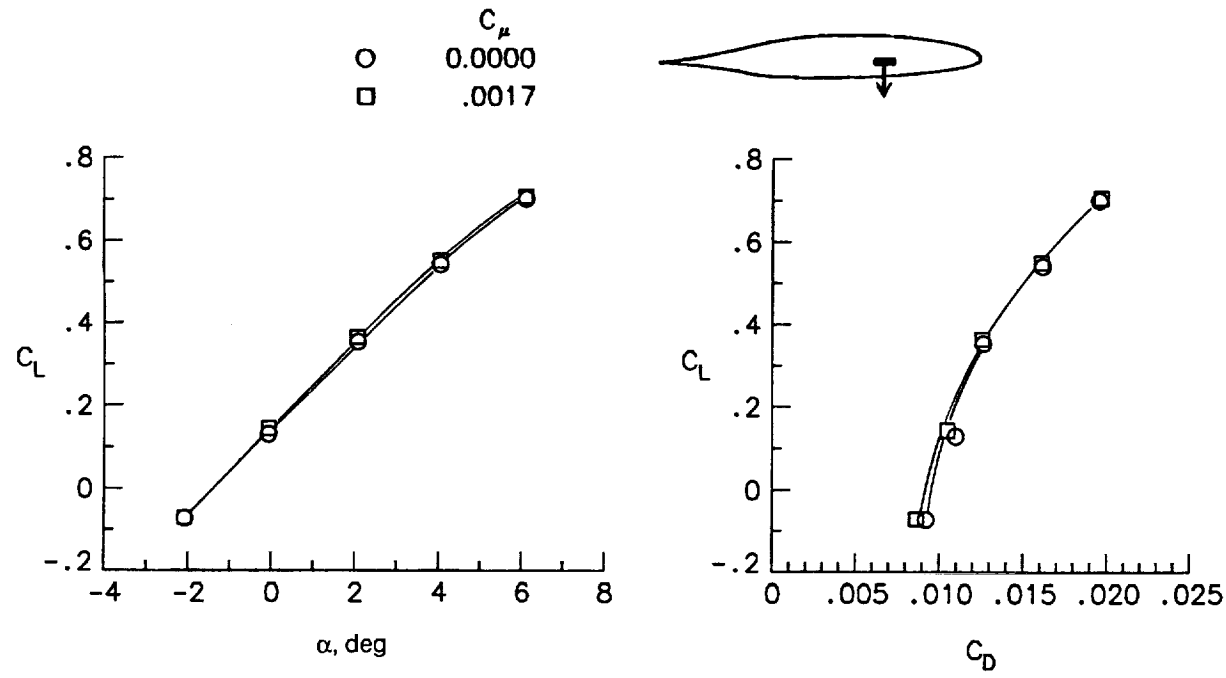

(a) $\delta_j = 20°$.

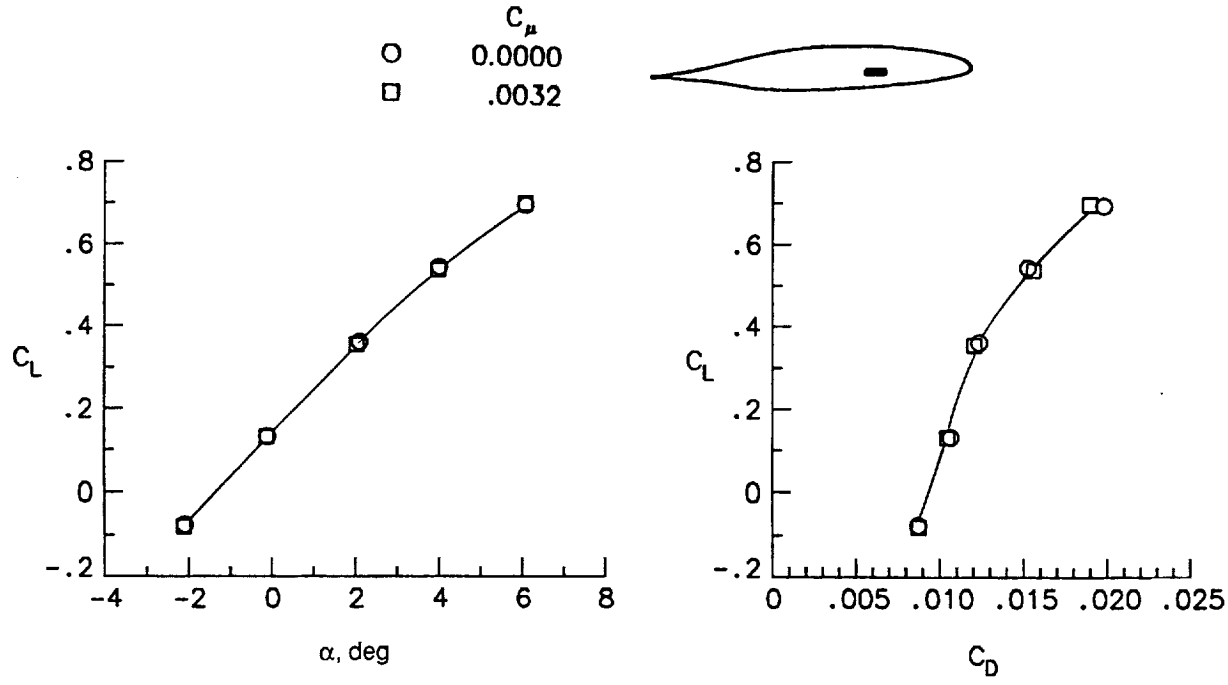

(b) $\delta_j = 0°$.

Figure 21. Effect of redirecting jet exhaust downward on wing lift and drag coefficients at $M_\infty = 0.30$. Jet contributions to lift and drag coefficients have been removed.

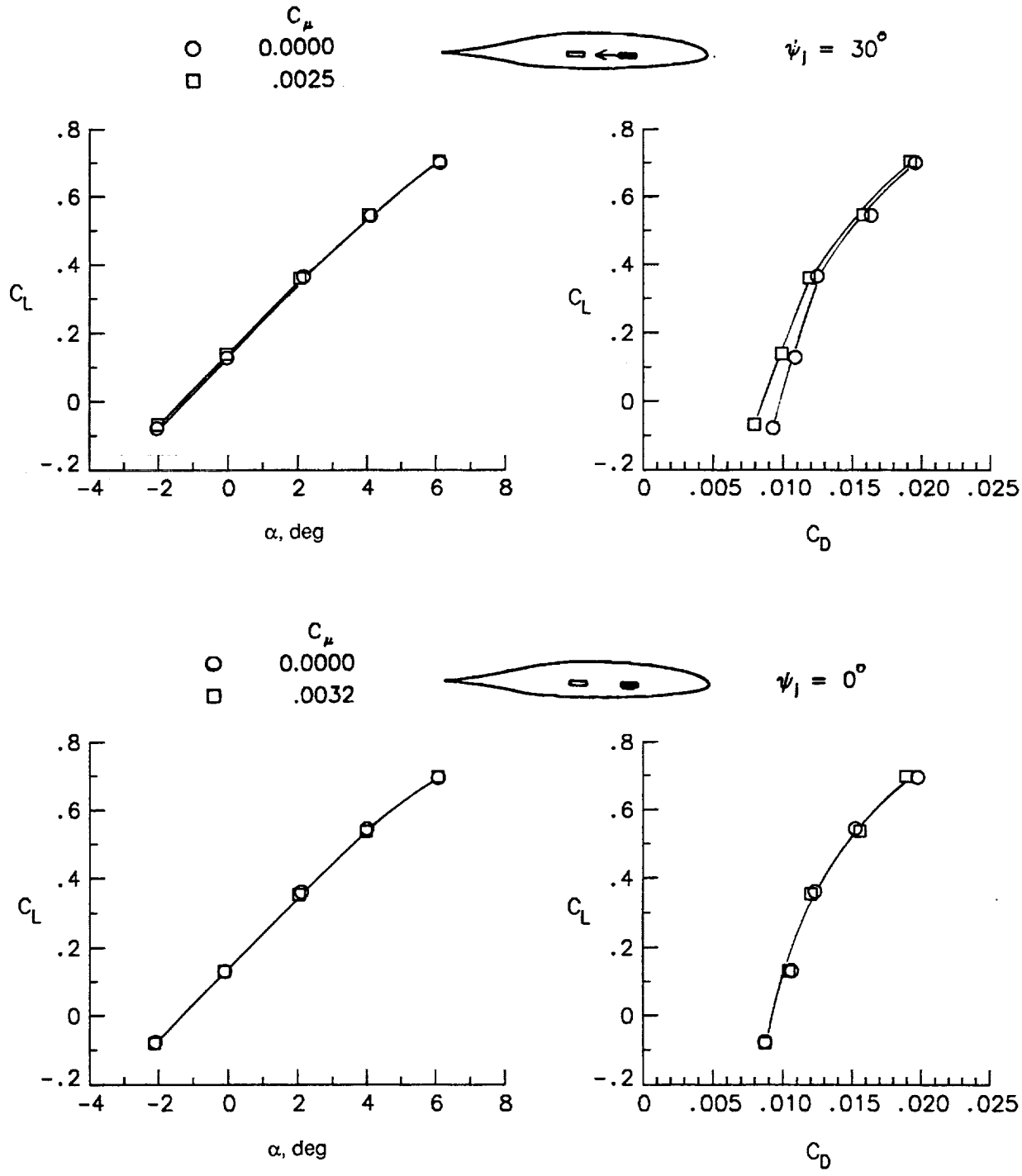

(a) $x_j/c_{tip} = 0.30$.

Figure 22. Effect of redirecting jet blowing downstream on wing lift and drag coefficients with direct thrust effects removed at $M_\infty = 0.30$.

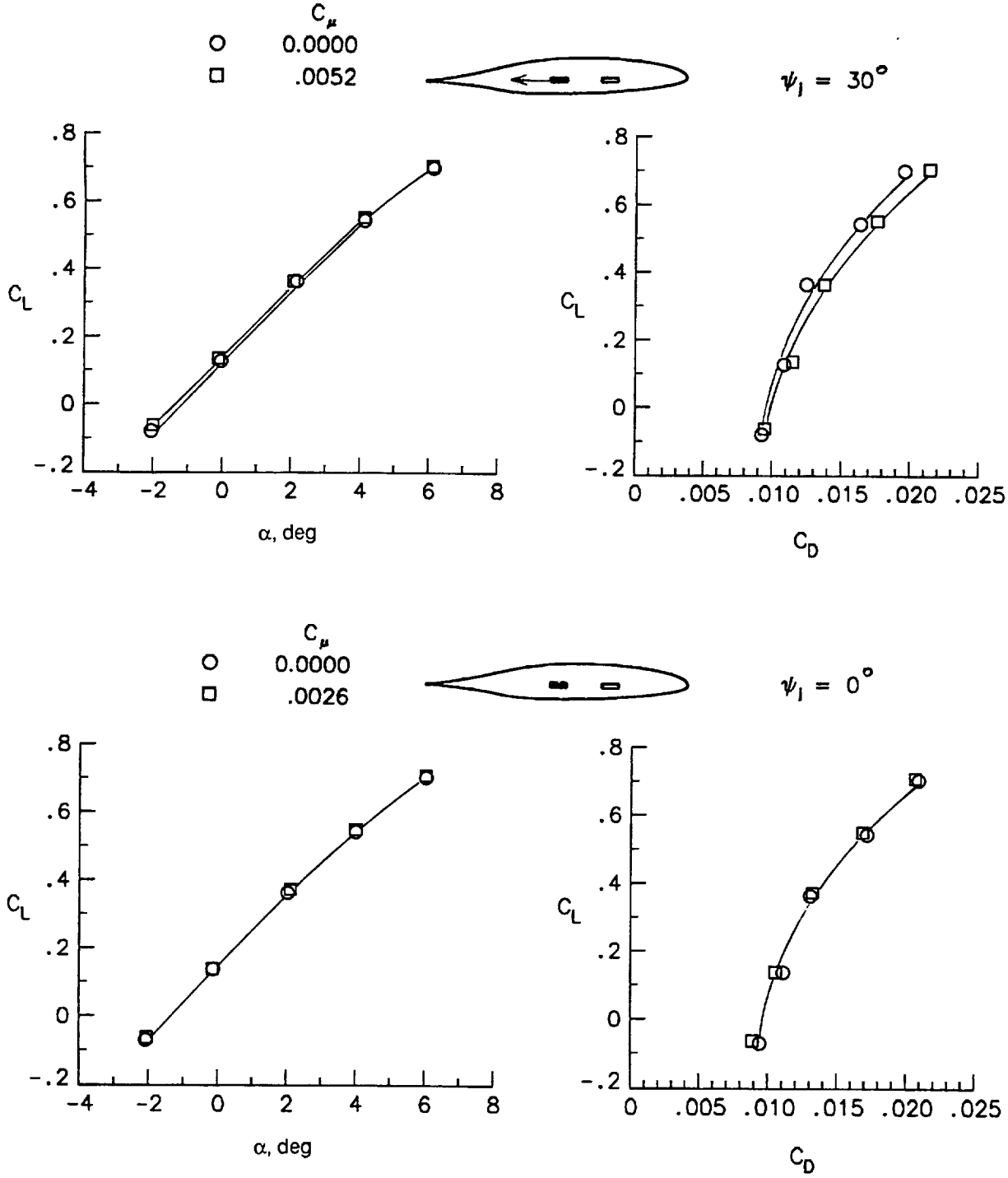

(b) $x_j/c_{tip} = 0.50$.

Figure 22. Concluded.

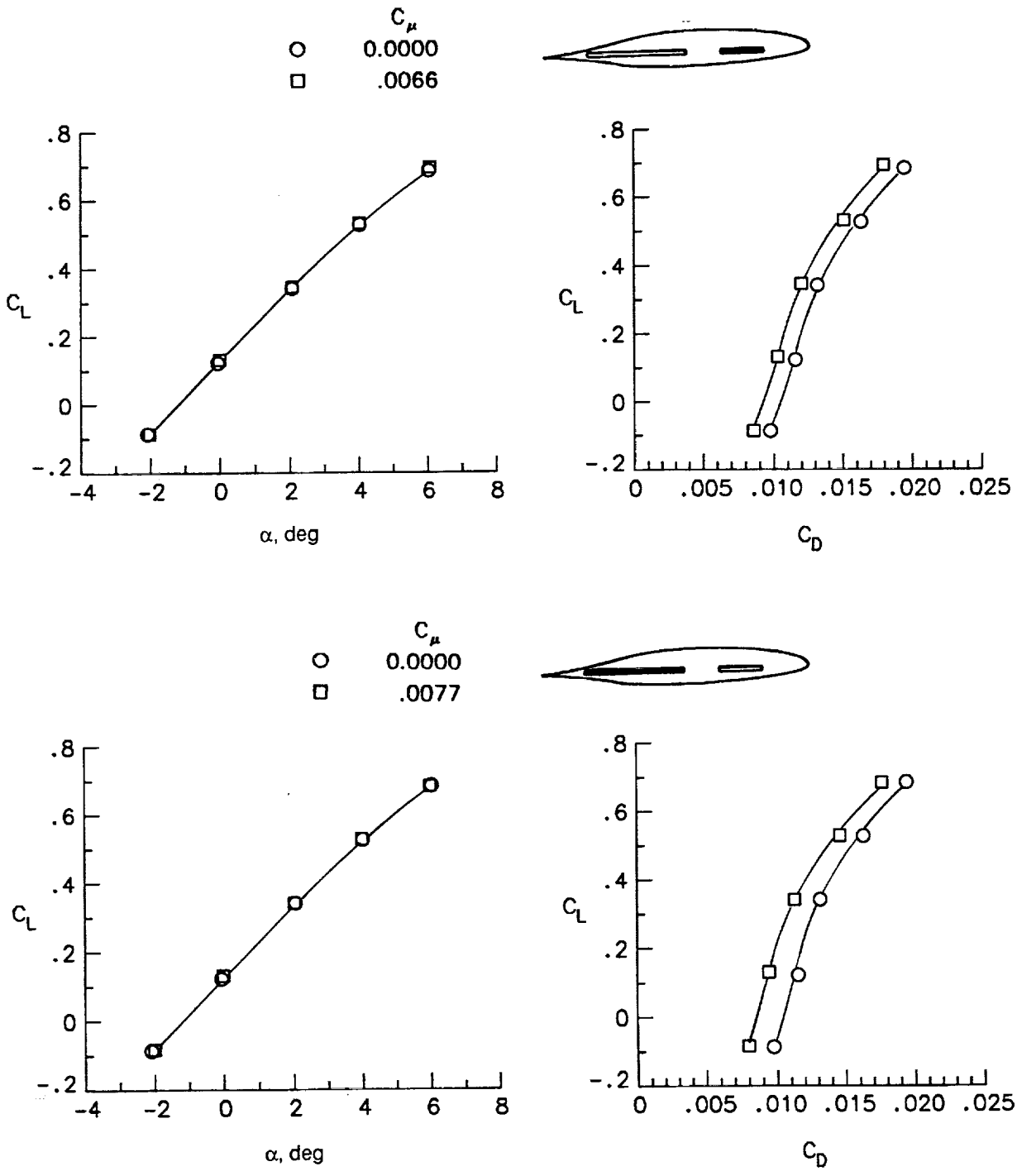

Figure 23. Effect of jet length on wing lift and drag coefficients at $M_\infty = 0.30$.

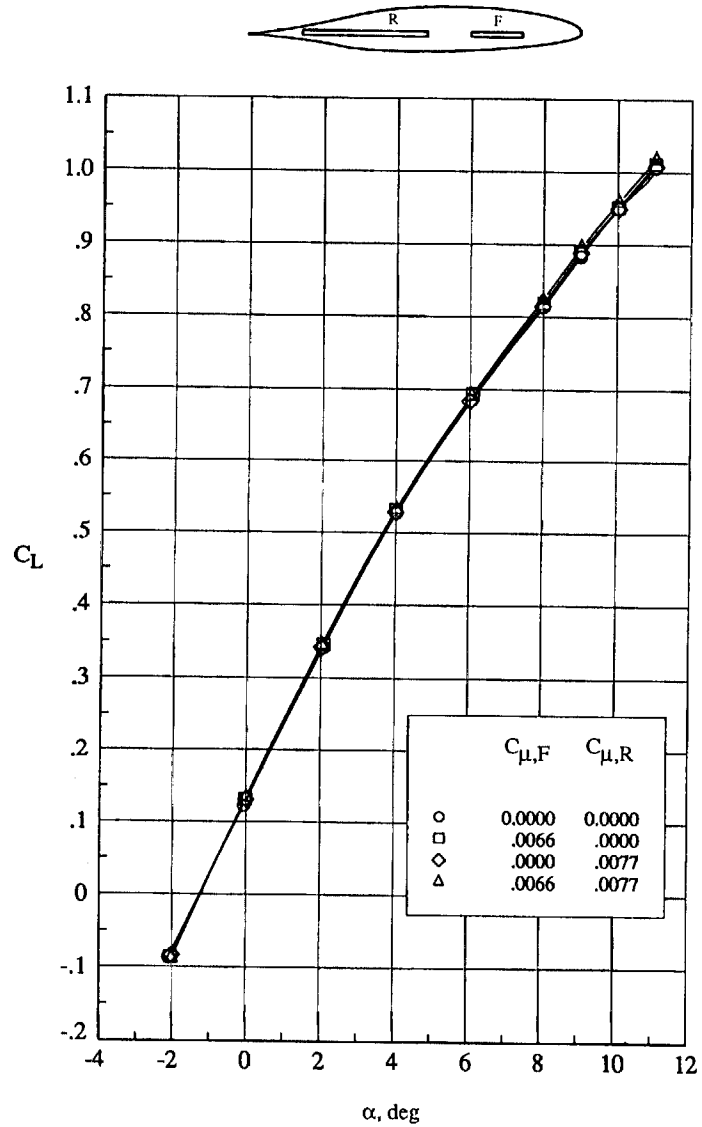

(a) Variation of lift coefficient with angle of attack.

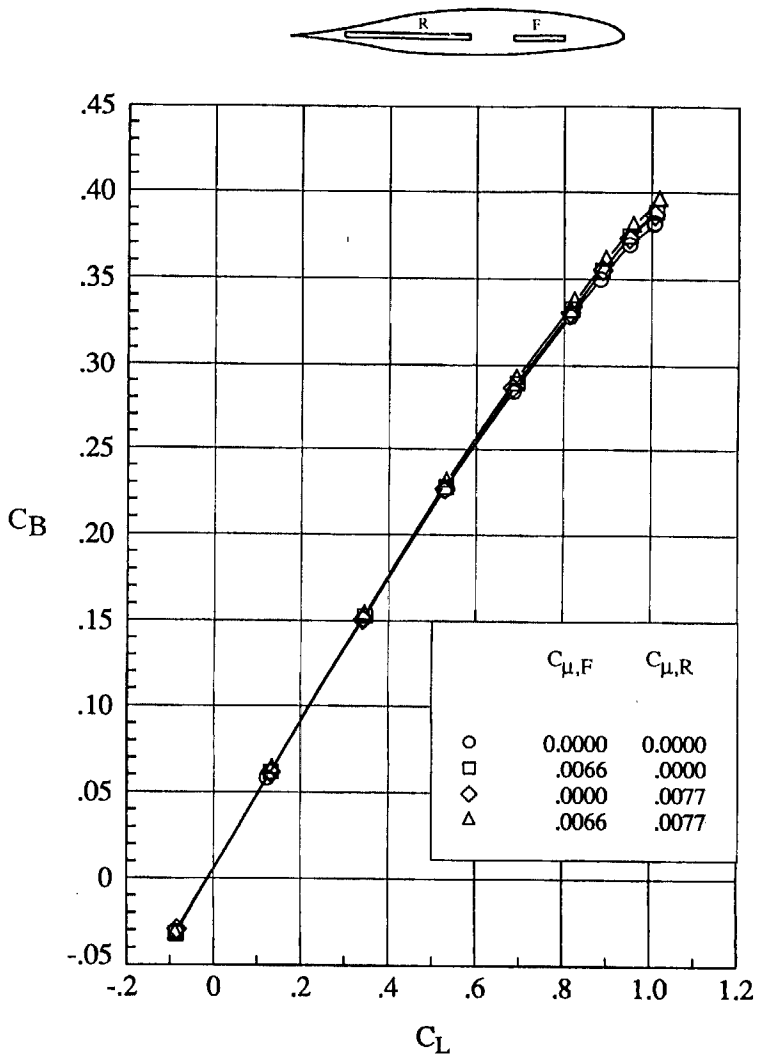

(b) Variation of wing-root bending-moment coefficient with lift coefficient.

Figure 24. Effect of blowing individually and simultaneously from long-chord jets on wing force and moment coefficients for tip 8 at $M_\infty = 0.30$.

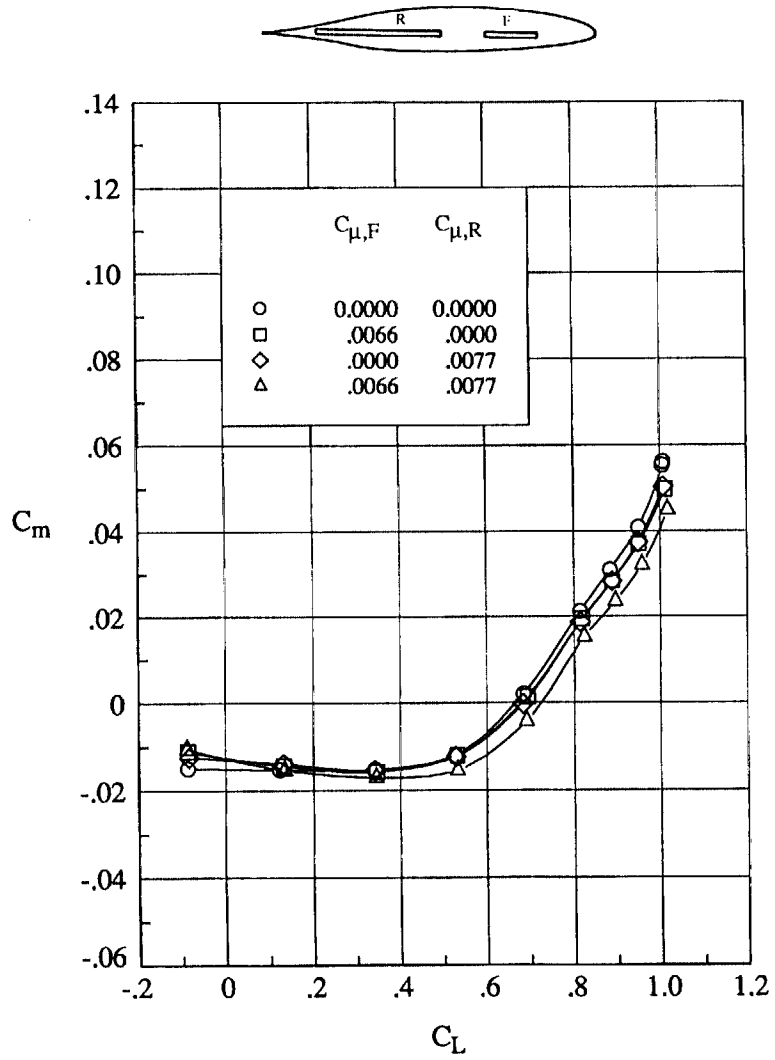

(c) Variation of wing pitching-moment coefficient with lift coefficient.

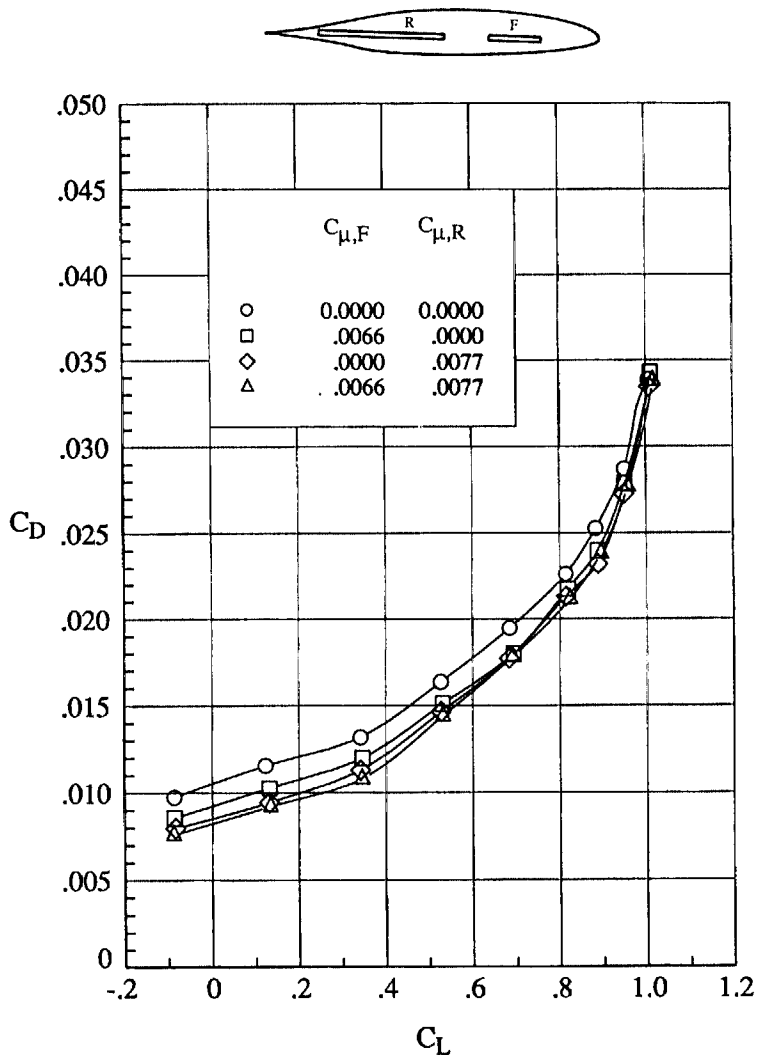

(d) Variation of wing drag coefficient with lift coefficient.

Figure 24. Continued.

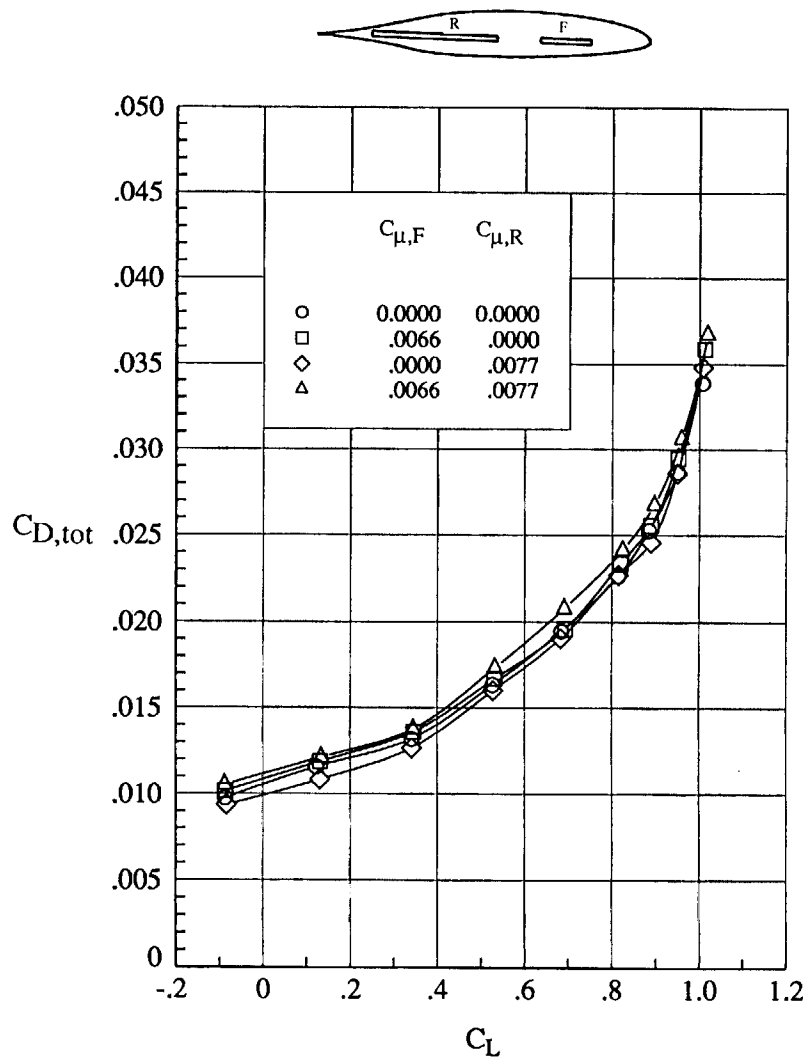

(e) Variation of wing total drag coefficient (including ram drag penalty) with lift coefficient.

Figure 24. Concluded.

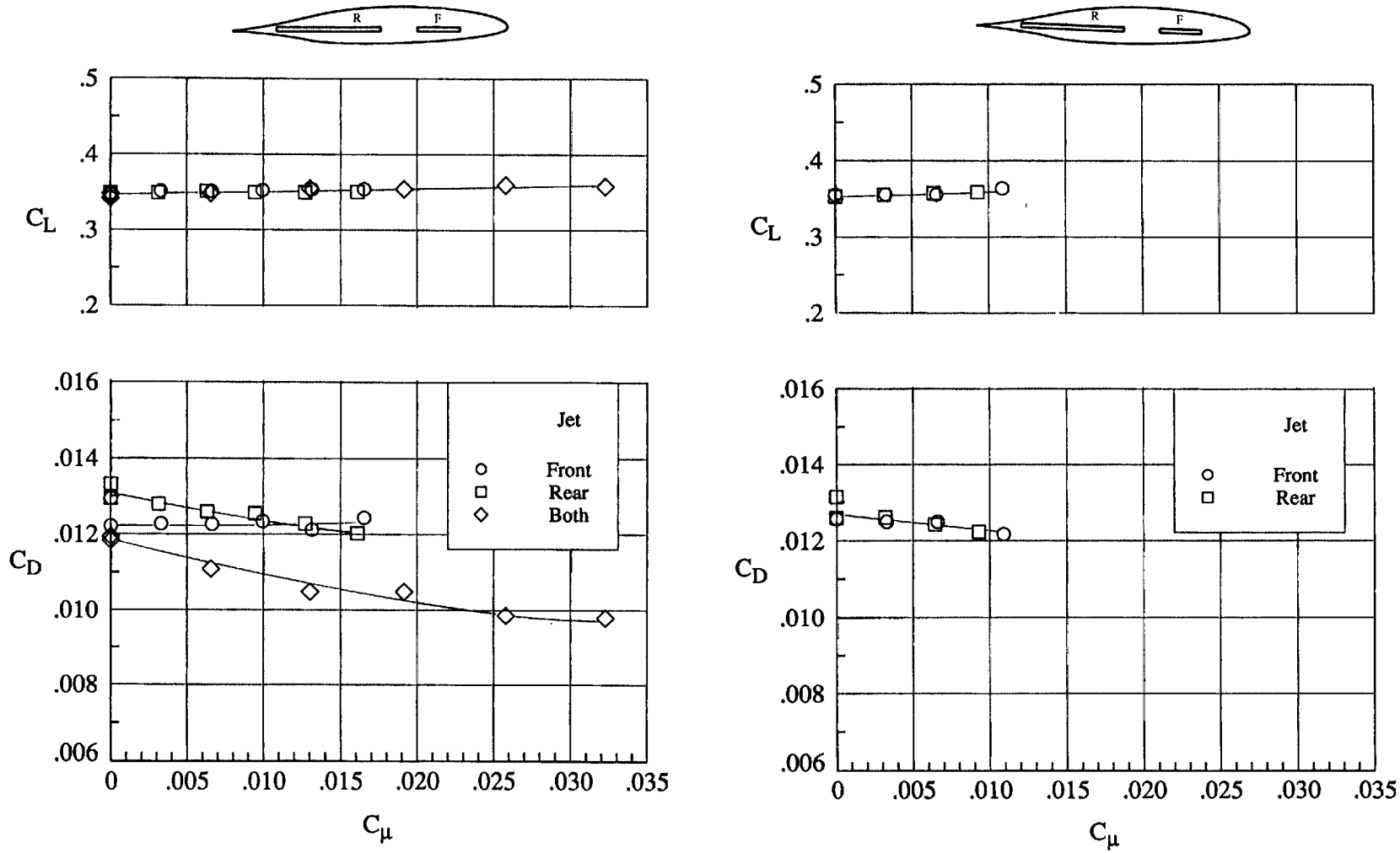

(a) $M_\infty = 0.20$.

(b) $M_\infty = 0.30$.

Figure 25. Variation of wing lift and drag coefficients with jet momentum coefficient for tip 8 at $\alpha = 2.1°$.

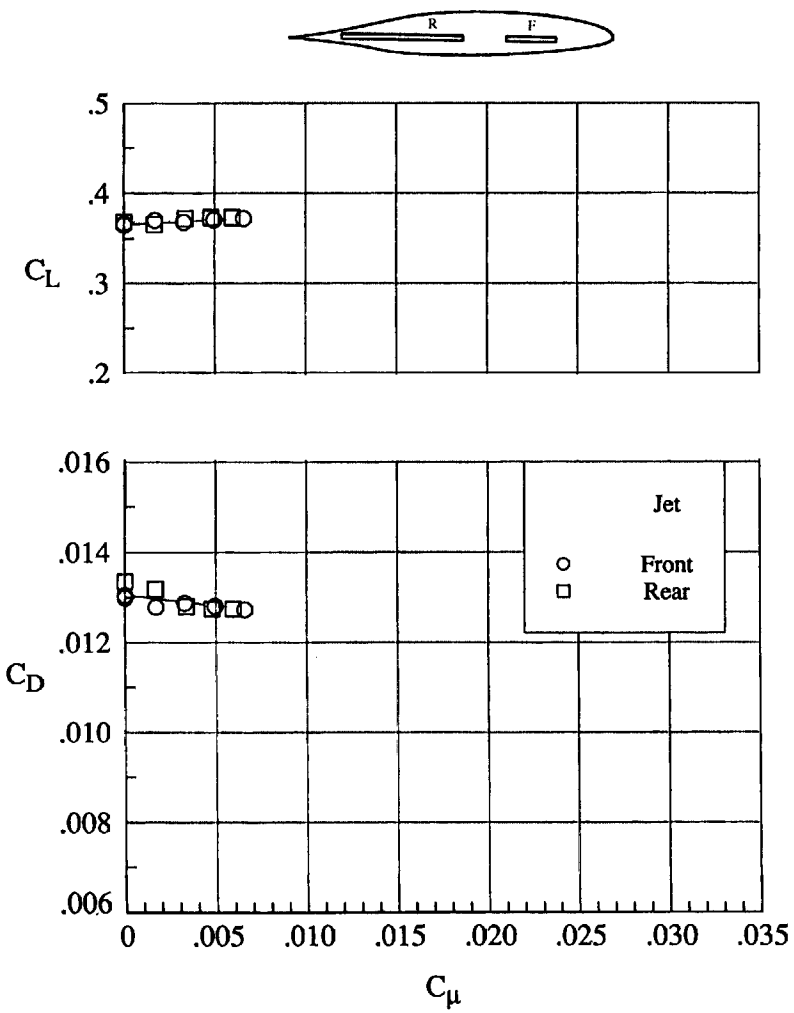

(c) $M_\infty = 0.40$.

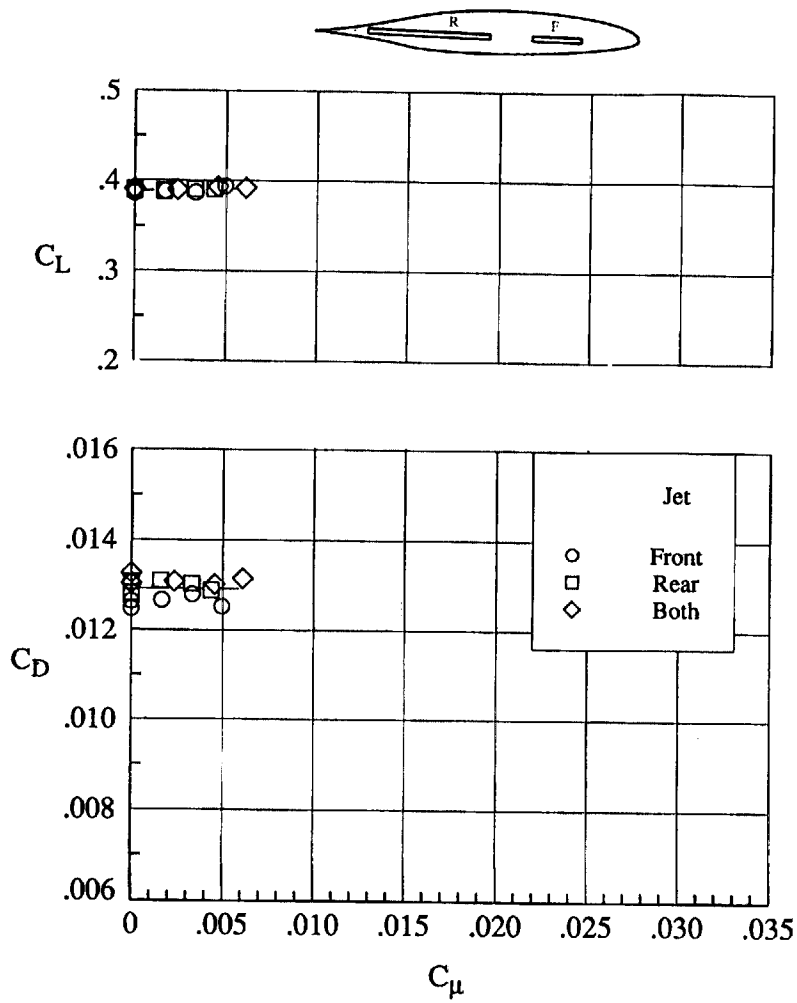

(d) $M_\infty = 0.50$.

Figure 25. Concluded.

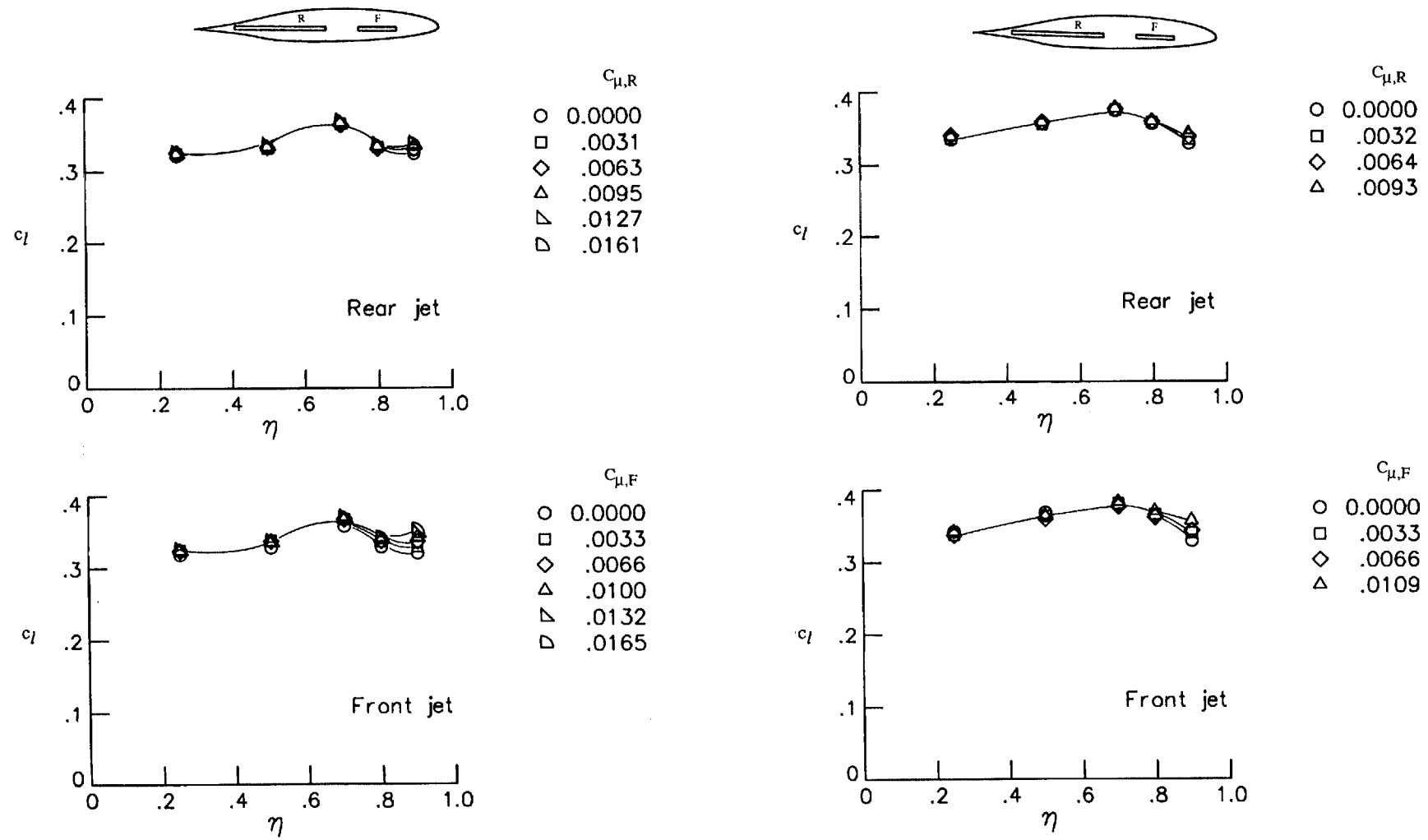

(a) $M_\infty = 0.20$.

(b) $M_\infty = 0.30$.

Figure 26. Effect of blowing on spanwise distribution of section lift coefficient for tip 8 at $\alpha = 2.1°$.

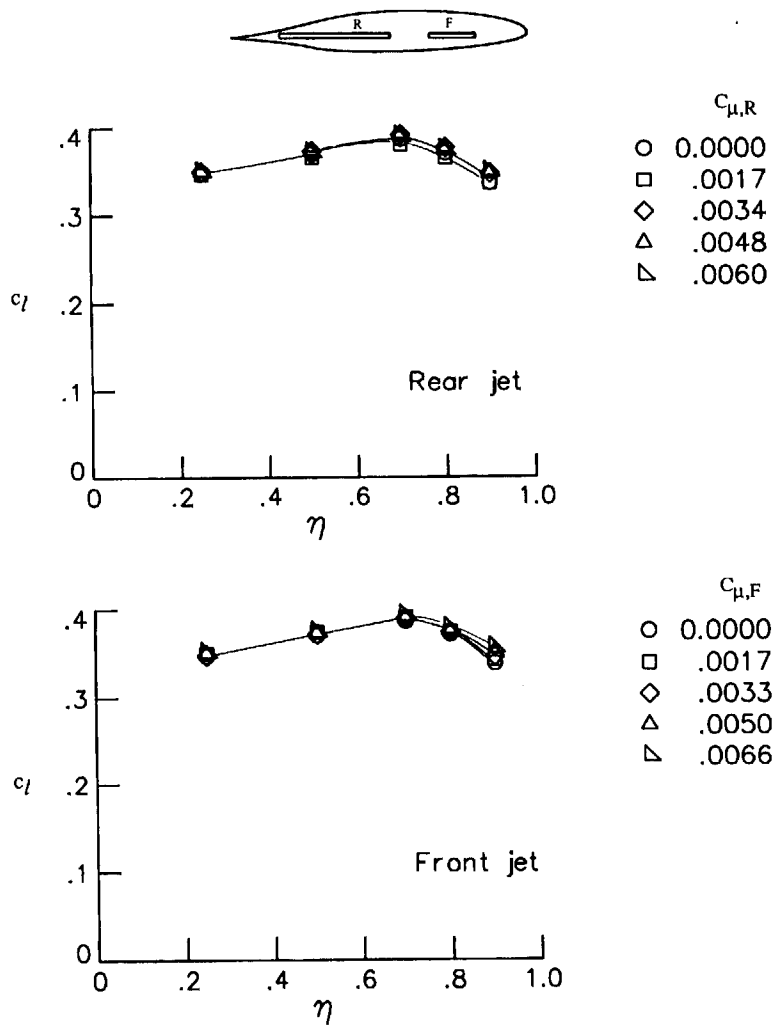

(c) $M_\infty = 0.40$.

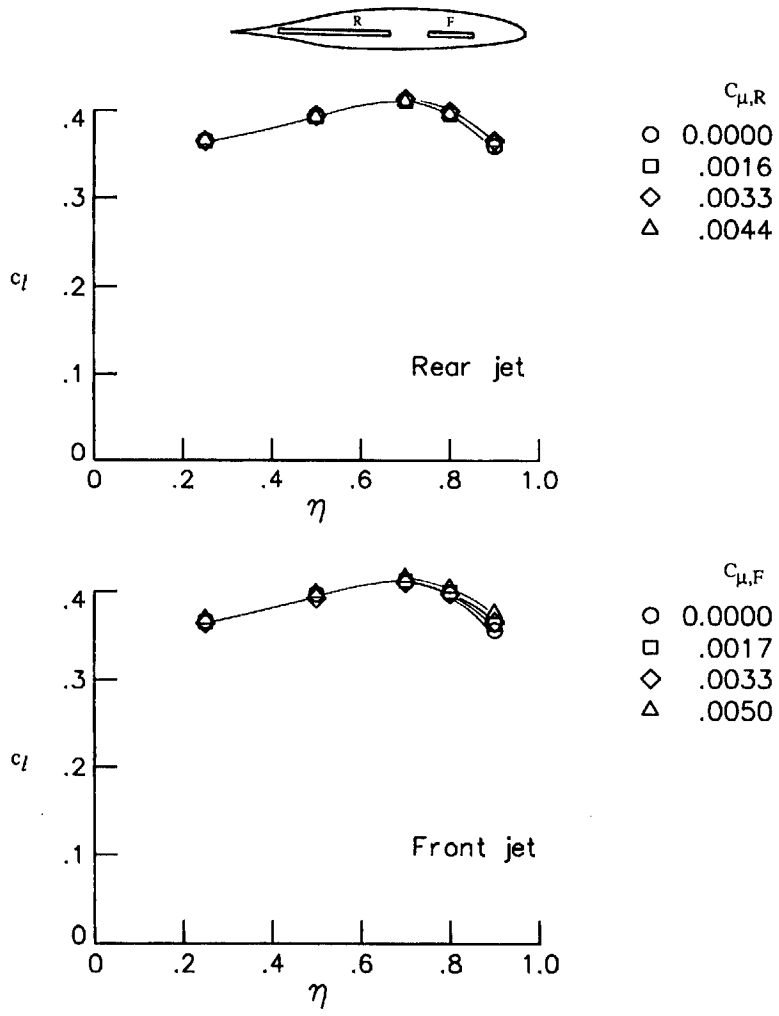

(d) $M_\infty = 0.50$.

Figure 26. Concluded.

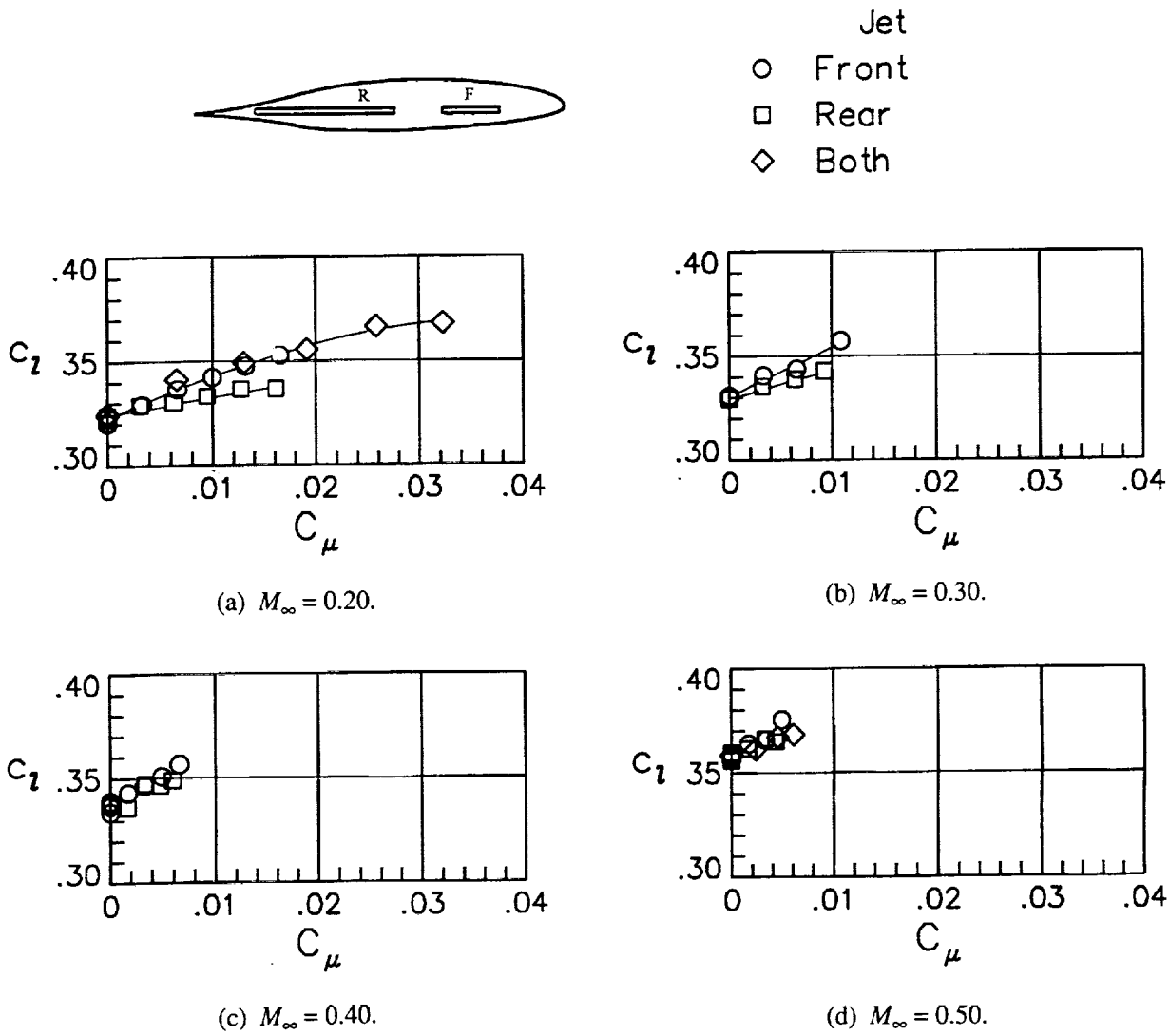

(a) $M_\infty = 0.20$.

(b) $M_\infty = 0.30$.

(c) $M_\infty = 0.40$.

(d) $M_\infty = 0.50$.

Figure 27. Variation of section lift coefficient at $\eta = 0.90$ with jet momentum coefficient for tip 8 at $\alpha = 2.1°$.

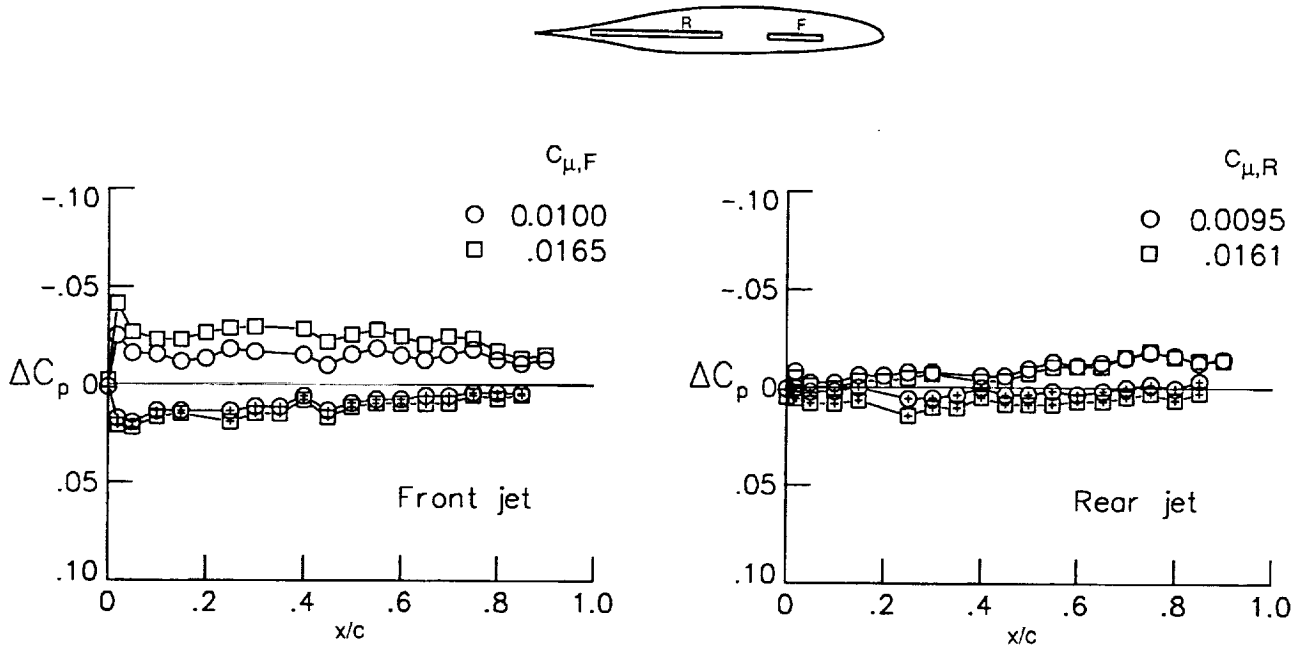

(a) $M_\infty = 0.20$.

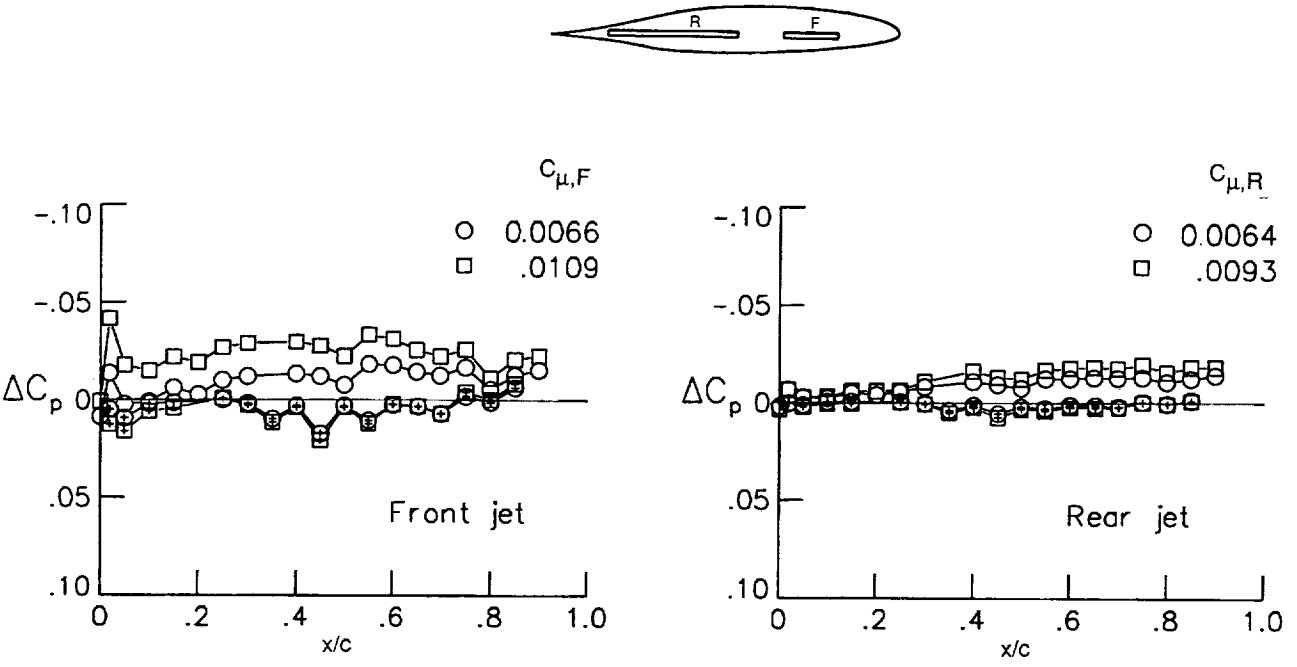

(b) $M_\infty = 0.30$.

Figure 28. Change in local pressure coefficient with blowing at $\eta = 0.90$ for tip 8 at $\alpha = 2.1°$. Symbols with "+" denote lower surface results.

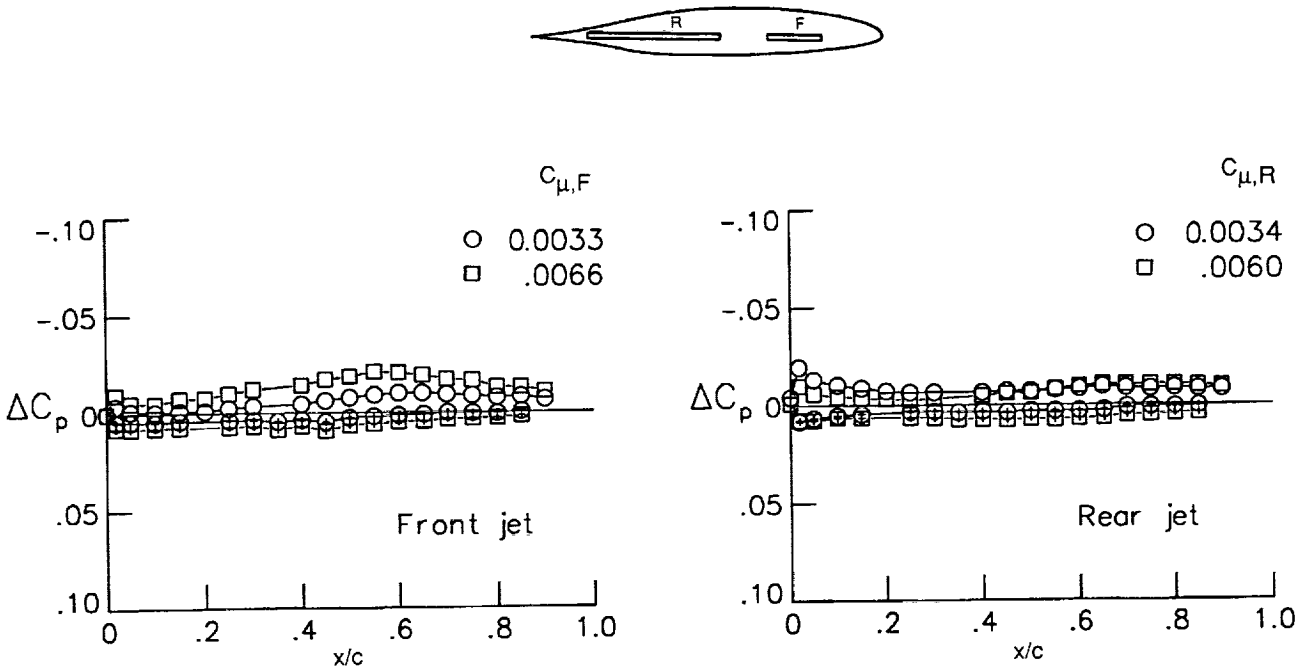

(c) $M_\infty = 0.40$.

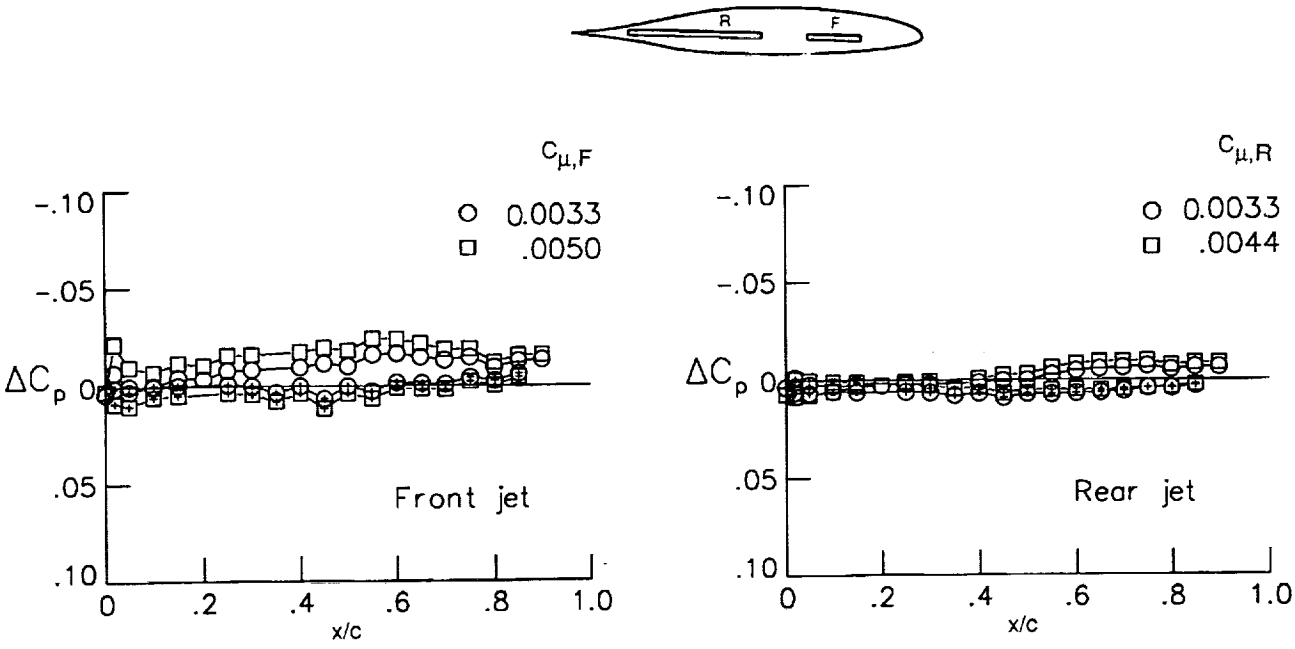

(d) $M_\infty = 0.50$.

Figure 28. Concluded.

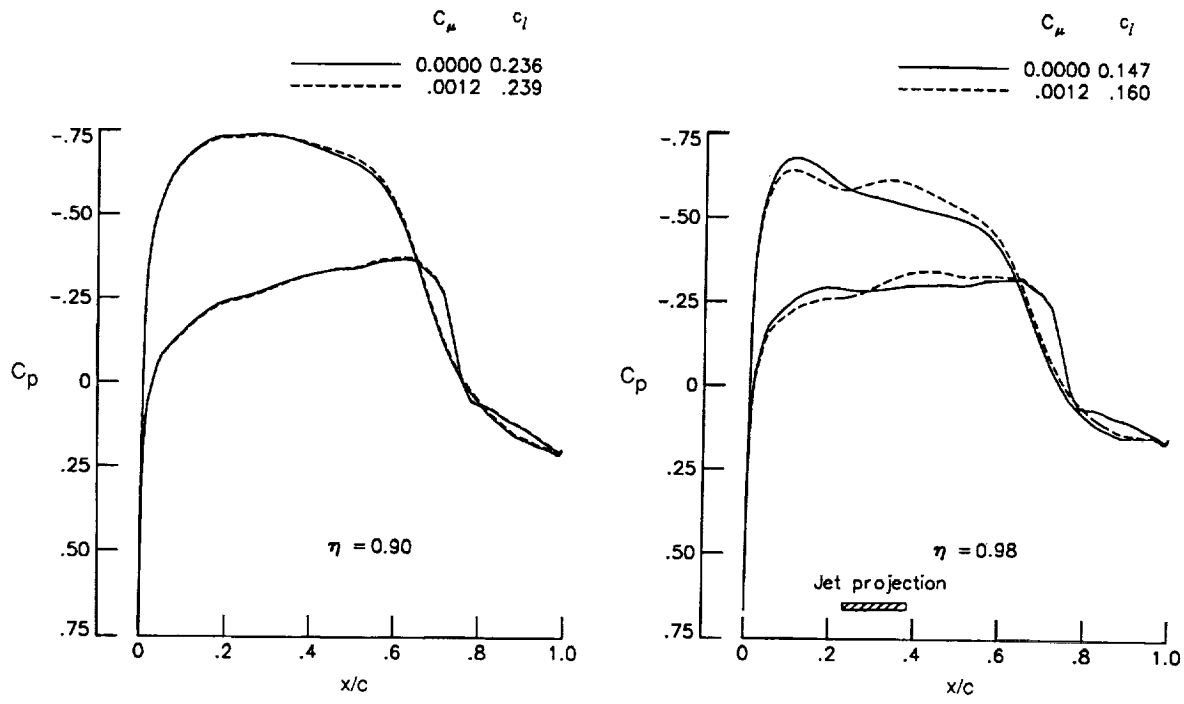

(a) Front jet.

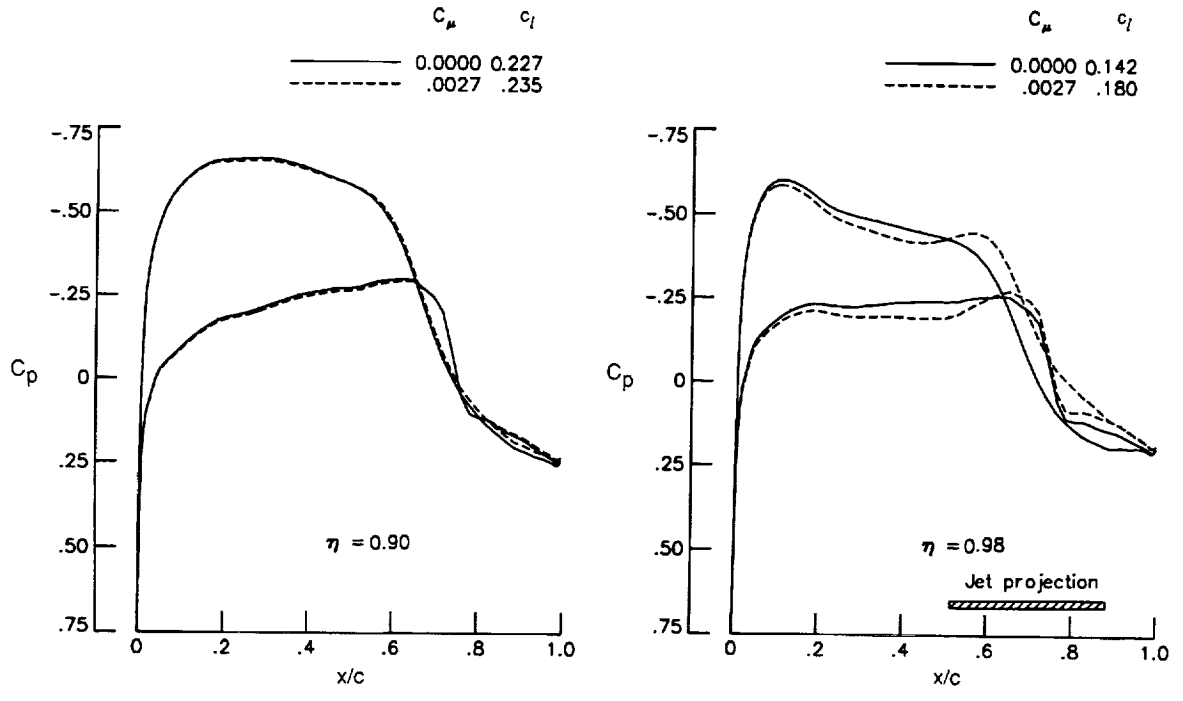

(b) Rear jet.

Figure 29. Computed chordwise pressure distributions near wingtip without and with spanwise blowing at $M_\infty = 0.72$, $\delta_j = 0°$, and $\alpha = 1°$.

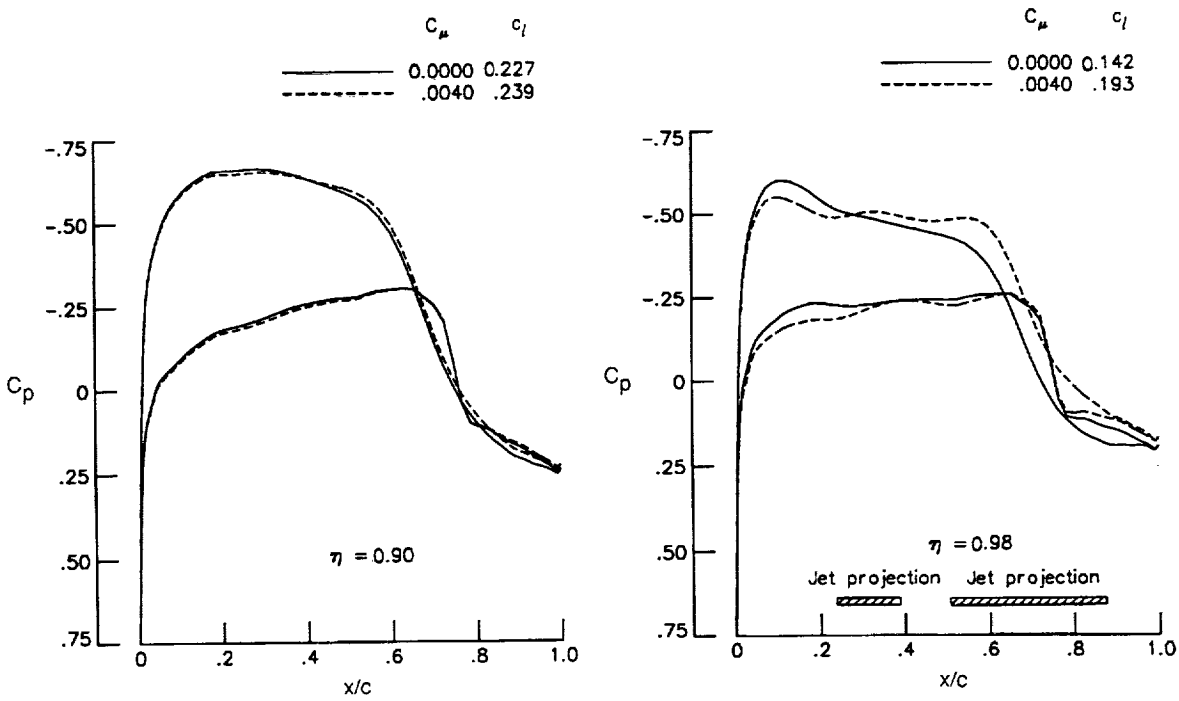

(c) Both jets.

Figure 29. Concluded.

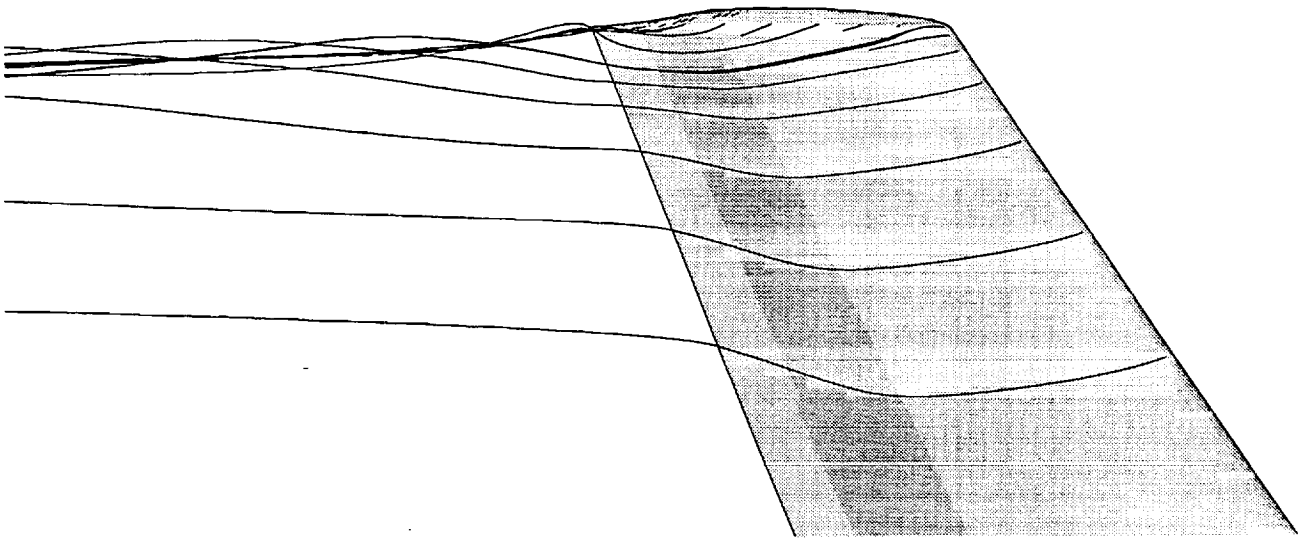

(a) No blowing ($C_\mu = 0$).

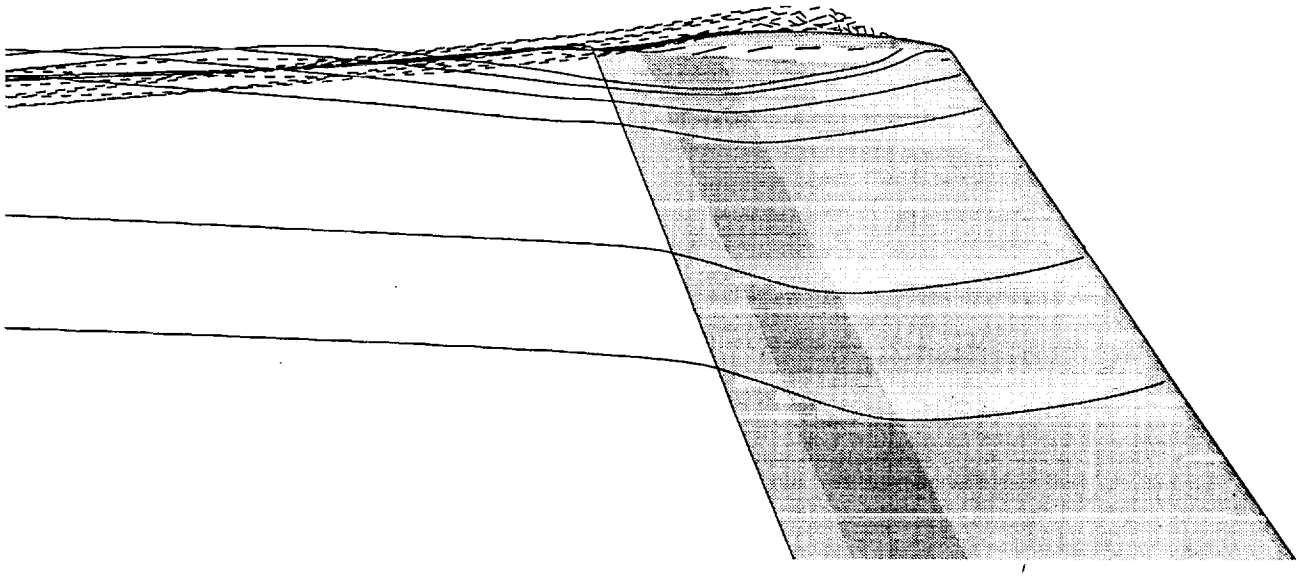

(b) Front jet operating ($C_\mu = 0.0012$).

Figure 30. Computed particle paths on upper surface near wingtip at $M_\infty = 0.72$, $\delta_j = 0°$, and $\alpha = 1°$. Paths starting at jet exit are denoted by dashed lines.

C-2.

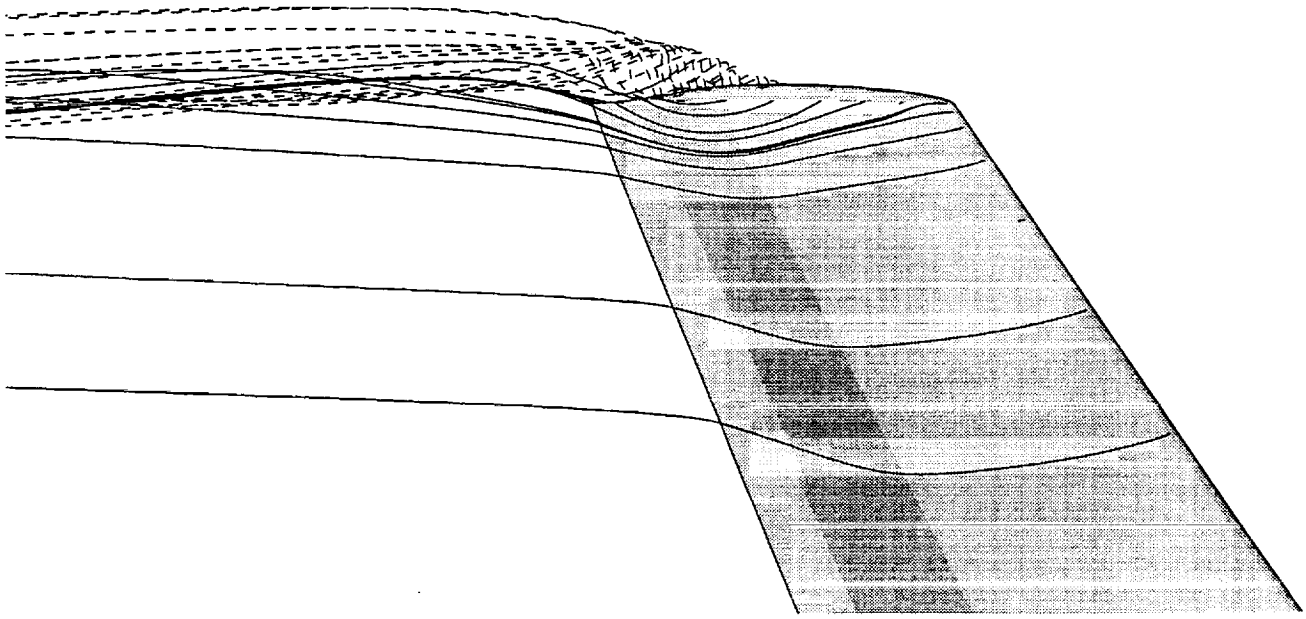

(c) Rear jet operating ($C_\mu = 0.0027$).

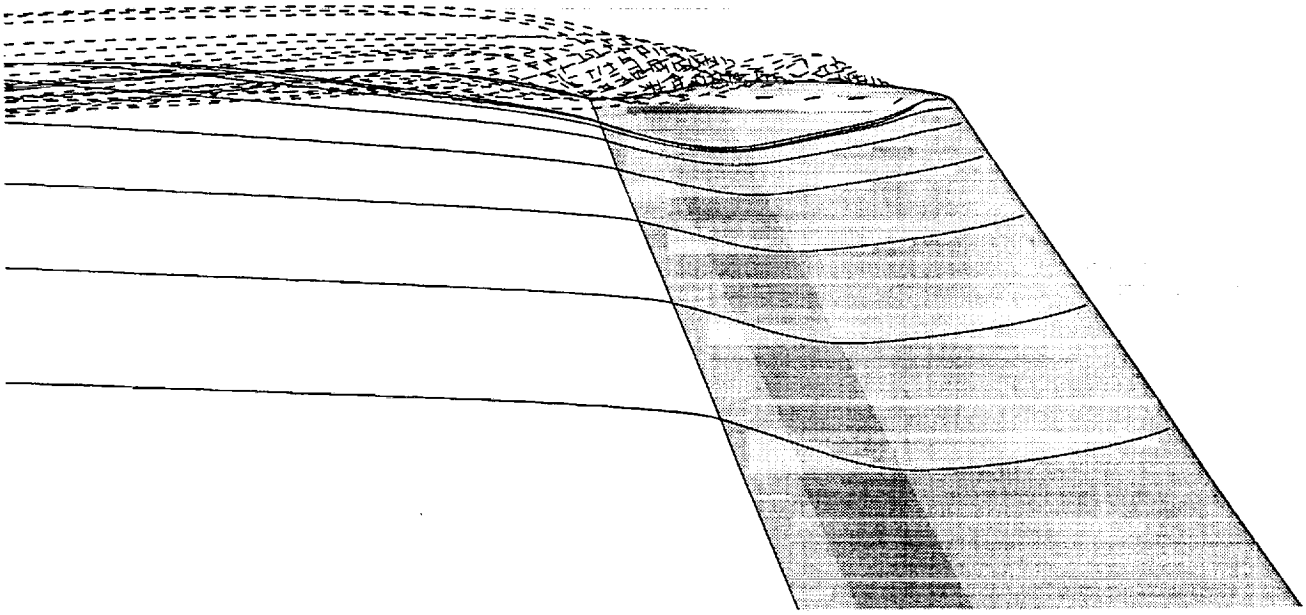

(d) Both jets operating ($C_\mu = 0.0040$).

Figure 30. Concluded.

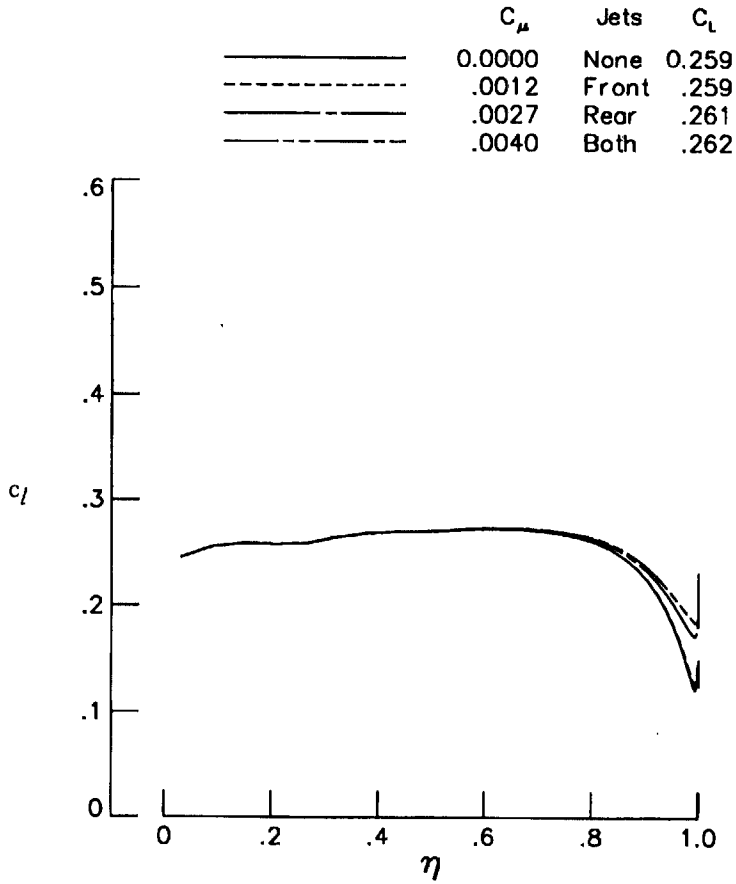

Figure 31. Computed spanwise variation of section lift coefficient for different jet blowing configurations at $M_\infty = 0.72$, $\delta_j = 0°$, and $\alpha = 1°$.

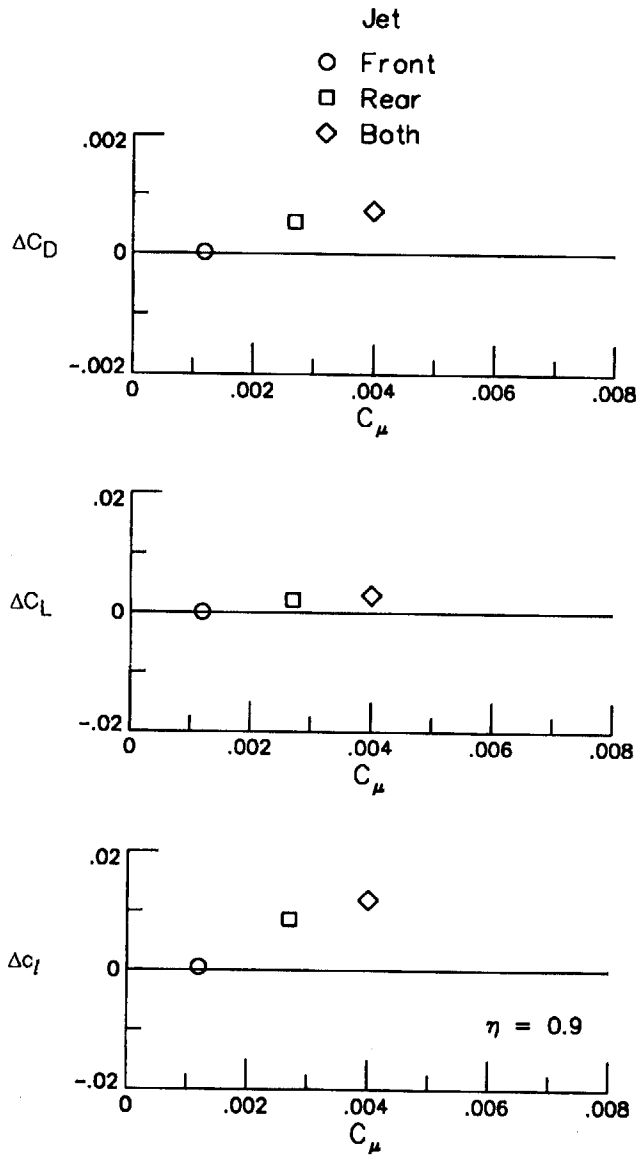

Figure 32. Computed changes in section wing lift coefficient at $\eta = 0.90$, wing lift, and wing drag coefficients due to blowing at $M_\infty = 0.72$, $\delta_j = 0°$, and $\alpha = 1°$.

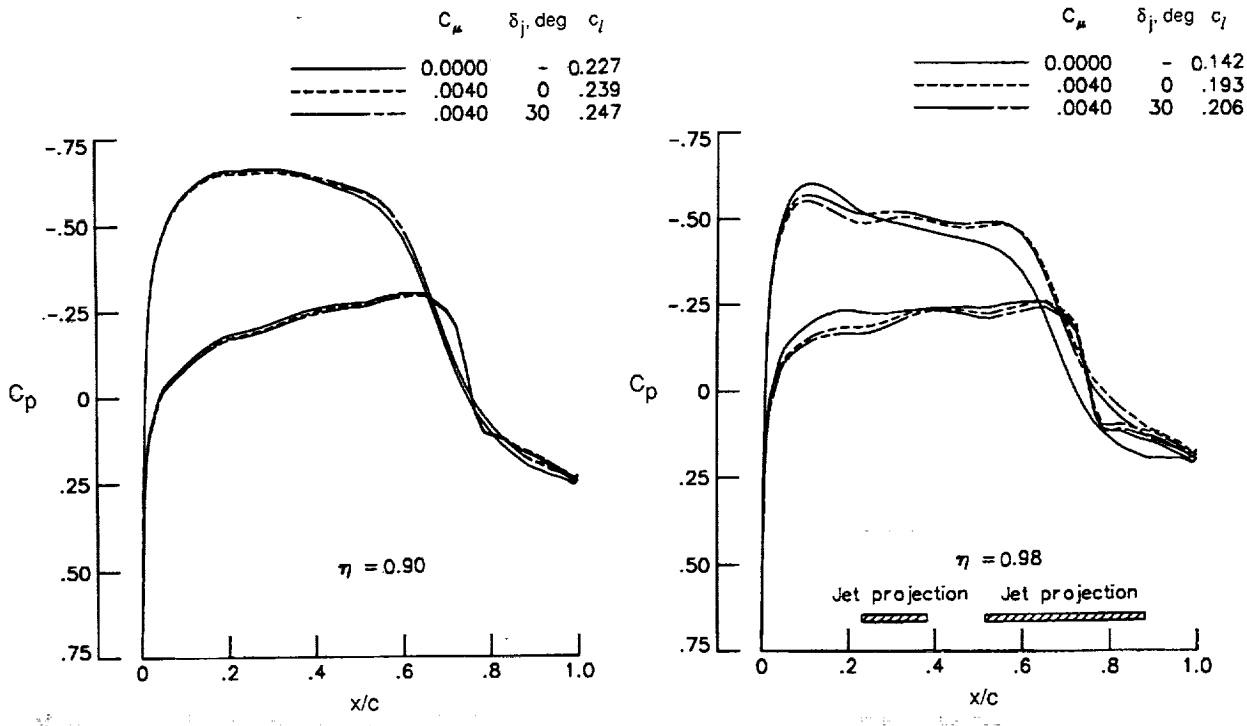

Figure 33. Computed chordwise pressure distribution near wingtip with blowing from both jets at two jet deflection angles compared with no-blowing case at $M_\infty = 0.72$ and $\alpha = 1°$.

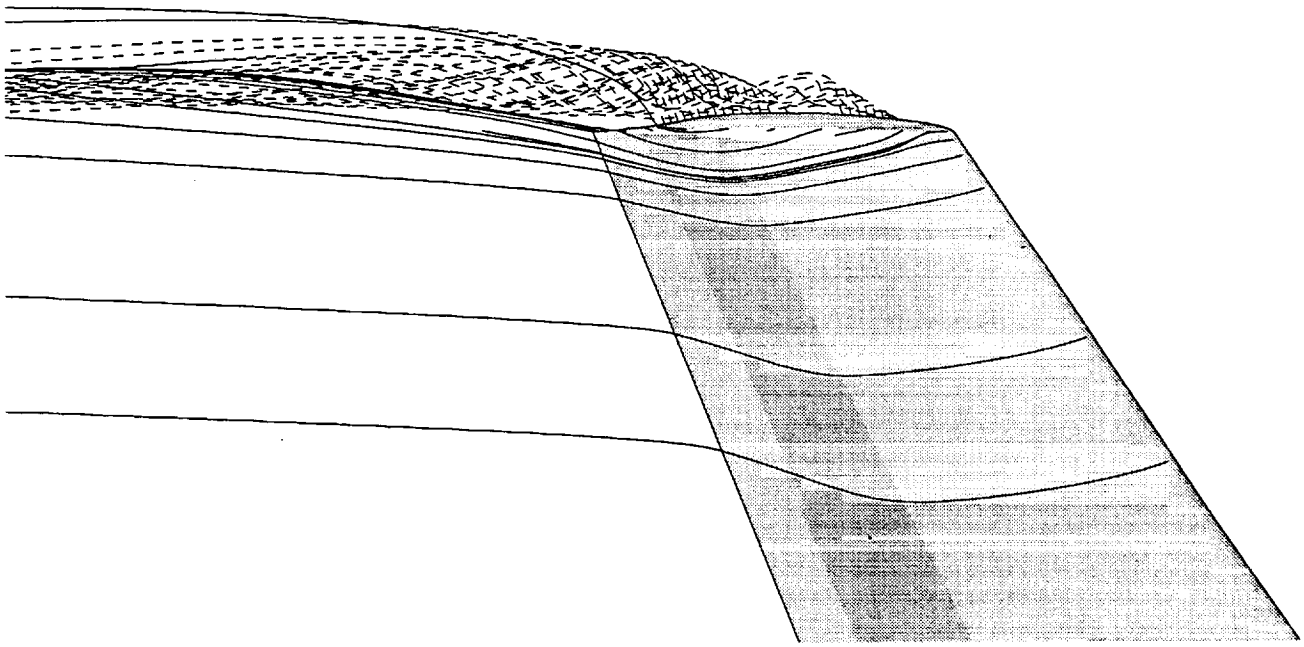

Figure 34. Computed particle paths on upper surface near wingtip with exhaust of both jets deflected downward 30° at $M_\infty = 0.72$ and $\alpha = 1°$. Paths starting at jet exit are denoted by dashed lines.

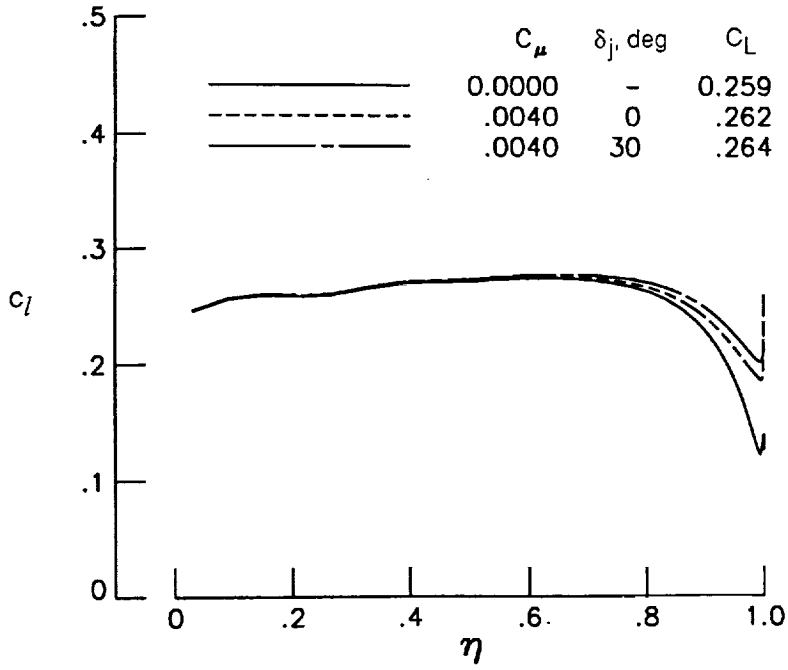

Figure 35. Computed spanwise variation of section lift coefficient with blowing at two deflection angles compared with no-blowing case at $M_\infty = 0.72$ and $\alpha = 1°$.

REPORT DOCUMENTATION PAGE

Form Approved
OMB No. 0704-0188

1. AGENCY USE ONLY *(Leave blank)*	2. REPORT DATE	3. REPORT TYPE AND DATES COVERED
	June 1995	Technical Paper

4. TITLE AND SUBTITLE
Study of Potential Aerodynamic Benefits From Spanwise Blowing at Wingtip

5. FUNDING NUMBERS
WU 505-59-10-30

6. AUTHOR(S)
Raymond E. Mineck

7. PERFORMING ORGANIZATION NAME(S) AND ADDRESS(ES)
NASA Langley Research Center
Hampton, VA 23681-0001

8. PERFORMING ORGANIZATION REPORT NUMBER
L-17368

9. SPONSORING/MONITORING AGENCY NAME(S) AND ADDRESS(ES)
National Aeronautics and Space Administration
Washington, DC 20546-0001

10. SPONSORING/MONITORING AGENCY REPORT NUMBER
NASA TP-3515

11. SUPPLEMENTARY NOTES
This report is an expanded version of a thesis submitted in partial fulfillment of the requirements for the Degree of Doctor of Science, George Washington University, Washington, D.C., May 1992.

12a. DISTRIBUTION/AVAILABILITY STATEMENT
Unclassified–Unlimited
Subject Category 02
Availability: NASA CASI (301) 621-0390

12b. DISTRIBUTION CODE

13. ABSTRACT *(Maximum 200 words)*
Comprehensive experimental and analytical studies have been conducted to assess the potential aerodynamic benefits from spanwise blowing at the tip of a moderate-aspect-ratio swept wing. Previous studies on low-aspect-ratio wings indicated that blowing from the wingtip can diffuse the tip vortex and displace it outward. The diffused and displaced vortex will induce a smaller downwash at the wing, and consequently the wing will have increased lift and decreased induced drag at a given angle of attack. Results from the present investigation indicated that blowing from jets with a short chord had little effect on lift or drag, but blowing from jets with a longer chord increased lift near the tip and reduced drag at low Mach numbers. A Navier-Stokes solver with modified boundary conditions at the tip was used to extrapolate the results to a Mach number of 0.72. Calculations indicated that lift and drag increase with increasing jet momentum coefficient. Because the momentum of the jet is typically greater than the reduction in the wing drag and the increase in the wing lift due to spanwise blowing is small, spanwise blowing at the wingtip does not appear to be a practical means of improving the aerodynamic efficiency of moderate-aspect-ratio swept wings at high subsonic Mach numbers.

14. SUBJECT TERMS
Spanwise blowing; Wingtip blowing

15. NUMBER OF PAGES
100

16. PRICE CODE
A05

17. SECURITY CLASSIFICATION OF REPORT	18. SECURITY CLASSIFICATION OF THIS PAGE	19. SECURITY CLASSIFICATION OF ABSTRACT	20. LIMITATION OF ABSTRACT
Unclassified	Unclassified	Unclassified	